A MULTI-AXIS COMPACT POSITIONER WITH A 6-COIL PLATEN MOVING OVER A SUPERIMPOSED HALBACH MAGNET MATRIX

A Thesis

by

VU HUY NGUYEN

Submitted to the Office of Graduate Studies of
Texas A&M University
in partial fulfillment of the requirements for the degree of

MASTER OF SCIENCE

May 2011

Major Subject: Mechanical Engineering

A Multi-axis Compact Positioner with a 6-coil Platen Moving Over a Superimposed

Halbach Magnet Matrix

A MULTI-AXIS COMPACT POSITIONER WITH A 6-COIL PLATEN MOVING OVER A SUPERIMPOSED HALBACH MAGNET MATRIX

A Thesis

by

VU HUY NGUYEN

Submitted to the Office of Graduate Studies of
Texas A&M University
in partial fulfillment of the requirements for the degree of

MASTER OF SCIENCE

Approved by:

Chair of Committee,	Won-jong Kim
Committee Members,	Alexander Parlos
	Hamid Toliyat
Head of Department,	Dennis O'Neal

May 2011

Major Subject: Mechanical Engineering

ABSTRACT

A Multi-axis Compact Positioner with a 6-coil Platen Moving Over a Superimposed Halbach Magnet Matrix. (May 2011)

Vu Huy Nguyen, B.S., Hanoi University of Science and Technology

Chair of Advisory Committee: Dr. Won-jong Kim

A multi-axis compact positioner is designed and implemented in this thesis. The single-moving-part positioner is designed to move in the magnetic field generated by a superimposed concentrated-field permanent magnet matrix. The compact positioner is primarily for the stepping and scanning applications that require 3-DOF planar motions. In which, the travel ranges in two orthogonal directions are on the order of 100 mm. The moving platen, which has the size of 185.4 mm × 157.9 mm and weighs 0.64 kg, mainly comprises of a plastic frame and six copper coils. It is actuated in the horizontal plane by flowing six independent electric currents into the coils. The platen is supported against gravity by three air bearings.

Force calculation is based on the Lorentz force law. With a current-carrying rectangular coil placed in the magnetic field of the supper-imposed Hallbach magnet matrix, the force acting on the coil is calculated by volume integration. The distances between the longer sides and between the shorter sides of the rectangular coil are designed to fit a half pitch and one pitch of the Hallbach magnet array, respectively.

Therefore, the volume integration is simplified considerably. The force-current relation for the entire platen with six coils is derived.

Three Hall-effect sensors are attached to the moving platen to measure the magnetic flux densities at the center points of the sensors. The position of the moving platen is determined by the field solution of the magnet matrix and the magnetic flux densities sensed by the Hall-effect sensors. A new discrete PID-like controller is proposed and tested. For the step responses with the step sizes within 1000 μm, the overshoots and the steady state errors are negligible. The achieved velocity in x is 10.50 cm/s and in y is 16.25 cm/s, respectively. The achieved acceleration in x is 43.75 cm/s^2 and in y is 95.59 cm/s^2, respectively. The achieved travel ranges are 15.24 cm in x, 20.32 cm in y, and 0.21 rad in the rotational motions about the vertical axis. The positioning resolution in x and y is 8 μm with the rms positioning error of 6 μm. The positioning resolution in rotation about the vertical axis is 130 μrad.

ACKNOWLEDGMENTS

First of all, I cannot thank Dr. Won-jong Kim, my thesis advisor, enough for his guidance on my academic work at Texas A&M University. I would like to express my deep gratitude to him for his broad knowledge, very high intensity of working, and his enthusiasm for advising his students.

I wish to thank Dr. Alexander Parlos and Dr. Hamit Toliyat for serving on my thesis committee. I would like to thank Tiejun Hu and Ho Yu, former Ph.D. students of Dr. Kim, who developed the first and second maglev positioners in our lab. I learned much of knowledge and experience from their works.

I also wish to thank Mr. Robert W. Wenck, Mrs. Linda Caraway, and Mr. Tim Thornton, for their friendship and for teaching me English since the early time I came to Texas A&M University.

I would like to express my thank to Mr. Van Le, Mr. Nghi Nguyen, Mr. Son Nguyen, and Dr. Ninh Le, who are currently at the Faculty of Mechanical Engineering, University of Transport and Communications, Hanoi, Vietnam. They helped me much when I first launched my academic career. While working with them, I had matured significantly in my specialty area of mechanical engineering. Thanks to Mr. Van Anh for spending his great time and efforts to help me in cutting the frame of the moving platen by a computer-numerical-control milling machine.

Without unconditional love, care and continuing supports from my parents, my wife, and my sisters, I would not be able to go forward; I can never thank them enough for everything they have done for me.

TABLE OF CONTENTS

CHAPTER Page

LIST OF FIGURES

FIGURE Page

FIGURE Page

FIGURE Page

FIGURE Page

LIST OF TABLES

CHAPTER I

INTRODUCTION

1.1 Design objectives

This thesis project is to design and control of a three-degree-of-freedom (3-DOF) compact positioner, which is levitated by three air bearings, working over a superimposed Halbach magnet array [1, 2]. The high-precision compact positioner designed in this project is primarily for stepping and scanning applications that require multi-axis motions in which the travel ranges in two orthogonal dimensions are on the order of 100 mm. Following are some specifications of the positioner:

- Total number of coils in the moving platen: 6
- Mass of the moving platen: less than 0.8 kg
- Travel ranges: at least 150 mm × 150 mm in x and y directions
- Positioning resolution in x and in y: 10 micrometer
- Maximum velocity in x and y: at least 10 cm/s.

1.2 Applications of high-precision multi-axis positioners

Precise multi-axis positioners have been increasingly used in a large number of applications in the industry. Among them, a very popular application in semiconductor

---

This thesis follows the style and format of *IEEE Transactions on Automatic Control.*

manufacturing is wafer steppers in photolithography. In a scanning probe microscope or a scanning electron microscope, there must be a high-precision positioning system. In the micro-electronic assembly, precise multi-axis positioners are required for component placement, component mounting, and inspection of printed-circuit boards. Other common applications are surface profilometer to scan and measure surface profiles and active multi-axis vibration rejection.

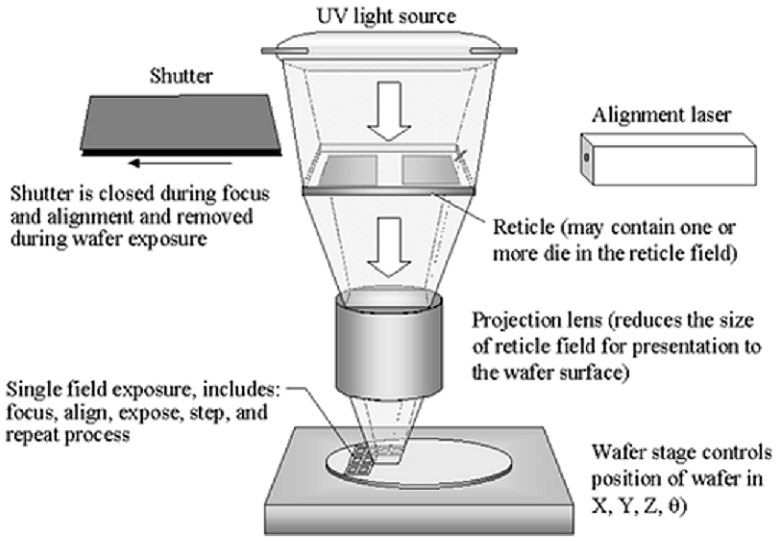

Figure 1-1: Projection lithography equipment [3].

Multi-axis positioners are commonly used in semiconductor manufacturing processes. Figure 1-1 shows the structure and components of a projection lithography system. In which are an ultraviolet light source, a reticle with a die pattern, a laser-alignment system, a wafer covered with a light-sensitive photoresist, and a projection

lens. The lens is to focus the ultraviolet light passing through the reticle onto the surface of the wafer, and to reduce the reticle image. The wafer is carried by a multi-axis positioner. A reticle image on the wafer is reproduced through exposure of the resist.

In the early 1990s, SVG Lithography introduced a hybrid step-and-scan approach [4]. In this approach, a rectangular field, being noted as a single-exposure field in Figure 1-2, is scanned in one direction to expose the entire reduction mask. The wafer is then stepped to a new die site and the scanning process is repeated.

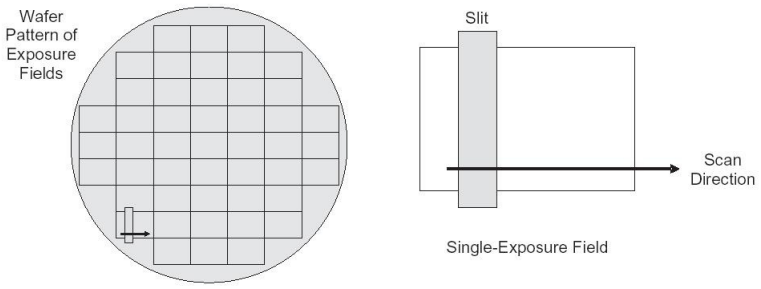

Figure 1-2: Step-and-scan imaging [4].

It is essential that a projection optical exposure tool includes a highly accurate and precise stage to position the wafer exactly to the correct die site to receive the projected image [5]. In optical projection lithography with step-and-scan approach, there must be a stage to align the wafer to the reticle and the lens, and another stage to precisely move the reticle in a relative motion to the wafer. Along with these, the stage that carries the wafer is required to move in a X-Y plane to step the wafer to different locations for the fields to be scanned. Furthermore, the alignment system must exactly

align a wafer to the position of the previous one. The functions of the wafer-carrying stage described above require precise translational motions along x and y directions and precise rotation about the z-axis.

Smaller imaging field and higher productivity of wafer steppers require that the motion resolution of the stage gets smaller, the travel range is larger, and the mechanical dynamics of the stages is improved. For step-and-scan photolithography, one has to deal with the difficulty in synchronizing the motions of the reticle stage and the wafer stage. In order to yield high throughput, high speed and acceleration of the stages must be obtained. However, when stepping the stages to new positions, there must be a certain time for the moving stages to stop and settle down, reducing vibrations. It is sometimes possible to make a trade-off in the wafer fabrication between throughput and stage precision, depending on the needs of the wafer product [5]. With the increasing demands on higher productivity in the applications mentioned above, multi-axes positioners need to be more precise, faster, and more reliable.

1.3 Prior art of the single-platen electromagnetic multi-axis positioners

1.3.1 The world's first 6-DOF precise planar magnetic-levitation stage

The world's first one-moving-part 6-DOF precise planar magnetic-levitation stage was developed by Won-jong Kim at Massachusetts Institute of Technology in 1997 [1]. Figure 1-3 below describes the structure of the positioning system. In this design, the winding is stationary and the permanent magnet arrays are attached to the moving platen. There are totally 4 motors; each has 3 phases with 11 windings per phase. Each

motor is to generate two force components, one in the z-direction and the other one in the x-direction or the y-direction.

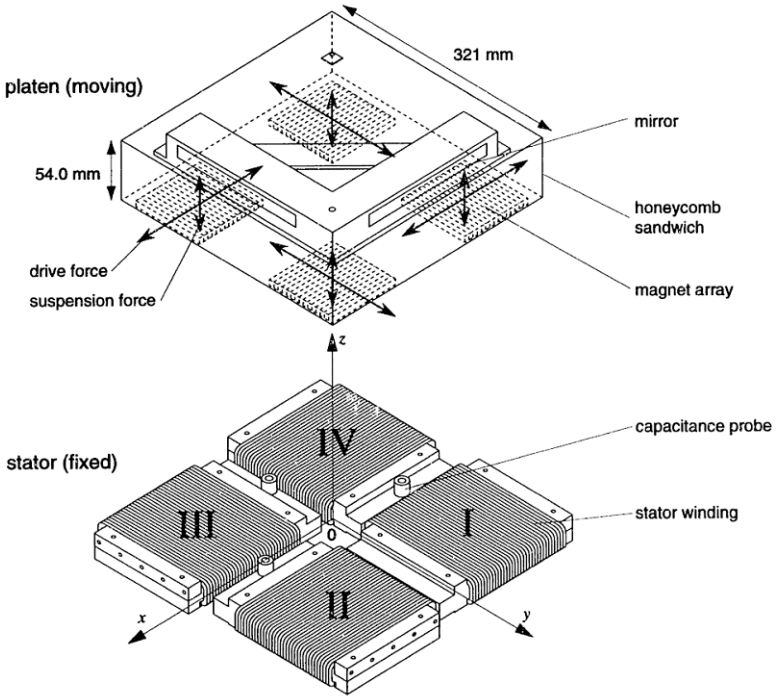

Figure 1-3: Structure of the design with four motors [1].

DQ decomposition was performed to obtain the electric current-force relation and to eliminate the nonlinearity due to trigonometric functions. Two orthogonal force components are decoupled to control the two degrees of freedom independently. As in Figure 1-4, the *D*-axis is defined as the z'-axis in the platen frame; the *Q*-axis leads the *D*-axis by $\frac{l}{4}$ [1]. Here, l is a spatial pitch of the Halbach magnet array.

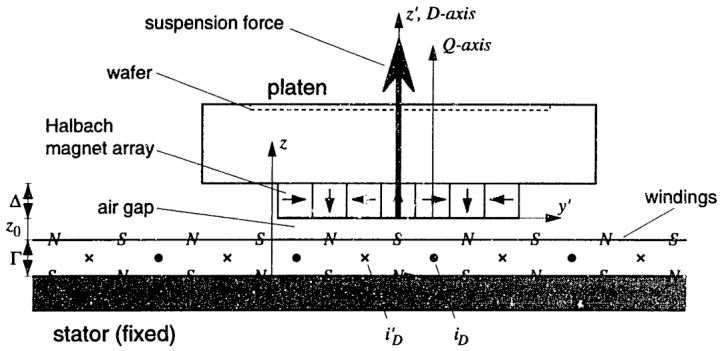

Figure 1-4: Suspension of the platen in dynamic equilibrium [1].

Apart from the linearity in force-current relation and no mechanical contact during moving, this positioning system has a number of advantages:

- Being symmetric in the *x*-direction and the *y*-direction.
- There is no wire or cable connected with the moving platen, except a thin ground wire for the capacitance gauges.
- There is no heat stored and dissipated through the moving platen. Therefore, the thermal expansion error is minimized [1].

Some specifications of this magnetic-levitation positioning system are as following:

- Sampling rate: 5 kHz
- Control bandwidth: 100 Hz
- Maximum acceleration: 2 *g*
- Overall mass of the moving platen: 5.6 kg
- Travel range: 50 mm in *x*, 50 mm in *y*, 400 μm in *z* direction [1].

1.3.2 Advanced Technology Program (ATP) stage

The ATP stage was developed by Hu, a former Ph.D. student of Dr. Won-jong Kim [6]. The moving platen works over a superimposed Halbach magnet matrix, which is the superimposition of two orthogonal single-axis Halbach magnet arrays. Figure 1-5 shows the moving platen with its components. The design uses the same linear force-current relation as in [1] by *DQ* decomposition. There are 3 motors with 3 phases per motor and 4 windings per phase. Each motor can generate a force in the *z*-direction and the other one in the *x*-direction or the *y*-direction. Totally 6 force components distributed as in Figure 1-6 are sufficient for the moving platen to move in 6 DOFs.

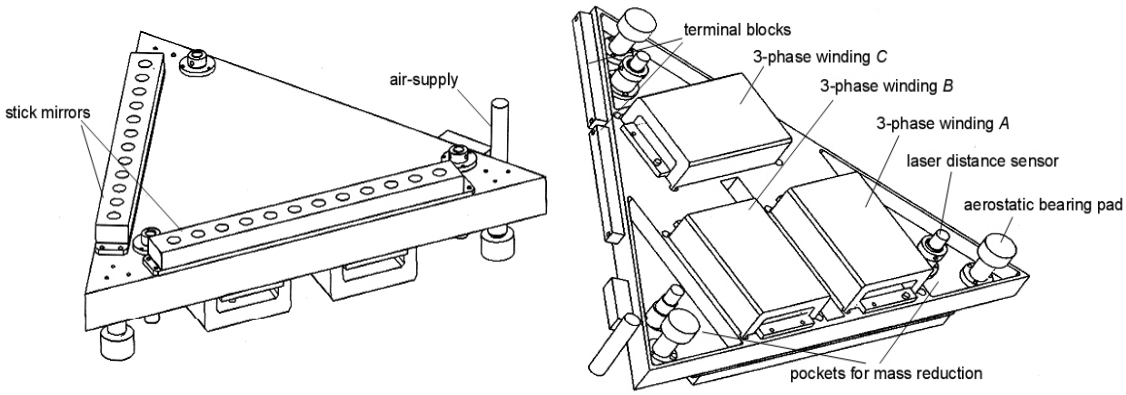

Figure 1-5: Top and bottom of the moving platen [6].

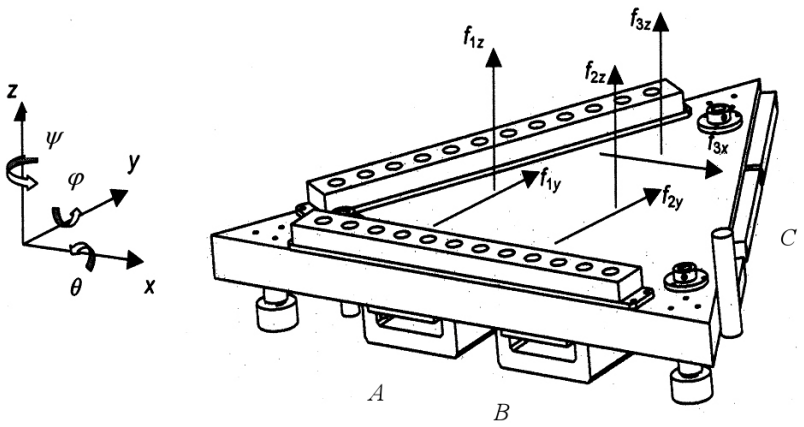

Figure 1-6: Forces generated by three sets of coils of the moving platen [6].

Three Agilent laser interferometers are used to sense the exact position of the moving platen in planar motions. There are two stick mirrors reflecting the laser beams. Three Nanogage 100 laser distance sensors are to measure the distances from the laser heads to the flat aluminum surface on top of the magnet matrix. With these measurements, the roll, pitch, and yaw angles of the moving platen can be determined.

The moving platen, which weights 5.91 kg, can travel a range of 160 mm in *x*, 160 mm in *y*. The positioner demonstrated a position resolution of 20 nm and position noise of 10 nm rms in *x* and *y* and 15 nm rms in *z*. Maximum velocity achieved is 0.5 m/s at a 5 m/s^2 acceleration [6].

1.3.3 Long-stroke magnetically levitated linear actuator

A moving-coil-structure electro-dynamic planar motor was developed by Compter [7]. The stationary part is a two-dimentional Halbach magnet array. The moving part has four forcers with three phases per forcer. Figure 1-7 shows the structure

of the planar motor with the stationary magnet plate and four forcers fixed to the moving part.

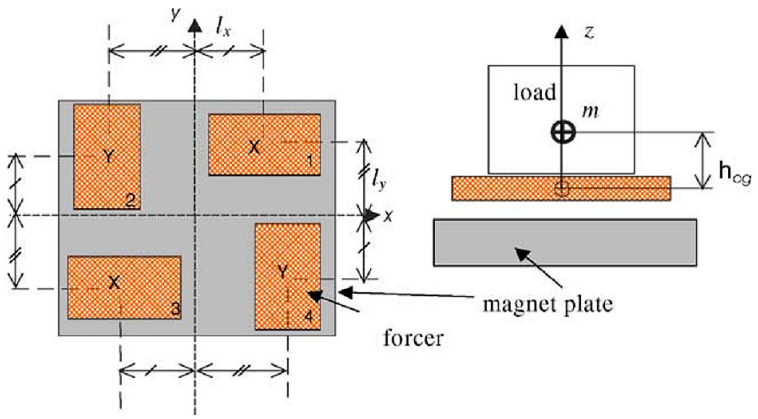

Figure 1-7: The electro-dynamic planar motor with four forcers in the moving part [7].

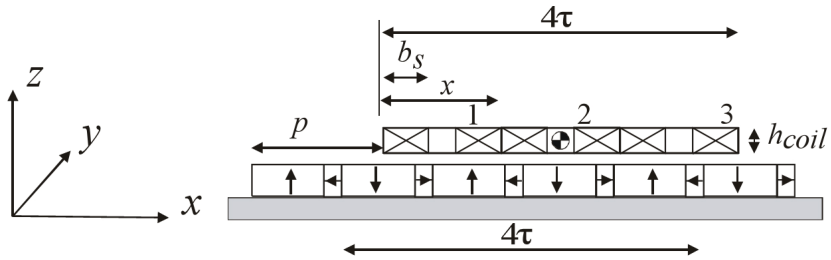

Figure 1-8: Cross section of a forcer with the Halbach magnet array [7].

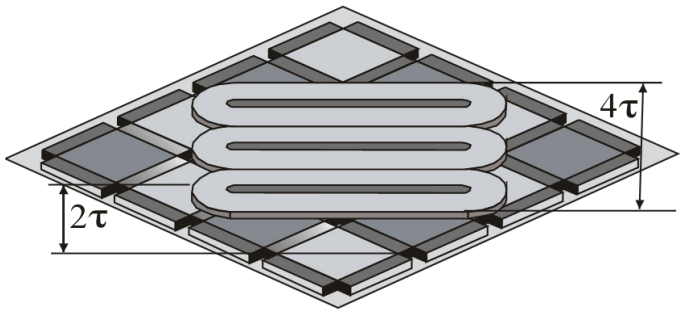

Figure 1-9: Magnet orientation [7].

Figure 1-8 shows a cross-sectional view of a forcer with the Halbach magnet array. The horizontal distance between two adjacent coils is $4\tau/3$ where τ is one spatial pitch of the magnet array. Each forcer is a symmetrical three-phase motor. In Figure 1-9, the magnet orientation is illustrated. The angle between the longer sides of the coils and the edges of the magnet blocks is 45°. Each forcer can generate two force components in the vertical direction and in a horizontal direction. The force-current relation for a forcer was derived with the introduction of the current amplitude and the current phase. In which, the current amplitude determines the force amplitude and the force angle is controlled by the current phase angle [7]. The positioning resolution, the maximum velocity, acceleration and travel ranges of this electro-dynamic planar motor are not shown in [7]. In this system, the sensing accuracy of 1% of a spatial pitch of the magnet array is low if the spatial pitch is on the order of 10 mm.

The long-stroke magnetically levitated linear actuator was developed by a group of researcher at Department of Electrical Engineering, Eindhoven University of Technology [8]. This design is for 3-DOF planar motions. In which, the magnet is moving and the coils are stationary.

The translator is a Halbach magnet array. The angles between the sides of the magnet blocks and the sides of the coils are 45°, as shown in Figure 1-10. There are 10 coils in the stators. Five adjacent coils are simultaneously energized to control the 3 DOFs [8]. A nonlinear model-based commutation algorithm for this actuator was developed in [9]. A commutation and switching algorithm was introduced in [8]. The advantages of this long-stroke linear actuator are its simple structure, the capability to

extend or shorten the motion range easily in the *x*-direction by changing the number of coils aligned in the stator, and no wire connected to the moving part.

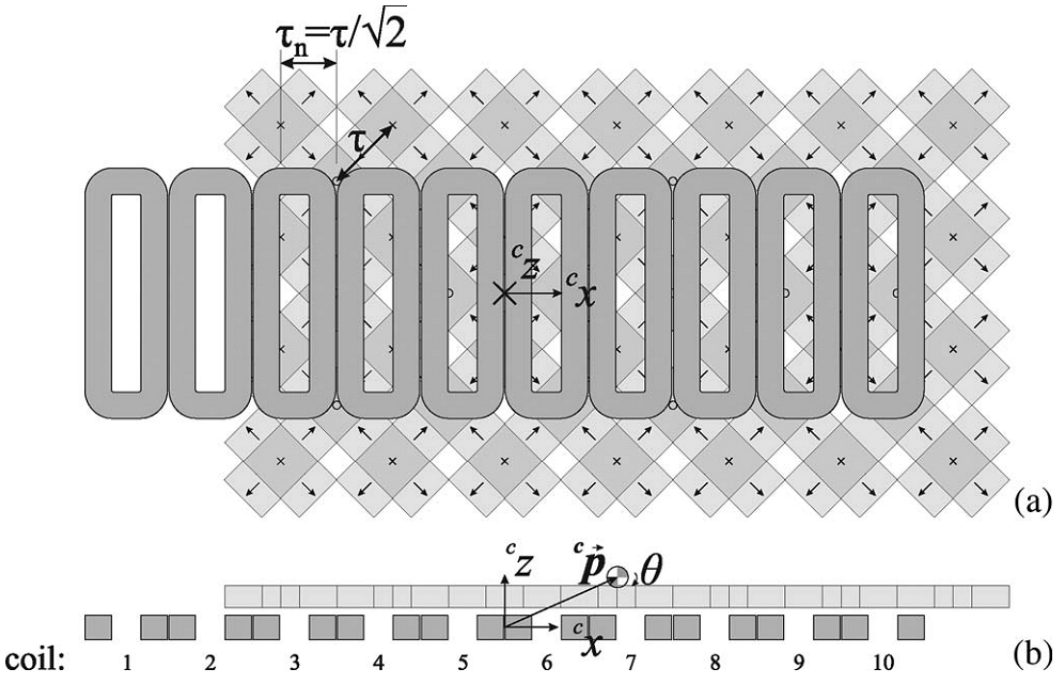

Figure 1-10: (a) Bottom view and (b) Side view of the linear actuator [8].

There is a point in this design that is unsuitable for the target applications described in Subsection 1.1. The forces acting on the moving platen are distributed within the closed area corresponding to the adjacent coils which are energized. When the platen moves, the acting points of those forces are not fixed to the platen but moving. This negatively affects the mechanical dynamics of the moving platen, especially in causing the error torque about the *y*-axis.

1.3.4 Compact 6-degree-of-freedom precision positioner

The compact 6-degree-of-freedom precision positioner was developed by Yu, a former Ph.D. student of Dr. Won-jong Kim [10]. The moving platen in this positioning system also works over a superimposed Halbach magnet matrix. There are 3 motors as in [6] and the force allocations of the two designs are the same. In Figure 1-11, the motors are noted as 3-phase windings A, B, and C. In this design, the number of coils per motor is only 3, compared to 12 in [6]. Therefore, the total number of coils, the mass and volume of the moving platen, and the energy consumed are reduced considerably. There are 3 Hall-effect sensors attached to the moving platen to measure the magnetic flux densities at the center points of the sensors. The position of the moving platen is determined by the field solution of the magnet matrix and the magnetic flux densities sensed by the Hall-effect sensors. Figure 1-12 illustrates the collaboration of two Hall-effect sensors to locate the position of the moving platen in a horizontal direction. Beyond the sensitive intervals as noted in Figure 1-12, the sensing noise is relatively large and the magnetic flux density may exceed the sensing range of the sensors. Therefore, a sensor is only used for locating the position of the moving platen if it is in a sensitive interval.

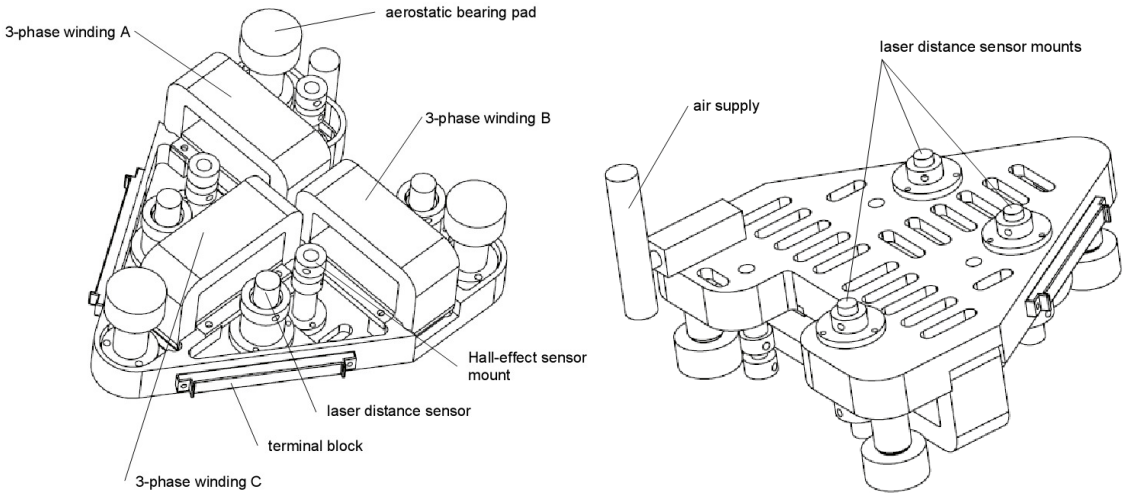

Figure 1-11: Structure and components of the moving platen [10].

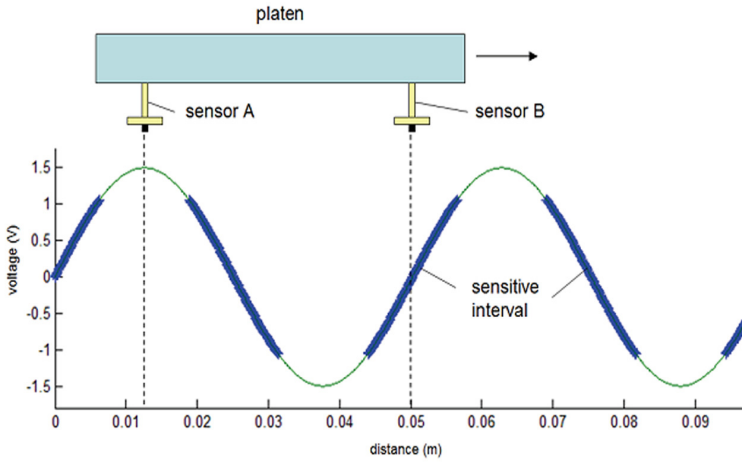

Figure 1-12: Collaboration of two sensors [10].

The total mass of the moving platen is 1.52 kg. The travel ranges are 220 mm in the *x*-direction and 200 mm in the *y*-direction. Translational motion resolution is 10 μm. The rotation angle of 12° was achieved in rotation around the *z*-axis [10], which is perpendicular to the top flat surface of the magnet matrix.

1.3.5 A planar actuator with a small mover travelling over large yaw and translational displacements

A planar actuator with a small mover travelling over large yaw and translational displacements was developed by Ueda and Ohsaki [11]. Figure 1-13 shows the structure of the planar actuator. This is a moving-magnet design; the moving part is a 2-D Halbach permanent magnet array. The stator has two sets of three-phase armature conductors arranged on a double-layered printed circuit board. The Halbach permanent magnet array is positioned 45° from the armature conductors [11].

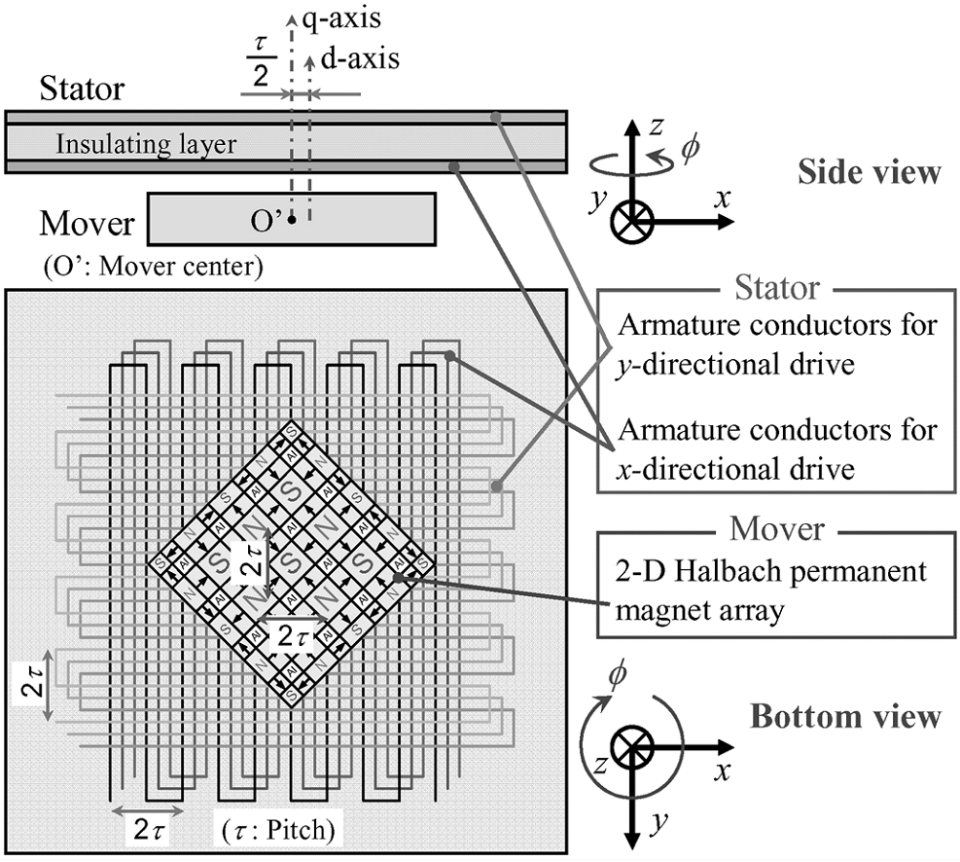

Figure 1-13: Fundamental structure of the planar actuator [11].

DQ decomposition was applied for decoupling control of the thrusts in the *x*- and *y*-directions and the torque about the vertical axis. The travel range in *x* and in *y* is 20 mm and in rotation about the *z*-axis is 10°. The maximum velocity, maximum acceleration and the positioning resolution are not given in [11]. Having the armature conductors integrated in a doubled-layer printed board circuit is the point that makes this design different from the prior art. This reduces the size of the positioner, especially in the vertical direction. However, the drawback is the force acting on the moving part in each horizontal direction generated by currents flowing in a single layer of conductors must be relatively small compared to the force generated by currents flowing in a multi-layer coil. Another disadvantage is that the positioning errors are large. In some step responses with the step sizes of 20 mm in *x* and 10° in ϕ as discussed in [11], the position errors in *x* are larger than 0.2 mm and the position errors in ϕ are larger than 0.3°. The mover is supported in the vertical direction by mechanical bearings with considerable friction. This negatively affects the dynamics of the mover, causing steady state errors.

1.4 Design considerations

1.4.1 Why single moving part?

In multi-moving-part positioning systems, there are usually errors in the mechanical joints between the mechanisms of the positioners. These errors are accumulated from the base to the end-effector of a multi-part positioner, directly increasing its response time and reducing the mechanical rigidity. In comparison with the

multi-part positioners, the single-moving-part positioners are much simpler to be modeled for dynamic analysis. If there are two or more parts in a positioner, one cannot focus on the dynamics of the end-effector only but the dynamics of the entire complex mechanical system with friction and hysteresis.

In applications that require multi-DOF motions, which include large motion ranges in two orthogonal dimensions, it is common that multi-part positioners accompany bulky mechanisms. In contrast, a single-part magnetically levitated positioner with a magnet matrix can solve the problem. Here, the stationary part, being either the magnet or the winding, has the size corresponding to the desired motion ranges. The moving part, which can perform multi-axis motions, can be designed to be in a very compact size.

1.4.2 Moving magnet or moving coil?

This subsection compares two structures in multi-axis positioning stages working with magnet matrices: moving-magnet structure and moving-coil structure. The focus is only positioning systems that are primarily for stepping and scanning applications with large travel ranges in two directions.

There is no wire connected to the moving stage in a moving-magnet structure. The coils are fixed in the stationary part and the permanent magnet array or matrix is moving. Therefore, force disturbances due to wire stiffness, which present in moving-coil structures, are avoided.

The heat from the coils in a moving-magnet maglev system can be dissipated

easily through its stationary part. In contrast, the heat in a moving-coil maglev system heats up the coils themselves and the frame of the moving platen. If the coils get heated and their temperature increase, their resistances decrease. Taking this into account will make the control system more complicated and time consuming. When the frame of the moving platen is heated up, it may be deformed. This causes errors in positioning because there are mirrors or sensors attached to the moving platen.

In a moving-magnet design, in order to have motion ranges in two directions, it is required that the coils are relatively large or the number of coils is large. Larger coils result in more energy consumed. A large number of coils lead to complications in switching-coil algorithms. In a in moving-coil design, the coil is relatively small, and the stationary magnet matrix is large to give long travel ranges. Depending on the design structure, the number of coils can be small, and a switching-coil algorithm is unnecessary.

Eventually, in both moving-magnet and moving-coil designs, there must be trade-off between the advantages and the drawbacks. In this thesis project, moving-coil structure is chosen. This is to take the advantage of a superimposed Halbach magnet matrix with the size of 12 inch × 12 inch and to obtain long-range motions with a light, compact, and low-center-of-gravity moving platen.

1.4.3 Rectangular coils or circular coils?

In the magnetic field of a superimposed Halbach magnet matrix, along a straight line parallel to the x-axis, the magnetic flux densities in the x- and z-directions vary

sinusoidally, the magnetic flux density in the *y*-direction is a constant. A three-dimension (3-D) plot of the magnetic flux density on a plane parallel to the top surface of the magnet matrix looks like an egg cage, as seen in the figure shown on page 26. If a rectangular coil is placed so that its sides are parallel to the sides of the magnet matrix and a coil surface is parallel to the surface of the magnet matrix, ignoring the curved parts of the coil, the electromagnetic force can be calculated by simple volume integration for the right-rectangular-prism parts of the coil. This is simpler than doing the volume integration for a round coil with the coil surface parallel to the surface of the magnet matrix. For the purpose of a multi-dimensional positioner moving over a superimposed Halbach matrix with long travel ranges in *x* and *y*, and with small rotational motions about the *z*-axis, in this thesis project, the rectangular-coil shape is chosen.

1.5 Thesis overview

The thesis consists of 8 chapters: Introductions, Analysis, Electromechanical Design of the moving platen, Mechanical Design and Assembly, Instrumentation, Dynamics Analysis and Controller Design, Experimental Results, Conclusions and Future Works.

Chapter I, Introductions, describes applications of multi-axis positioners, prior art in research on multi-axis single-platen positioners, design considerations, thesis overview, and significance of thesis contributions.

Chapter II, Analysis, discusses the Halbach magnet matrix and electric current-

force relation for a single rectangular coil placed in the magnetic field of the Halbach magnet matrix. The single-axis Halbach array is introduced first, followed by the superimposed Halbach magnet matrix. In calculating the resultant force acting on a single rectangular coil, the forces acting on its sides due to different components of magnetic flux densities are calculated and summed.

Chapter III is Electromechanical Design of the moving platen. Based on the characteristics of the superimposed Halbach magnet matrix, the desired forces to move the platen, and the allowable size of the platen, the coil shape and size is designed first. The placement of the coils in the platen is then figured out in detail. Following that, the electric current-force relation for the 6-coil moving platen is derived.

Chapter IV is about the Mechanical Design and fabrication of the moving platen. The platen is cut to be only a single part with a single-tool process. Mechanical assembly of the platen, including the frame, the coils, and the air bearings, is also discussed.

Chapter V, Instrumentation, introduces the VME-bus computer to control the system, the Hall-effect sensors used to measure magnetic flux density, and the power amplifier circuits to provide the coils with electric currents.

Chapter VI presents Dynamics Analysis and Control of the Positioner. In this chapter, the electric current-force relation derived in Chapter III and the Newtonian force laws are used to analyze electromechanical dynamics of the moving platen. In order to close the control loop for the 3-DOF motions of the platen, a discrete PID-like control approach is proposed.

In Chapter VII, Experimental Results are shown in step responses in single-axis

motions and achieved travel ranges in translational motions in *x* and *y*. Along with this, the dynamic behaviors of the positioner are discussed and explained.

In Chapter VIII, the conclusions are drawn with advantages, disadvantages, and applicability of the design presented in this thesis project. In addition, future works are suggested.

1.6 Thesis contributions

A novel 3-DOF compact positioner levitated by three air bearings has been designed to work over a superimposed Halbach magnet matrix. A significant contribution is the capability of the positioner to generate 3-DOF motions by only a single moving part with total 6 coils. Based on the features of the superimposed Halbach magnet matrix, the coil size and the arrangement of the coils in the moving platen have been designed for a new electromechanical commutation. Figure 1-14 shows relative positions of the coils in this arrangement.

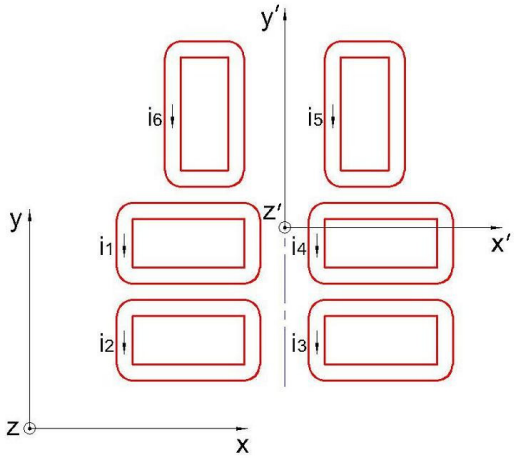

Figure 1-14: Relative positions of the coils in the moving platen.

The distance between two shorter sides of a rectangular coil fits one pitch of the magnet matrix. Therefore, when the moving platen is placed so that all the sides of the rectangular coils are parallel to the top surface of the magnet matrix, the volume integrations to calculate the forces are simplified considerably. This is because the horizontal electromagnetic forces acting on the shorter coil sides cancel out. The distance between two longer sides of a coil fits a half of one pitch of the magnet matrix. Therefore, the two horizontal electromagnetic forces, which act on the two longer coil sides, have the same direction and magnitude. Ignoring the effects of the curve parts at the corner of the rectangular coils, once the position of the moving platen is known, the force-current relations for the moving platen have been figured out to be in the form of $\boldsymbol{F} = \boldsymbol{A}\boldsymbol{i}$. Where $\boldsymbol{F}$ and $\boldsymbol{i}$ are the column vectors of forces and electric currents, respectively; $\boldsymbol{A}$ is a 3×6 matrix, of which each non-zero element depends in x or y sinusoidally, and in z exponentially.

The other significance of the thesis contributions is the compact size and light mass of the moving platen. The center of mass of the moving platen is as low as 10.2 mm from the mirror-finished aluminum surface on top of the magnet matrix, thereby, reducing the error torque about the x- and y-axes significantly. The height of the moving platen, from the aluminum surface on top of the magnet matrix to the top surface of the platen's frame is only 22.2 mm. Its total mass is only 0.64 kg. A picture of the fully-assembled moving platen is given in Figure 1-15.

Electromechanical dynamics of the positioner has been derived for 3-DOF planar motions. A discrete PID-like control approach is proposed and tested to close the control

loops of the system.

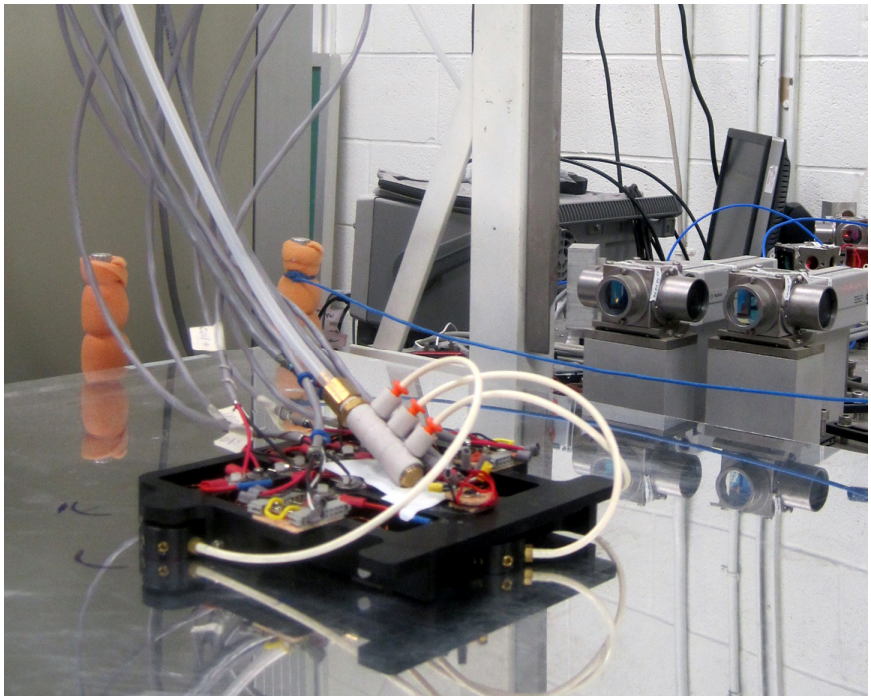

Figure 1-15: The fully-assembled moving platen on top of the magnet matrix.

CHAPTER II

ANALYSIS

2.1 Halbach magnet array

The Halbach magnet array was first introduced in [12]. The distinguished feature is the asymmetry of the magnetic field. The magnetic field is reinforced on one side of the magnet array and cancelled on the other side. In the conventional magnet arrays used for linear motors without iron backing, the winding is in one side of the magnet array. The magnetic field in the other side is wasted.

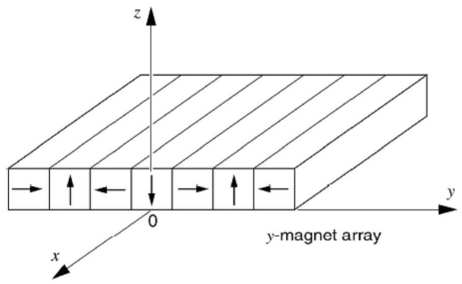

Figure 2-1: *y*-magnet array with its magnetization [1].

In a Halbach magnet array, each magnet segment is rotated relatively to the magnet segment close to it with a fixed angle. This can be 90° or 45°, for example. As shown in Figure 2-1, the magnet array is formed by successively adding a block of magnet and rotating it 90° relatively to the previous one with the key point that all the rotations are in the same direction. On spatial pitch of this magnet array contains four

magnet blocks. The magnetic field of this linear Halbach magnet array is stronger than that of a conventional iron-less magnet array with the same size by a factor of $\sqrt{2}$ [1].

2.2 Superimposed Halbach magnet array

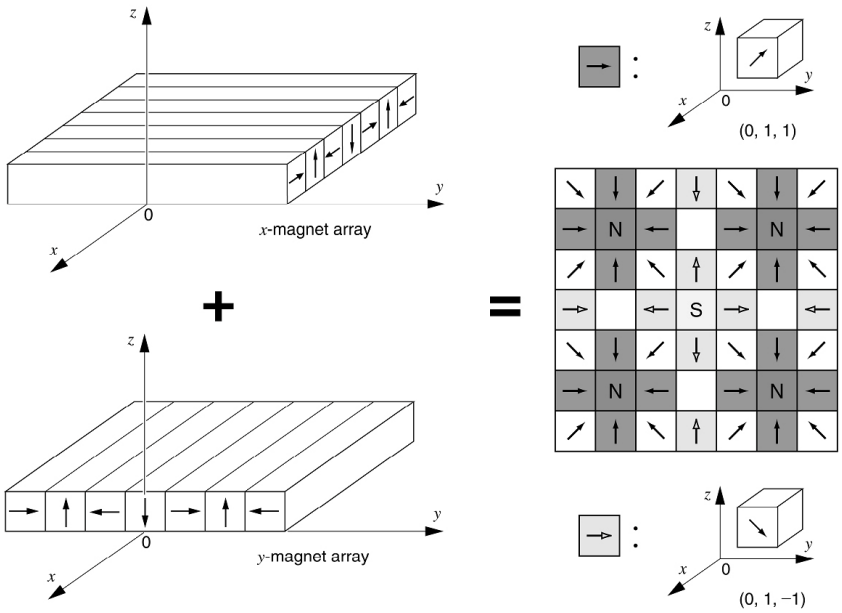

Figure 2-2: Illustration of superimposing two orthogonal single-axis Habach magnet arrays [1, 2, 5].

Two orthogonal single-axis Halbach magnet arrays are superimposed to produce a concentrated field magnet matrix [1, 2]. There are two types of magnet blocks. The ones which are noted as N (North) or S (South) are the strong magnet blocks. At the positions of the strong magnet blocks, two same-direction vectors of magnetic flux densities are added up. In Figure 2-2, the magnet blocks which are noted by an arrow are the weak ones. At the positions of the weak magnet blocks, two orthogonal vectors of

magnetic flux densities are superimposed. The remanence of each weak magnet block is $1/\sqrt{2}$ that of a strong magnet block. At the magnet blocks corresponding to blank squares/cubes, the magnetic flux density is cancelled.

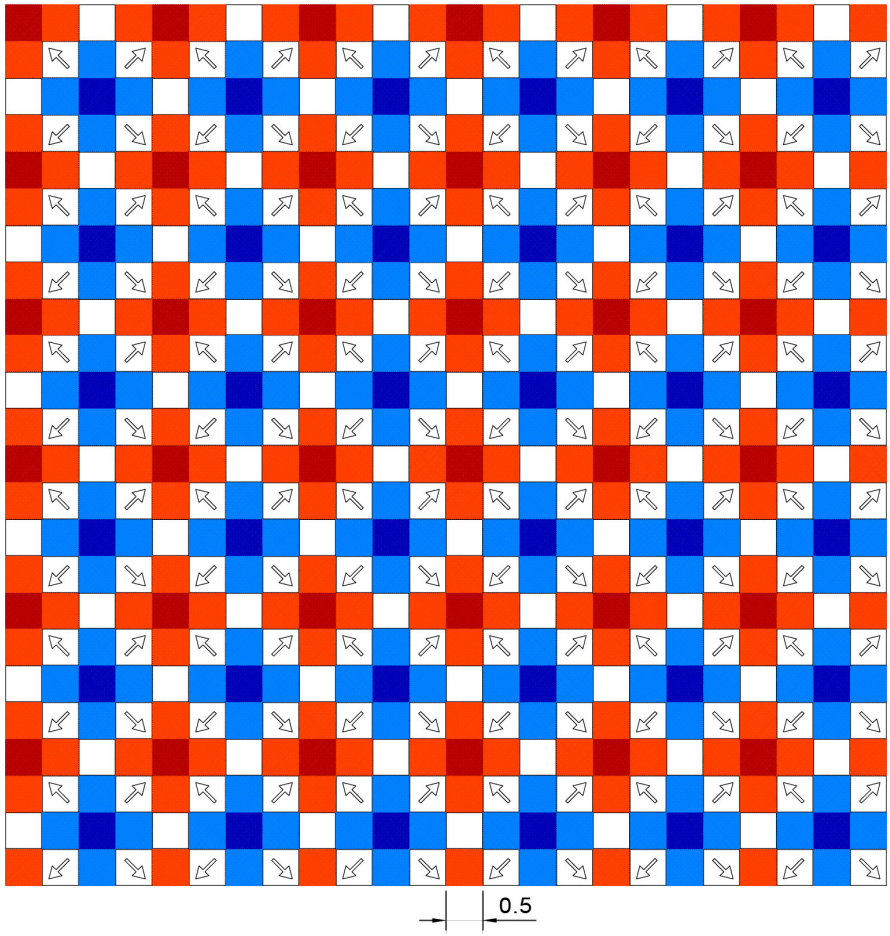

Figure 2-3: Illustration of a superimposed Halbach magnet matrix (length unit: inch).

The superimposed Halbach magnet matrix used in this thesis project was constructed by Nikhil Bhat, a former Master student of Dr. Won-jong Kim [13]. Figure 2-3 illustrates the arrangement of different types of magnet blocks in a superimposed

Halbach magnet matrix, whose size is approximately 12 inch × 12 inch. Magnet blocks with dark red and dark blue colors are strong magnets which have a remanence of 1.43 T. Blocks with light red and light blue colors, and blocks with an arrow are weak magnets which have a remanence of 1.10 T. The blank blocks are aluminum spacers. Each magnet block is a cube with the size of 12.7 mm × 12.7 mm × 12.7 mm. One spatial pitch of the magnet matrix along the x-axis or the y-axis is L = 50.8 mm.

For this superimposed Halbach magnet matrix, linear superposition applies. At any point in the magnetic field of the magnet matrix, the resultant magnetic flux density is the sum of magnetic flux densities generated by the two single-side Halbach magnet arrays. Figure 2-4 below shows the magnetic flux density on a plane parallel to the surface of the magnet matrix, the plane of z = 0.003 m. This is the resultant magnetic flux density in the z-direction due to linear superposition of two single-side Halbach magnet arrays.

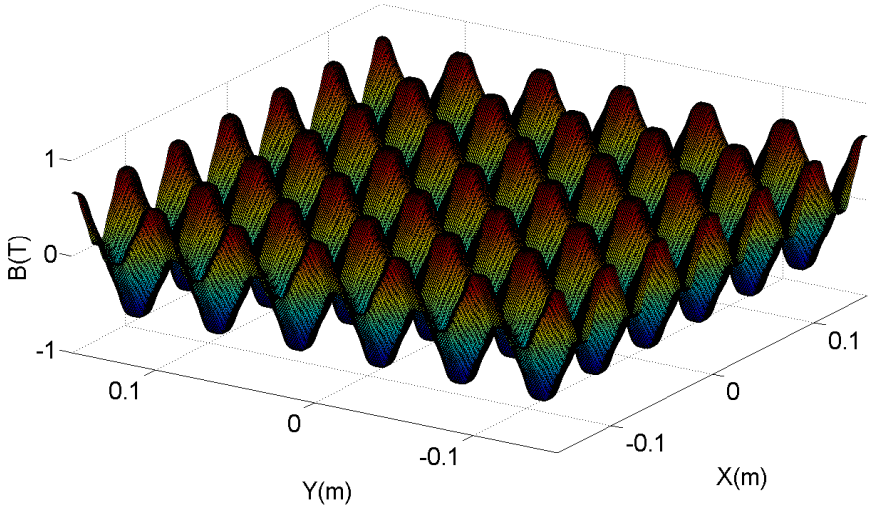

Figure 2-4: The resultant z-direction magnetic flux density component.

2.3 Field solution

We consider a single-axis Halbach magnet array as in Figure 2-5, namely array *A*, or the *y*-direction array, that has magnetic flux density components in the *z*-direction and the *y*-direction. O*xyz* is a Cartesian inertial coordinate system which is fixed to the magnet array; O*xy* is the surface of the magnet array in the strong side.

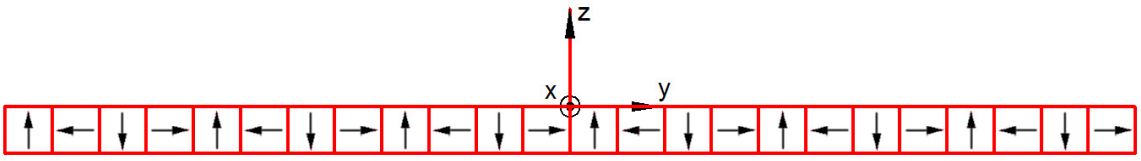

Figure 2-5: A single *y*-axis Halbach magnet array.

Along the *y*-axis, the magnetic flux density varies sinusoidally with a spatial pitch of *L*. Following [1], Fourier series representation is deployed for the field solution; the magnetic flux density *B* is represented as:

$$\boldsymbol{B} = \sum_{n=-\infty}^{+\infty} (B_{z,n}\boldsymbol{i}_z + B_{y,n}\boldsymbol{i}_y) = \sum_{n=-\infty}^{+\infty} (\tilde{B}_{zn}e^{-jk_n z}\boldsymbol{i}_z + \tilde{B}_{yn}e^{-jk_n z}\boldsymbol{i}_y)\,. \tag{2.3.1}$$

The *z*-component and the *y*-component magnetic flux densities are, respectively

$$B_z(x,y,z) = \sum_{n=-\infty}^{+\infty} B_{z,n}(x,y,z) = \sum_{n=-\infty}^{+\infty} \tilde{B}_{zn}(x,y,z)e^{-jk_n y}\,, \tag{2.3.2}$$

$$B_y(x,y,z) = \sum_{n=-\infty}^{+\infty} B_{y,n}(x,y,z) = \sum_{n=-\infty}^{+\infty} \tilde{B}_{yn}(x,y,z)e^{-jk_n y}\,, \tag{2.3.3}$$

where

$$\tilde{B}_{zn}(x,y,z)=\mu_0(-\frac{jk_n}{2\gamma_n}\tilde{M}_{yn}+\frac{1}{2}\tilde{M}_{zn})(1-e^{-\gamma_n\Delta})e^{-\gamma_n z}, \tag{2.3.4}$$

$$\tilde{B}_{yn}(x,y,z)=\mu_0(-\frac{1}{2}\tilde{M}_{yn}-\frac{j\gamma_n}{2k_n}\tilde{M}_{zn})(1-e^{-\gamma_n\Delta})e^{-\gamma_n z}, \tag{2.3.5}$$

$$\begin{cases}\tilde{M}_{zn}=\dfrac{\sqrt{2}M_0}{\pi|n|} \text{ for } \begin{cases}n=\pm(8r+1)\\ n=\pm(8r+3)\end{cases} & (2.3.6)\\ \tilde{M}_{zn}=-\dfrac{\sqrt{2}M_0}{\pi|n|} \text{ for } \begin{cases}n=\pm(8r+5)\\ n=\pm(8r+7)\end{cases} & (2.3.7)\end{cases}$$

$$\tilde{M}_{yn}=j^n\tilde{M}_{zn}. \tag{2.3.8}$$

In the equations above, $\boldsymbol{i_y}$ and $\boldsymbol{i_z}$ are the unit vectors of the *y*-axis and the *z*-axis, respectively. $\gamma_n = |k_n|$, where $k_n=2\pi n/L$, is the spatial wave number of the *n*th harmonic. $L =$ 0.0508 m is one spatial period of the Halbach magnet array. $\Delta =$ 0.0127 m is the dimension of a cubic magnet block. *r* is a non-negative integer. M_0 is the peak magnetization. μ_0 is the magnetic constant. $\tilde{M}_{yn}$ and $\tilde{M}_{zn}$ are the *y*-direction and *z*-direction magnetization components, respectively.

2.3.1 Field solution for the *z*-component magnetic flux density

Considering (2.3.4), denoting *k* as a non-negative integer, for $n = 4k + 1$, we have

$$\tilde{B}_{zn}(x,y,z)=\mu_0[-\frac{j}{2}\tilde{M}_{yn}\text{sign}(n)+\frac{1}{2}\tilde{M}_{zn}](1-e^{-\gamma_n\Delta})e^{-\gamma_n z} \tag{2.3.9}$$

$$-\frac{j}{2}\tilde{M}_{yn}\text{sign}(n)+\frac{1}{2}\tilde{M}_{zn}=\frac{1}{2}[-j^{(4k+1)}\tilde{M}_{zn}j+\tilde{M}_{zn}]=\tilde{M}_{zn}. \tag{2.3.10}$$

For $n = -(4k + 1)$, we have

$$-\frac{j}{2}\tilde{M}_{yn}\mathrm{sign}(n)+\frac{1}{2}\tilde{M}_{zn}=\frac{1}{2}[j^{-(4k+1)}\tilde{M}_{zn}j+\tilde{M}_{zn}]=\tilde{M}_{zn}. \tag{2.3.11}$$

For $n = 4k + 3$, we have

$$-\frac{j}{2}\tilde{M}_{yn}\mathrm{sign}(n)+\frac{1}{2}\tilde{M}_{zn}=\frac{1}{2}[-j^{4k+3}\tilde{M}_{zn}j+\tilde{M}_{zn}]=0. \tag{2.3.12}$$

For $n = -(4k + 3)$, we have

$$-\frac{j}{2}\tilde{M}_{yn}\mathrm{sign}(n)+\frac{1}{2}\tilde{M}_{zn}=\frac{1}{2}[j^{-(4k+3)}\tilde{M}_{zn}j+\tilde{M}_{zn}]=0. \tag{2.3.13}$$

To sum up, the components corresponding to $n = \pm(4k + 3)$ are zero. For $n = 4k+1$, $k \geq 0$

$$B_{z,n}(x,y,z)+B_{z,-n}(x,y,z)=\mu_0\tilde{M}_{zn}(1-e^{-\gamma_n\Delta})e^{-z\gamma_n}(e^{-j\frac{2\pi n}{L}y}+e^{-j\frac{2\pi(-n)}{L}y}) \tag{2.3.14}$$

$$B_{z,n}(x,y,z)+B_{z,-n}(x,y,z)=2\mu_0\tilde{M}_{zn}(1-e^{-\gamma_n\Delta})e^{-z\gamma_n}\cos(\frac{2\pi n}{L}y). \tag{2.3.15}$$

In this case, if k is even, (2.3.6) and (2.3.15) yield the following

$$B_{z,n}(x,y,z)+B_{z,-n}(x,y,z)=2\mu_0\frac{\sqrt{2}M_0}{\pi n}(1-e^{-\gamma_n\Delta})e^{-z\gamma_n}\cos(\frac{2\pi n}{L}y). \tag{2.3.16}$$

With k odd, (2.3.7) and (2.3.15) yield the following:

$$B_{z,n}(x,y,z)+B_{z,-n}(x,y,z)=-2\mu_0\frac{\sqrt{2}M_0}{\pi n}(1-e^{-\gamma_n\Delta})e^{-z\gamma_n}\cos(\frac{2\pi n}{L}y). \tag{2.3.17}$$

Finally, the z-component magnetic flux density is figured out as below, with $n = 4k+1$,

$$B_z(x,y,z)=\sum_{n=1}^{+\infty}[B_{z,n}(x,y,z)+B_{z,-n}(x,y,z)], \tag{2.3.18}$$

$$B_z(x,y,z)=\sum_{k=0}^{+\infty}(-1)^k 2\mu_0\frac{\sqrt{2}M_0}{\pi n}(1-e^{-\gamma_n\Delta})e^{-\gamma_n z}\cos(\frac{2\pi n}{L}y). \tag{2.3.19}$$

Now we consider two single-side Halbach magnet arrays *A* and *B* being superimposed to yield a resultant magnetic field. Array B generates magnetic flux density components in the *z*-direction and the *x*-direction. The *z*-direction magnetic flux density at a point (*x*, *y*, *z*) is the sum of magnetic flux densities generated by array *A* and array *B* at this point. The total field solution for *z*-component magnetic flux density is

$$\begin{aligned} &B_z(x,y,z) = B_{Az} + B_{Bz} = \\ &= \sum_{k=0}^{+\infty} (-1)^k 2\mu_0 \frac{\sqrt{2}M_0}{\pi n}(1-e^{-\gamma_n \Delta})e^{-\gamma_n z}\cos(\frac{2\pi n}{L}y) \\ &+ \sum_{k=0}^{+\infty} (-1)^k 2\mu_0 \frac{\sqrt{2}M_0}{\pi n}(1-e^{-\gamma_n \Delta})e^{-\gamma_n z}\cos(\frac{2\pi n}{L}x) \end{aligned} \tag{2.3.20}$$

$n = 4k+1$.

A 3-D plot of the *z*-component resultant magnetic flux density on the plane $z = 0.003$ m is given in Figure 2-4.

2.3.2 Field solution for the *y*-component magnetic flux density

According to (2.3.5)

$$\tilde{B}_{y,n}(x,y,z) = \mu_0[-\frac{1}{2}\tilde{M}_{yn} - \frac{j}{2}\tilde{M}_{zn}\text{sign}(n)](1-e^{-\gamma_n \Delta})e^{-\gamma_n z}.$$

Denoting again *k* as a non-negative integer, for $n = 4k + 1$, we have

$$-\frac{1}{2}\tilde{M}_{yn} - \frac{j}{2}\tilde{M}_{zn}\text{sign}(n) = -\frac{j^{4k+1}}{2}\tilde{M}_{zn} - \frac{j}{2}\tilde{M}_{zn} = -j\tilde{M}_{zn}. \tag{2.3.21}$$

For $n = -(4k + 1)$

$$-\frac{1}{2}\tilde{M}_{yn} - \frac{j}{2}\tilde{M}_{zn}\text{sign}(n) = -\frac{j^{-(4k+1)}}{2}\tilde{M}_{zn} + \frac{j}{2}\tilde{M}_{zn} = j\tilde{M}_{zn}. \tag{2.3.22}$$

For $n = 4k + 3$, we have

$$-\frac{1}{2}\tilde{M}_{yn}-\frac{j}{2}\tilde{M}_{zn}\text{sign}(n)=-\frac{j^{4k+3}}{2}\tilde{M}_{zn}-\frac{j}{2}\tilde{M}_{zn}=0. \tag{2.3.23}$$

For $n=-(4k+3)$, $n<0$, we have

$$-\frac{1}{2}\tilde{M}_{yn}-\frac{j}{2}\tilde{M}_{zn}\text{sign}(n)=-\frac{j^{-(4k+3)}}{2}\tilde{M}_{zn}+\frac{j}{2}\tilde{M}_{zn}=0 \tag{2.3.24}$$

To sum up, the components corresponding to $n=\pm(4k+3)$ are zero. For $n=4k+1$, $k\geq 0$

$$B_{y,n}(x,y,z)+B_{y,-n}(x,y,z)=\mu_0\tilde{M}_{zn}(1-e^{-\gamma_n\Delta})e^{-z\gamma_n}(-je^{-j\frac{2\pi n}{L}y}+je^{-j\frac{2\pi(-n)}{L}y}), \tag{2.3.25}$$

$$B_{y,n}(x,y,z)+B_{y,-n}(x,y,z)=-2\mu_0\tilde{M}_{zn}(1-e^{-\gamma_n\Delta})e^{-z\gamma_n}\sin(\frac{2\pi n}{L}y). \tag{2.3.26}$$

In this case, if k is even, (2.3.6) and (2.3.26) yield the following

$$B_{y,n}(x,y,z)+B_{y,-n}(x,y,z)=-2\mu_0\frac{\sqrt{2}M_0}{\pi n}(1-e^{-\gamma_n\Delta})e^{-z\gamma_n}\sin(\frac{2\pi n}{L}y). \tag{2.3.27}$$

With k odd, (2.3.7) and (2.3.26) yield the following

$$B_{y,n}(x,y,z)+B_{y,-n}(x,y,z)=2\mu_0\frac{\sqrt{2}M_0}{\pi n}(1-e^{-\gamma_n\Delta})e^{-z\gamma_n}\sin(\frac{2\pi n}{L}y). \tag{2.3.28}$$

Finally, the y-component magnetic flux density is, with $n=4k+1$,

$$B_y(x,y,z)=\sum_{n=1}^{+\infty}[B_{y,n}(x,y,z)+B_{y,-n}(x,y,z)], \tag{2.3.29}$$

$$B_y(x,y,z)=\sum_{k=0}^{+\infty}(-1)^{k+1}2\mu_0\frac{\sqrt{2}M_0}{\pi n}(1-e^{-\gamma_n\Delta})e^{-\gamma_n z}\sin(\frac{2\pi n}{L}y), \tag{2.3.30}$$

Since the x-axis Halbach magnet array does not generate the y-component magnetic flux density, the resultant y-component magnetic flux density generated by the superimposed Halbach magnet matrix is the y-component magnetic flux density generated by the y-axis Halbach magnet array. The 3-D plot of the y-component

magnetic flux density in Figure 2-6 below is drawn with the two harmonics of n = 1 and n = 5.

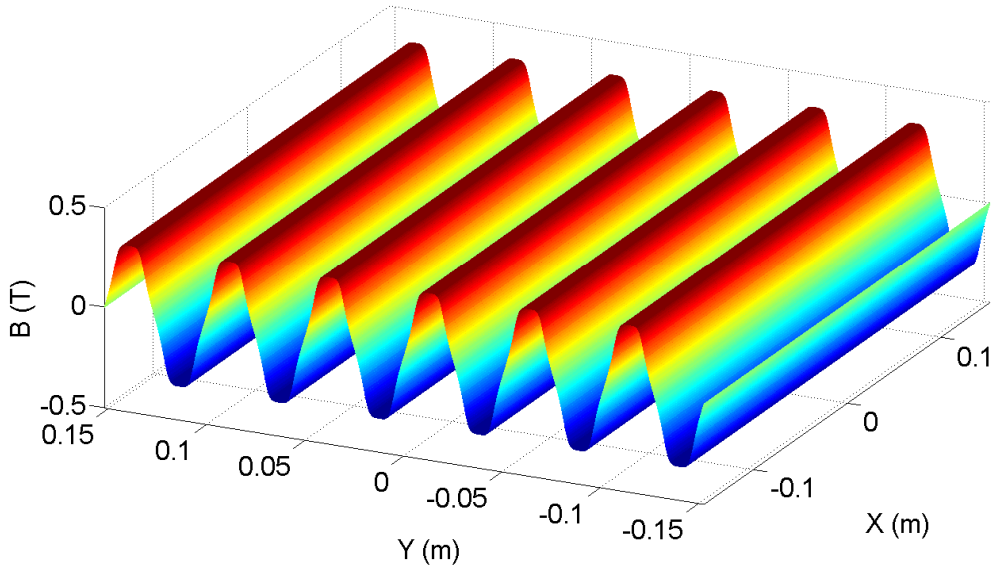

Figure 2-6: The 3-D plot of the *y*-component magnetic flux density on the plane at $z = 0.003$ m.

2.3.3 Field solution for the *x*-direction magnetic flux density

By a similar way as the derivation of the field solution for the *y*-component magnetic flux density generated by the superimposed Halbach magnet matrix, we have the equivalent result for the *x*-component magnetic flux density

$$B_x(x,y,z) = \sum_{k=0}^{+\infty} (-1)^{k+1} 2\mu_0 \frac{\sqrt{2}M_0}{\pi n}(1-e^{-\gamma_n \Delta})e^{-\gamma_n z}\sin(\frac{2\pi n}{L}x) \quad , \tag{2.3.31}$$

$n = 4k+1$.

The 3-D plot of the *x*-component magnetic flux density in Figure 2-7 below is drawn with the two harmonics of $n = 1$ and $n = 5$.

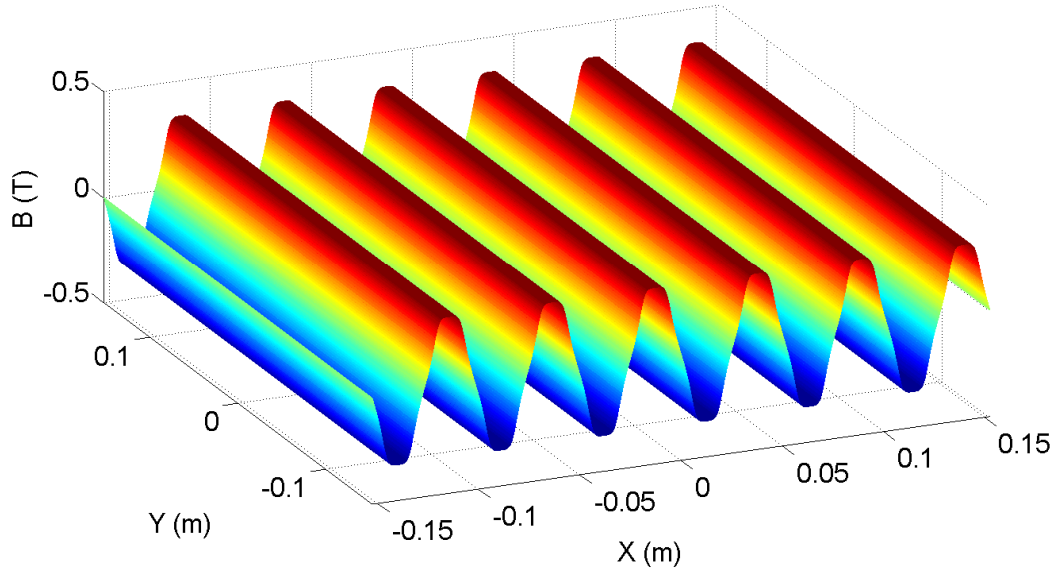

Figure 2-7: The 3-D plot of the x-component magnetic flux density on the plane at $z = 0.003$ m.

2.4 Force acting on a coil side due to B_z and the x-directed current

Assume that we have a coil being placed in the magnetic field of the superimposed Halbach magnet array so that the sides of the coil are parallel to the edges of the magnet matrix. Flowing a current i in the coil, we calculate the electromagnetic forces acting on the coil due to different components of magnetic flux density. Ignoring the curve parts, the coil is divided into 4 right-rectangular-prism sides. The calculation of the force acting on each coil side is based on the electric current, the field solution, the dimensions of the coil side and the position of a point fixed to the coil side, namely the base point. This subsection investigates the electromagnetic force acting on a right-rectangular-prism part of the coil where the electric current is flowing in the x-direction.

The resultant z-direction magnetic flux density component is recalled as

$$B_z(x,y,z) = B_{Az} + B_{Bz} =$$
$$= \sum_{k=0}^{+\infty} (-1)^k 2\mu_0 \frac{\sqrt{2}M_0}{\pi n}(1-e^{-\gamma_n \Delta})e^{-\gamma_n z}\cos(\frac{2\pi n}{L}y) \qquad (2.4.1)$$
$$+\sum_{k=0}^{+\infty} (-1)^k 2\mu_0 \frac{\sqrt{2}M_0}{\pi n}(1-e^{-\gamma_n \Delta})e^{-\gamma_n z}\cos(\frac{2\pi n}{L}x)$$

$n = 4k+1$.

We denote

$$B_z(x,y,z) = B_{Az} + B_{Bz} =$$
$$= \sum_{k=0}^{+\infty} B_{Azn}\cos(\frac{2\pi n}{L}y) + \sum_{k=0}^{+\infty} B_{Bzn}\cos(\frac{2\pi n}{L}x) \qquad (2.4.2)$$

$n = 4k+1$,

where $B_{Azn} = B_{Bzn} = (-1)^k 2\mu_0 \frac{\sqrt{2}M_0}{\pi n}(1-e^{-\gamma_n \Delta})e^{-\gamma_n z}$. (2.4.3)

We calculate the force component F_{3yn} acting on the coil side due to the nth-order component in the expansion of $B_z(x, y, z)$, which is

$$B_{z,n} = B_{Azn}\cos(\frac{2\pi n}{L}y) + B_{Bzn}\cos(\frac{2\pi n}{L}x). \qquad (2.4.4)$$

The right-rectangular-prism part of the coil has the length l along the x-axis, the width w along the y-axis and the height h along the z-axis.

First, we consider the force F_{1yn} acting on a segment of a single coil turn due to $B_{z,n}$. The segment is parallel to the x-axis with the current i being flowed to the positive x-direction.

$$d\boldsymbol{F}_{1yn} = idx\boldsymbol{i}_x \times B_{z,n}(x,y,z)\boldsymbol{i}_z = -idxB_{z,n}(x,y,z)\boldsymbol{i}_y \qquad (2.4.5)$$

$$F_{1yn} = -\int_{x}^{x+l} iB_{z,n}(x,y,z)dx = -i\int_{x}^{x+l}[B_{Azn}\cos(\frac{2\pi n}{L}y) + B_{Bzn}\cos(\frac{2\pi n}{L}x)]dx$$

$$= -ilB_{Azn}\cos(\frac{2\pi n}{L}y) - iB_{Bzn}\frac{L}{2\pi n}\sin(\frac{2\pi n}{L}x)\Big|_{x}^{x+l}$$

$$= -ilB_{Azn}\cos(\frac{2\pi n}{L}y) - iB_{Bzn}\frac{L}{2\pi n}[\sin(\frac{2\pi n}{L}(x+l)) - \sin(\frac{2\pi n}{L}x)]$$

$$= -ilB_{Azn}\cos(\frac{2\pi n}{L}y) - iB_{Bzn}\frac{L}{\pi n}\cos(\frac{2\pi n}{L}(x+l/2))\sin(\frac{\pi nl}{L}) \quad (2.4.6)$$

$$\boldsymbol{F}_{1yn} = F_{1yn}\boldsymbol{i}_{y} \quad (2.4.7)$$

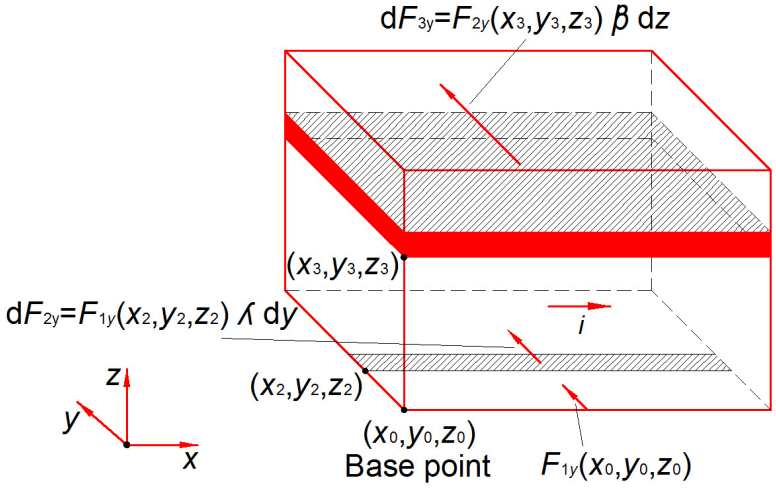

Figure 2-8: The scheme to calculate the electromagnetic force by volume integration.

We denote F_{2yn} as the force due to $B_{z,n}$ acting on the rectangular bottom surface of the right-rectangular-prism coil side. The rectangular bottom surface, which contains the point (x_0, y_0, z_0) as in Figure 2-8, is parallel to the plane xy and has length l and width w. The turn density of the coil along the width w is λ.

$$d\boldsymbol{F}_{2yn}(x,y,z) = \boldsymbol{F}_{1yn}(x,y,z)\lambda dy \tag{2.4.8}$$

$$dF_{2yn}(x,y,z) = F_{1yn}(x,y,z)\lambda dy \tag{2.4.9}$$

$$F_{2yn}(x,y,z) = \int_{y}^{y+w} F_{1yn}(x,y,z).\lambda dy =$$

$$= -\int_{y}^{y+w} \{ilB_{Azn}\cos(\frac{2\pi n}{L}y) + iB_{Bzn}\frac{L}{\pi n}\cos[\frac{2\pi n}{L}(x+\frac{l}{2})]\sin(\frac{\pi n}{L}l)\}\lambda dy$$

$$= -iB_{Bzn}\frac{L}{\pi n}\cos[\frac{2\pi n}{L}(x+\frac{l}{2})]\sin(\frac{\pi n}{L}l)\lambda w - \int_{y}^{y+w} ilB_{Azn}\cos(\frac{2\pi n}{L}y)\lambda dy$$

$$= -iB_{Bzn}\frac{L}{\pi n}\cos[\frac{2\pi n}{L}(x+\frac{l}{2})]\sin(\frac{\pi n}{L}l)\lambda w$$

$$-ilB_{Azn}\frac{L}{\pi n}\lambda\cos[\frac{2\pi n}{L}(y+\frac{w}{2})]\sin(\frac{\pi n}{L}w) \tag{2.4.10}$$

We denote F_{3yn} as the force acting on the rectangular cube of the coil that has length l, width w and height h.

$$d\boldsymbol{F}_{3yn}(x,y,z) = \boldsymbol{F}_{2yn}(x,y,z)\beta dz \tag{2.4.11}$$

$$dF_{3yn}(x,y,z) = F_{2yn}(x,y,z)\beta dz \tag{2.4.12}$$

β is the turn density of the coil along the height h.

$$F_{3yn}(x,y,z) = \int_{z}^{z+h} F_{2yn}(x,y,z)\beta dz \tag{2.4.13}$$

$$F_{3yn}(x,y,z) = -\frac{iL\lambda w}{\pi n}\cos[\frac{2\pi n}{L}(x+\frac{l}{2})]\sin(\frac{\pi n}{L}l)\int_{z}^{z+h} B_{Bzn}\beta dz$$

$$-\frac{ilL\lambda}{\pi n}\cos[\frac{2\pi n}{L}(y+\frac{w}{2})]\sin(\frac{\pi n}{L}w)\int_{z}^{z+h} B_{Azn}\beta dz \tag{2.4.14}$$

Equation (2.4.3) is

$$B_{Azn} = B_{Bzn} = (-1)^k 2\mu_0 \frac{\sqrt{2}M_0}{\pi n}(1-e^{-\gamma_n \Delta})e^{-\gamma_n z}.$$

From these, we have

$$\begin{cases} \int_z^{z+h} B_{Bzn}\beta dz = B_{Bzn}\beta \frac{-1}{\gamma_n}|_z^{z+h} = \frac{1}{\gamma_n} B_{Bzn}\beta(1-e^{-\gamma_n h}) \\ \int_z^{z+h} B_{Azn}\beta dz = B_{Azn}\beta \frac{-1}{\gamma_n}|_z^{z+h} = \frac{1}{\gamma_n} B_{Azn}\beta(1-e^{-\gamma_n h}) \end{cases} \tag{2.4.15}$$

Equation (2.4.15) is substituted into (2.4.14), yielding

$$\begin{aligned} F_{3yn}(x,y,z) &= -\frac{iL\lambda w}{\pi n}\cos[\frac{2\pi n}{L}(x+\frac{l}{2})]\sin(\frac{\pi n}{L}l)[\frac{1}{\gamma_n}B_{Bzn}\beta(1-e^{-\gamma_n h})] \\ &-\frac{ilL\lambda}{\pi n}\cos[\frac{2\pi n}{L}(y+\frac{w}{2})]\sin(\frac{\pi n}{L}w)[\frac{1}{\gamma_n}B_{Azn}\beta(1-e^{-\gamma_n h})] \\ &= F_{2yn}(x,y,z)\frac{\beta}{\gamma_n}(1-e^{-\gamma_n h}) \end{aligned} \tag{2.4.16}$$

The vector $\boldsymbol{F}_{3yn}(x,y,z)$ is expressed as

$$\boldsymbol{F}_{3yn}(x,y,z) = F_{3yn}(x,y,z)\boldsymbol{i}_y = F_{2yn}(x,y,z)\frac{\beta}{\gamma_n}(1-e^{-\gamma_n h})\boldsymbol{i}_y \tag{2.4.17}$$

2.5 Force acting on a coil side due to B_y and the x-directed current

In this case, the electric current being flowed in the x-direction and the y-component magnetic flux density B_y generate a force in the z-direction, acting on the right-rectangular-prism side of the coil. From section 2.3, the field solution for the y-component magnetic flux density of the superimposed Halbach magnet matrix is

$$B_y(x,y,z) = \sum_{k=0}^{+\infty}(-1)^{k+1}2\mu_0 \frac{\sqrt{2}M_0}{\pi n}(1-e^{-\gamma_n \Delta})e^{-\gamma_n z}\sin(\frac{2\pi n}{L}y), \tag{2.5.1}$$

$n = 4k + 1.$

We denote

$$B_y(x, y, z) = \sum_{k=0}^{+\infty} B_{Byn} \sin(\frac{2\pi n}{L} y), \tag{2.5.2}$$

$n = 4k + 1,$

$$B_{Byn} = (-1)^{k+1} 2\mu_0 \frac{\sqrt{2} M_0}{\pi n} (1 - e^{-\gamma_n \Delta}) e^{-\gamma_n z}. \tag{2.5.3}$$

The nth-order harmonic in the expansion of $B_y(x, y, z)$ above is

$$B_{y,n} = B_{Byn} \sin(2\pi n y / L). \tag{2.5.4}$$

The z-component force F_{3zn} acting on the right-rectangular-prism side of the coil due to $B_{y,n}$ will be calculated. Being similar to what has been described in Subsection 2.4, the right-rectangular-prism side has length l along the x-axis, width w along the y-axis and height h along the z-axis; the current i is flowed in the coil side along the x-axis. First, the force F_{1zn} acting on a straight-line segment of a single coil turn due to $B_{y,n}$ is considered. The straight-line segment, which has the length of l, is parallel to the x-axis with the current i being flowed to the positive-x direction.

$$d\boldsymbol{F}_{1zn} = idx\boldsymbol{i}_{\boldsymbol{x}} \times B_{y,n}(x, y, z)\boldsymbol{i}_{\boldsymbol{y}} \tag{2.5.5}$$

$$dF_{1zn} = idxB_{y,n}(x, y, z) = idxB_{Byn} \sin(\frac{2\pi n}{L} y) \tag{2.5.6}$$

$$F_{1zn} = \int_{x}^{x+l} iB_{Byn} \sin(\frac{2\pi n}{L} y) dx = iB_{Byn} l \sin(\frac{2\pi n}{L} y) \tag{2.5.7}$$

$$\boldsymbol{F}_{1zn} = F_{1zn}\boldsymbol{i}_z \tag{2.5.8}$$

We denote F_{2zn} as the z-direction force acting on the rectangular bottom surface

of the coil side, which is parallel to the top surface of the magnet matrix and has the length l and the width w. The force F_{3zn} is the z-direction resultant force acting on the entire coil side. The turn density of the coil along the width w is λ.

$$d\boldsymbol{F}_{2zn}(x,y,z) = \boldsymbol{F}_{1zn}(x,y,z)\lambda dy \tag{2.5.9}$$

$$F_{2zn}(x,y,z) = \int_{y}^{y+w} F_{1zn}(x,y,z)\lambda dy \tag{2.5.10}$$

$$F_{2zn}(x,y,z) = \int_{y}^{y+w} iB_{Byn} l \sin(\frac{2\pi n}{L} y)\lambda dy \tag{2.5.11}$$

$$F_{2zn}(x,y,z) = iB_{Byn} l\lambda[-\cos(\frac{2\pi n}{L} y)]\Big|_{y}^{y+w} \frac{L}{2\pi n} \tag{2.5.12}$$

$$F_{2zn}(x,y,z) = \frac{iB_{Byn} l\lambda L}{2\pi n}\{\cos(\frac{2\pi n}{L} y) - \cos[\frac{2\pi n}{L}(y+w)]\} \tag{2.5.13}$$

$$F_{2zn}(x,y,z) = \frac{iB_{Byn} l\lambda L}{\pi n}\sin[\frac{2\pi n}{L}(y+\frac{w}{2})]\sin(\frac{\pi n w}{L}) \tag{2.5.14}$$

$$d\boldsymbol{F}_{3zn}(x,y,z) = \boldsymbol{F}_{2zn}(x,y,z)\beta dz \tag{2.5.15}$$

$$dF_{3zn}(x,y,z) = F_{2zn}(x,y,z)\beta dz \tag{2.5.16}$$

The parameter β is the turn density of the coil along the height h. By using (2.5.3), (2.5.14) and the similar derivations to obtain (2.4.16) and (2.4.17) in Subsection 2.4, we have

$$F_{3zn}(x,y,z) = \int_{z}^{z+h} F_{2zn}(x,y,z)\beta dz = F_{2zn}\frac{\beta}{\gamma_n}(1-e^{-\gamma_n h}). \tag{2.5.17}$$

The force vector $\boldsymbol{F}_{3zn}(x,y,z)$ can be expressed as

$$\boldsymbol{F}_{3zn}(x,y,z) = F_{3zn}(x,y,z)\boldsymbol{i}_z = F_{2zn}(x,y,z)\frac{\beta}{\gamma_n}(1-e^{-\gamma_n h})\boldsymbol{i}_z \tag{2.5.18}$$

2.6 Total force acting on a single coil

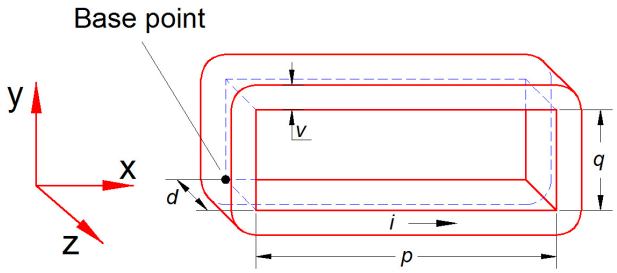

Figure 2-9: Perspective view of a coil with its dimensions, z is the vertical axis.

This section is to calculate the total force acting on the entire coil due to the x, y, and z components of the resultant magnetic field generated by the superimposed Halbach magnet matrix. Ignoring the four small quarter-cylindrical parts, we calculate the electromagnetic forces acting on four right-rectangular-prism sides with the base points noted in Figures 2-9 and 2-10. The base point to calculate the force is the point at the inner corner of the coil with lowest x, y, and z. In practice, the coil has a small curve at every inner corner; the base point is the intersection of two inner edges of the bottom surface of the coil.

The total force acting on the coil in x, y, or z depends on the field solution, the size of the coil, and the base point (x_1, y_1, z_1) of the coil. However, when deriving the calculation for forces acting on the coil sides, in order to apply what has been derived in

Subsections 2.4 and 2.5, it is required to specify a base point for each coil side. That is why Figure 2-10 is given. Table 1-1 gives the overview of the contributions of the forces due to different magnetic flux density components B_x, B_y and B_z with the electric current flowing in the coil sides.

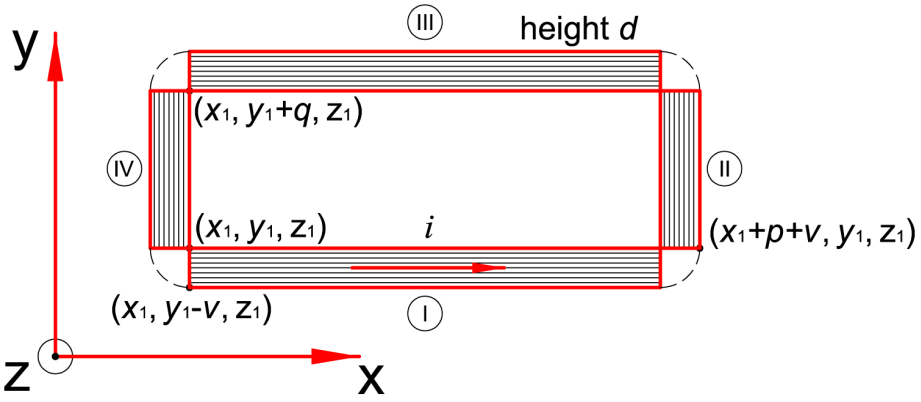

Figure 2-10: A coil with the base points to calculate the forces for its rectangular sides.

Table 1-1: Force contributions of the sides of a coil

Magnetic flux density / Coil side	B_x	B_y	B_z
I		$\boldsymbol{F}_{3z}^{I}$, in z-direction	$\boldsymbol{F}_{3y}^{I}$, in y-direction
II	$\boldsymbol{F}_{3z}^{II}$, in z-direction		$\boldsymbol{F}_{3x}^{II}$, in x-direction
III		$\boldsymbol{F}_{3z}^{III}$, in z-direction	$\boldsymbol{F}_{3y}^{III}$, in y-direction
IV	$\boldsymbol{F}_{3z}^{IV}$, in z-direction		$\boldsymbol{F}_{3x}^{IV}$, in x-direction

2.6.1 Force acting on a single coil in the *x*-direction

Being similar to (2.4.10) and (2.4.17), the *x*-direction force due to the magnetic flux density component $B_{z,n}$ acting on the coil side II in Figure 2.10 is figured out as:

$$\boldsymbol{F}_{3xn}^{II} = -\frac{i\lambda L}{\pi n}\left\{ B_{Bzn}(z_1)v\cos(\frac{2\pi n}{L}y_1 + \frac{\pi n}{L}q)\sin(\frac{\pi n}{L}q) + \right.$$
$$\left. + B_{Azn}(z_1)q\cos[-\frac{2\pi n}{L}(x_1 + p + v) + \frac{\pi n}{L}v]\sin(\frac{\pi n}{L}v)\right\}\frac{\beta}{\gamma_n}(1-e^{-\gamma_n d})\boldsymbol{i}_{\boldsymbol{x}} \tag{2.6.1}$$

It is noticeable that the base point, in this case, is (x_1+p+v, y_1, z_1). The current is actually flowed in the *y*-direction so that we replace *x* and *y* in (2.4.10) and (2.4.17) with y_1 and $-x_1$, respectively. The force in the *x*-direction due to $B_{z,n}$ acting on the coil side IV is

$$\boldsymbol{F}_{3xn}^{IV} = \frac{i\lambda L}{\pi n}\left\{ B_{Bzn}(z_1)v\cos(\frac{2\pi n}{L}y_1 + \frac{\pi n}{L}q)\sin(\frac{\pi n}{L}q)\right.$$
$$\left. + B_{Azn}(z_1)q\cos(-\frac{2\pi n}{L}x_1 + \frac{\pi n}{L}v)\sin(\frac{\pi n}{L}v)\right\}\frac{\beta}{\gamma_n}(1-e^{-\gamma_n d})\boldsymbol{i}_{\boldsymbol{x}}\,. \tag{2.6.2}$$

In this case, the current flows in a reverse direction in comparison with that of the coil side II. The base point now is (x_1, y_1, z_1). From (2.6.1) and (2.6.2), the resultant force in the *x*-direction acting on the coil is

$$\boldsymbol{F}_{3xn}^{Coil} = \boldsymbol{F}_{3xn}^{II} + \boldsymbol{F}_{3xn}^{IV}. \tag{2.6.3}$$

It is noticeable that if p+v = L, this resultant force is zero.

2.6.2 Force acting on a single coil in the *y*-direction

From (2.4.10) and (2.4.17), the force in the *y*-direction due to $B_{z,n}$ acting on the rectangular side I, with the base point (x_1, y_1-v, z_1), is

$$\boldsymbol{F}_{3yn}^{I} = -\frac{i\lambda L}{\pi n}\Big\{B_{Bzn}(z_1)v\cos(\frac{2\pi n}{L}x_1+\frac{\pi n}{L}p)\sin(\frac{\pi n}{L}p)$$

$$+B_{Azn}(z_1)p\cos[\frac{2\pi n}{L}(y_1-v)+\frac{\pi n}{L}v]\sin(\frac{\pi n}{L}v)\Big\}\frac{\beta}{\gamma_n}(1-e^{-\gamma_n d})\boldsymbol{i}_y . \tag{2.6.4}$$

The force in the *y*-direction due to B_{zn} acting on the rectangular cube III, with the base point (x_1, y_1+q, z_1), is

$$\boldsymbol{F}_{3yn}^{III} = \frac{i\lambda L}{\pi n}\Big\{B_{Bzn}(z_1)v\cos(\frac{2\pi n}{L}x_1+\frac{\pi n}{L}p)\sin(\frac{\pi n}{L}p)$$

$$+B_{Azn}(z_1)p\cos[\frac{2\pi n}{L}(y_1+q)+\frac{\pi n}{L}v]\sin(\frac{\pi n}{L}v)\Big\}\frac{\beta}{\gamma_n}(1-e^{-\gamma_n d})\boldsymbol{i}_y . \tag{2.6.5}$$

The total force in y direction due to B_{zn} acting on the coil is

$$\boldsymbol{F}_{3yn}^{coil} = \boldsymbol{F}_{3yn}^{I} + \boldsymbol{F}_{3yn}^{III} \tag{2.6.6}$$

2.6.3 Force acting on a single coil in the *z*-direction

From (2.5.14) and (2.5.18), the force due to $B_{y,n}$, acting on the right-rectangular-prism side I, with the base point (x_1, y_1-v, z_1), is

$$\boldsymbol{F}_{3zn}^{I} = \frac{iL\lambda pB_{Ayn}(z_1)}{\pi n}\sin[\frac{2\pi n}{L}(y_1-\frac{v}{2})]\sin(\frac{\pi nv}{L})\frac{\beta}{\gamma_n}(1-e^{-\gamma_n d})\boldsymbol{i}_z . \tag{2.6.7}$$

The force due to $B_{y,n}$, acting on the rectangular side III with the base point (x_1, y_1+q, z_1) is

$$\boldsymbol{F}_{3zn}^{III} = -\frac{iL\lambda pB_{Ayn}(z_1)}{\pi n}\sin[\frac{2\pi n}{L}(y_1+q+\frac{v}{2}]\sin(\frac{\pi nv}{L})\frac{\beta}{\gamma_n}(1-e^{-\gamma_n d})\boldsymbol{i}_z . \tag{2.6.8}$$

The force due to $B_{x,n}$, acting on the right-rectangular-prism side II, is

$$\boldsymbol{F}_{3zn}^{II} = \frac{iL\lambda qB_{Bxn}(z_1)}{\pi n}\sin[-\frac{2\pi n}{L}(x_1 + p + \frac{v}{2})]\sin(\frac{\pi nv}{L})\frac{\beta}{\gamma_n}(1-e^{-\gamma_n d})\boldsymbol{i}_z . \tag{2.6.9}$$

The force due to $B_{x,n}$, acting on the right-rectangular-prism side IV, is

$$\boldsymbol{F}_{3zn}^{IV} = -\frac{iL\lambda qB_{Bxn}(z_1)}{\pi n}\sin[-\frac{2\pi n}{L}(x_1 - \frac{v}{2})]\sin(\frac{\pi nv}{L})\frac{\beta}{\gamma_n}(1-e^{-\gamma_n d})\boldsymbol{i}_z . \tag{2.6.10}$$

The total force due to $B_{x,n}$ and $B_{y,n}$, acting on the coil in the z-direction is

$$\boldsymbol{F}_{3zn}^{coil} = \boldsymbol{F}_{3zn}^{I} + \boldsymbol{F}_{3zn}^{III} + \boldsymbol{F}_{3zn}^{II} + \boldsymbol{F}_{3zn}^{IV} . \tag{2.6.11}$$

CHAPTER III

ELECTROMECHANICAL DESIGN OF THE MOVING PLATEN

3.1 Electromagnetic design

3.1.1 Coil design

On a plane parallel to the surface of the superimposed Halbach magnet matrix, the *x*-component and the *y*-component magnetic flux densities B_x and B_y vary periodically along the *x*-direction and the *y*-direction, respectively. In two opposite sides of a rectangular coil, an electric current flows in two opposite directions. If we design the size of the coil so that magnetic flux density in one side and in the other side of the coil can be in reverse, the electromagnetic force can be added up to be stronger. For this purpose, the distance between 2 longer sides of a rectangular coil is designed to be a half of a spatial period of the superimposed Halbach magnet matrix. Figure 3-1 below illustrates this feature. The red rectangles are the cross sections of the two opposite sides of a coil with current flowing in opposite directions. The electromagnetic forces acting on the two sides are in the same direction.

From the argument above and with reference to Figure 2-9 we have a distance ($p+v$) or ($q+v$) is $L/2$. Without losing generalization, we choose ($q+v$) as $L/2$. If ($p+v$) is not a multiple of L, all four sides always present in every force allocation of the coil. This makes the force calculation for a single coil complicated and time-consuming. A coil generating all force components in *x*, *y*, and *z,* leads to complication and conflicts in

force allocation, and, therefore, increases the calculation time of the force-current relation for the entire moving platen. The problem gets worse when the moving platen only requires one force component to move in one direction x or y.

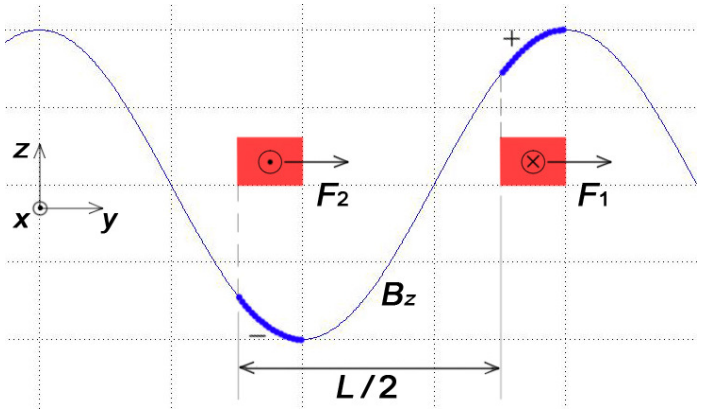

Figure 3-1: Illustration of forces acting on two sides of a coil with a distance of $L/2$.

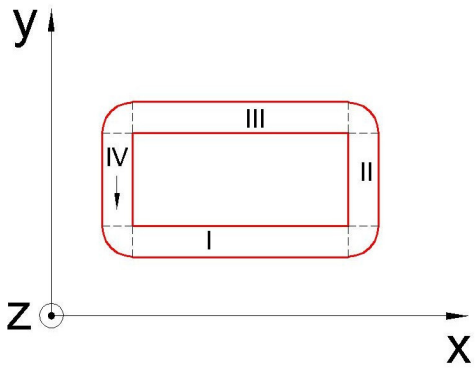

Figure 3-2: Numbering the sides of a coil.

With $p+v = L$, when a coil is placed so that its sides are parallel to the surface of the superimposed Halbach magnet matrix, the forces acting on the shorter sides of the

coils, II and IV as in Figure 3-2, always cancel out. This is because the magnetic flux densities at the two shorter sides, which have a distance of L from each other, are equal and the currents are opposite in directions. A coil being placed as discussed above generates two force components, one in the vertical direction, and another one in a horizontal direction perpendicular to the longer sides of the coil. The two forces in the direction parallel to the longer sides of a coil, which act on the shorter coil sides, cancel out.

By increasing the thickness v and the height d, the force acting on the coil is raised; however, the mass of the coil, and therefore, the mass of the moving platen is also increased. With considerations about this, and about wire diameter, number of turns, bending radius at inner corners, all dimension parameters for the coils are chosen and given in Figure 3-3.

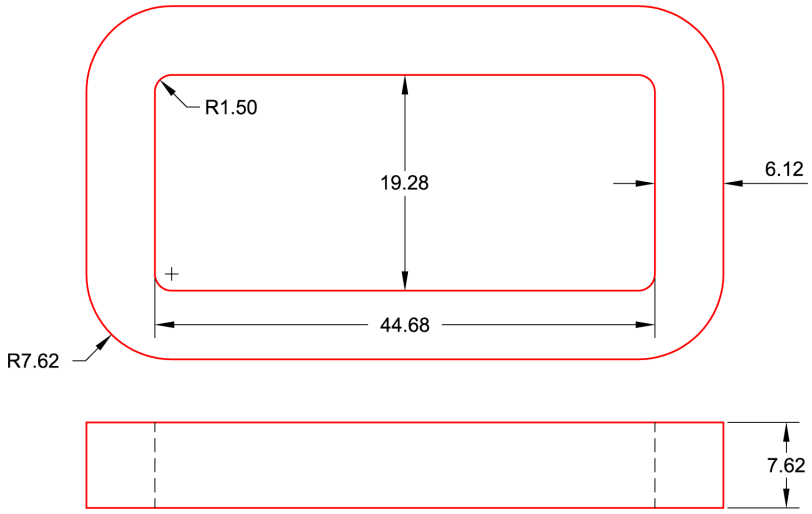

Figure 3-3: The coil size, unit: mm.

Following are specifications of the wire and the coils:

- Wire type: Heavy-build AWG #24 heat bondable wire,
- Wire diameter: 0.0213 inch.
- Number of turns: 156
- Coil resistance: 1.98 Ω
- Coil inductance: 1.28 mH

3.1.2 Coils arrangement in the moving platen

For any rectangular coil size, when the coil is placed so that its sides are parallel to the edges of the superimposed Halbach magnet matrix, there must be a case in which the two opposite coil sides are placed symmetrically about a peak of the z-direction magnetic flux density component. Because the electric currents flowing in these two sides are equal in magnitude but opposite in direction, the resultant horizontal force generated by these two sides is zero, no matter how big the current is. Especially, with the distance of $L/2$ between the longer coil sides, when the coil is placed symmetrically about a peak of the z-direction magnetic flux density component as in Figure 3-4, both electromagnetic forces acting on the two longer coil sides are zero.

The problem even occurs when a coil gets close to a position that the magnetic flux density distributes equally in two longer sides of the coil. In order to maintain a certain force, the current in the coil must be very large, exceeding the limit of the power amplifier circuits. The only way to overcome this problem is to use two coils placed in parallel in a way that when a coil cannot generate a force in a desired direction, the other

coil can do that. When a coil is in the position that the resultant force generated by its two longer sides is zero, the other coil should be able to generate the maximum force that a single coil can do. For this reason, the two coils are placed so that one leads the other 3*L*/4 along the direction that they are expected to generate a force in. Figure 3-5 illustrates this method. This set of two coils is a 2-phase motor with 270° phase difference.

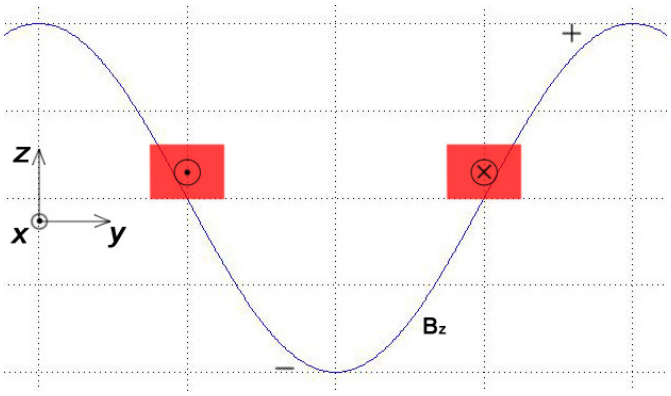

Figure 3-4: The position where two electromagnetic forces acting on the longer sides of the coil are both zero.

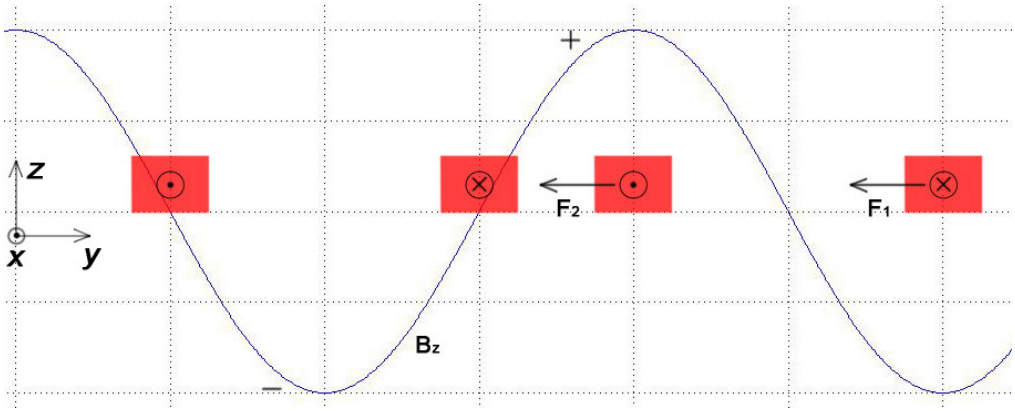

Figure 3-5: Collaboration of two coils to generate a force in a horizontal direction.

With two independent currents flowed into two coils placed as above, this set of two coils can generate a resultant force in a horizontal direction and a resultant force in the vertical direction. Three sets with two coils per set can generate the forces to move the platen in 3-DOF motions. Figure 3-6 shows the relative positions of three sets of coils for the moving platen. The set of coils 5 and 6 as noted in the figure shown on page 52 is a 2-phase motor with 450° phase difference.

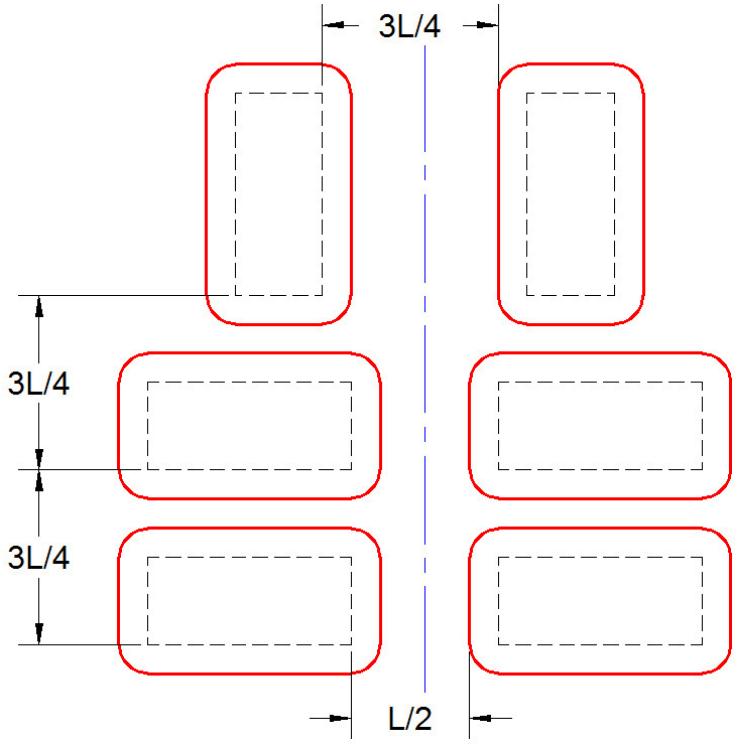

Figure 3-6: Arrangement of the six coils.

3.2 Electric current-force relation for the moving platen

This subsection is to derive the transformation between the electric currents flowed in to the six coils and the resultant electromagnetic forces acting on the moving platen. The following are the quantities and parameters that are used in this subsection:

- *xyz* is an stationary coordinate system which is fixed to the magnet matrix. This is the coordinate system used to derive the field solution in Subsection 2.3.
- *x'y'z'* is a coordinate system with the origin at the center of mass of the moving platen and the axes *x'*, *y'*, *z'* parallel to *x*, *y*, *z*, respectively.
- F_{xj} is the force acting on coil *j* along the *x*-axis; T_{zj} is the torque acting on the platen, with respect to the *z'*-axis, generated by the forces acting on coil *j*.
- v = 6.12 mm, the thickness of a coil.
- d = 7.62 mm, the height of a coil.
- p = 44.68 mm, $(p + v) = L$ is one pitch of the magnet matrix, and is also the distance between the two parallel shorter sides of a coil.
- q = 19.28 mm, $(q + v) = L/2$ is the distance between the two parallel longer sides of a coil.
- λ = 1968.50 is number of turns per meter along the thickness of a coil.
- β = 1711.74 is number of turns per meter along the height of a coil.
- i_j is the electric current flowed in the coil *j*. The coils are numbered in Figure 3-7.
- (x_j, y_j, z_j) is the base point of the coil *j*, as in Figure 3-7. The base point of a coil is defined in Subsection 2.6.

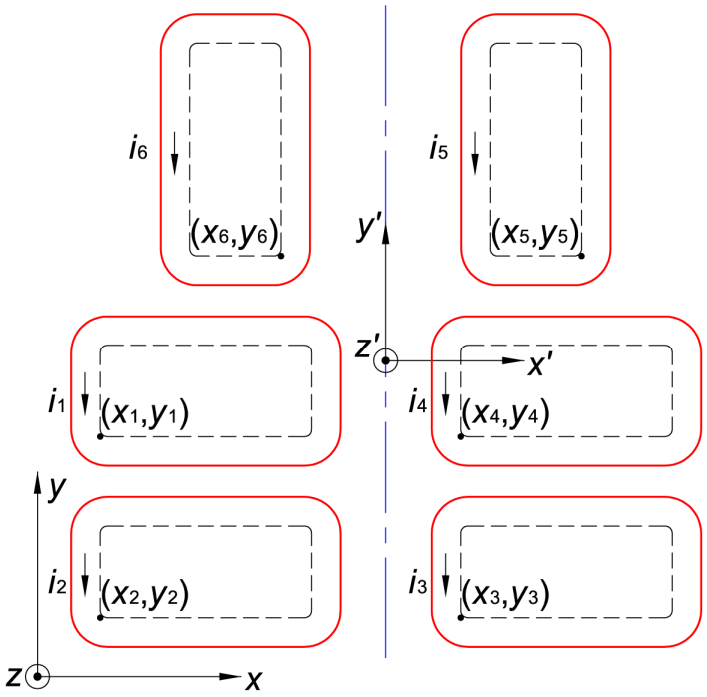

Figure 3-7: Declaring the coordinate systems, the coil number and base points for the force calculation.

3.2.1 Forces acting on the platen in the *x*-direction

For the x-direction electromagnetic force acting on the coil 6, from the result of Subsection 2.6.2, we replace x_1 and y_1 by y_6 and $-x_6$, respectively, giving

$$\boldsymbol{F}_{x6} =$$

$$= i_6 \frac{L\lambda\beta p}{\pi\gamma_1} B_{Bz1}(z_1)\sin(\frac{\pi v}{L})(1-e^{-\gamma_1 d})\{-\cos[\frac{2\pi}{L}(-x_6-\frac{v}{2})]+\cos[\frac{2\pi}{L}(-x_6+q+\frac{v}{2})]\}\boldsymbol{i}_x$$

$$= -2i_6 \frac{L\lambda\beta p}{\pi\gamma_1} B_{Bz1}(z_1)\sin(\frac{\pi v}{L})(1-e^{-\gamma_1 d})\cos[\frac{2\pi}{L}(x_6+\frac{v}{2})]\boldsymbol{i}_x$$

$$= 2i_6 b_{x6}\boldsymbol{i}_x, \qquad (3.2.1)$$

$$b_{x6} = -\frac{L\lambda\beta p}{\pi\gamma_1} B_{Bz1}(z_1)\sin(\frac{\pi v}{L})(1-e^{-\gamma_1 d})\cos[\frac{2\pi}{L}(x_6+\frac{v}{2})]. \quad (3.2.2)$$

In order to figure out the electromagnetic force acting coil the coil 5, we replace x_6 in the case of coil 6 by (x_6+5L/4), as in Figures 3-6 and 3-7.

$$\boldsymbol{F}_{x5} =$$

$$= -2i_5 \frac{L\lambda\beta p}{\pi\gamma_1} B_{Bz1}(z_1)\sin(\frac{\pi v}{L})(1-e^{-\gamma_1 d})\cos[\frac{2\pi}{L}(x_6+\frac{5L}{4}+\frac{v}{2})]\boldsymbol{i}_x$$

$$= 2i_5 \frac{L\lambda\beta p}{\pi\gamma_1} B_{Bz1}(z_1)\sin(\frac{\pi v}{L})(1-e^{-\gamma_1 d})\sin[\frac{2\pi}{L}(x_6+\frac{v}{2})]\boldsymbol{i}_x$$

$$= 2i_5 b_{x5}\boldsymbol{i}_x \quad (3.2.3)$$

$$b_{x5} = \frac{L\lambda\beta p}{\pi\gamma_1} B_{Bz1}(z_1)\sin(\frac{\pi v}{L})(1-e^{-\gamma_1 d})\sin[\frac{2\pi}{L}(x_6+\frac{v}{2})] \quad (3.2.4)$$

Total force acting on the moving platen in the x-direction: $\boldsymbol{F}_x = 2(i_5 b_{x5} + i_6 b_{x6})\boldsymbol{i}_x$ (3.2.5)

3.2.2 Forces acting on the platen in the *y*-direction

In order to figure out the force acting on the coil 1 in the y-direction, the result of the Subsection 2.6.2 is used.

$$\boldsymbol{F}_{y1} =$$

$$= i_1 \frac{L\lambda\beta p}{\pi\gamma_1} B_{Az1}(z_1)\sin(\frac{\pi v}{L})(1-e^{-\gamma_1 d})\{-\cos[\frac{2\pi}{L}(y_1-\frac{v}{2})]+\cos[\frac{2\pi}{L}(y_1+q+\frac{v}{2})]\}\boldsymbol{i}_y$$

$$= -2i_1 \frac{L\lambda\beta p}{\pi\gamma_1} B_{Az1}(z_1)\sin(\frac{\pi v}{L})(1-e^{-\gamma_1 d})\cos[\frac{2\pi}{L}(y_1-\frac{v}{2})]\boldsymbol{i}_y$$

$$= 2i_1 b_{y1}\boldsymbol{i}_y \quad (3.2.6)$$

$$b_{y1} = -\frac{L\lambda\beta p}{\pi\gamma_1} B_{Az1}(z_1) \sin(\frac{\pi v}{L})(1-e^{-\gamma_1 d}) \cos[\frac{2\pi}{L}(y_1 - \frac{v}{2})] \tag{3.2.7}$$

For the force acting on the coil 2, referring to Figure 3-6, y_1 in the force calculation for the coil 1 is replaced by (y_1−3L/4).

$$\boldsymbol{F}_{y2} = -2i_2 \frac{L\lambda\beta p}{\pi\gamma_1} B_{Az1}(z_1) \sin(\frac{\pi v}{L})(1-e^{-\gamma_1 d}) \cos[\frac{2\pi}{L}(y_1 - \frac{v}{2} - \frac{3L}{4})]\boldsymbol{i}_y$$

$$= 2i_2 \frac{L\lambda\beta p}{\pi\gamma_1} B_{Az1}(z_1) \sin(\frac{\pi v}{L})(1-e^{-\gamma_1 d}) \sin[\frac{2\pi}{L}(y_1 - \frac{v}{2})]\boldsymbol{i}_y$$

$$= 2i_2 b_{y2} \boldsymbol{i}_y \tag{3.2.8}$$

$$b_{y2} = \frac{L\lambda\beta p}{\pi\gamma_1} B_{Az1}(z_1) \sin(\frac{\pi v}{L})(1-e^{-\gamma_1 d}) \sin[\frac{2\pi}{L}(y_1 - \frac{v}{2})] \tag{3.2.9}$$

The derivation and the result for the force acting on the coil 3 are similar to those of the coil 2 because $y_3 = y_2$, as in Figure 3-7.

$$\boldsymbol{F}_{y3} = 2i_3 \frac{L\lambda\beta p}{\pi\gamma_1} B_{Az1}(z_1) \sin(\frac{\pi v}{L})(1-e^{-\gamma_1 d}) \sin[\frac{2\pi}{L}(y_1 - \frac{v}{2})]\boldsymbol{i}_y$$

$$= 2i_3 b_{y3} \boldsymbol{i}_y = 2i_3 b_{y2} \boldsymbol{i}_y \tag{3.2.10}$$

For the force acting on the coil 4, because of $y_4 = y_1$, as in Figure 3-7, with reference to (3.2.6) and (3.2.7), we have

$$\boldsymbol{F}_{y4} = -2i_4 \frac{L\lambda\beta p}{\pi\gamma_1} B_{Az1}(z_1) \sin(\frac{\pi v}{L})(1-e^{-\gamma_1 d}) \cos[\frac{2\pi}{L}(y_1 - \frac{v}{2})]\boldsymbol{i}_y$$

$$= 2i_4 b_{y4} \boldsymbol{i}_y = 2i_4 b_{y1} \boldsymbol{i}_y\,, \tag{3.2.11}$$

$$b_{y4} = b_{y1} = -\frac{L\lambda\beta p}{\pi\gamma_1} B_{Az1}(z_1) \sin(\frac{\pi v}{L})(1-e^{-\gamma_1 d}) \cos[\frac{2\pi}{L}(y_1 - \frac{v}{2})]\,. \tag{3.2.12}$$

Total force acting on the moving platen in the *y*-direction is

$$\boldsymbol{F}_y = 2(i_1 b_{y1} + i_2 b_{y2} + i_3 b_{y3} + i_4 b_{y4})\boldsymbol{i}_y \,. \tag{3.2.13}$$

3.2.3 Torque acting on the platen about the *z'*-axis

The torque acting on the platen about the *z'*-axis is generated by the forces acting on the coils 1, 2, 3 and 4 in the *y*-direction, and the forces acting on the coils 5 and 6 in the *x*-direction. The torque generated by the forces acting on the coils 1, 2, 3, and 4 in the *y*-direction is

$$T_{z1234} = T_{z1} + T_{z2} + T_{z3} + T_{z4} = \frac{3L}{2}(i_3 b_{y3} + i_4 b_{y4} - i_1 b_{y1} - i_2 b_{y2}) \,. \tag{3.2.14}$$

The torque generated by the forces acting on the coils 5 and 6 in the *x*-direction is

$$T_{z56} = T_{z5} + T_{z6} = -2(i_5 b_{x5} + i_6 b_{x6}) c_{56} \,, \tag{3.2.15}$$

where c_{56} is the distance on the horizontal plane from the center of mass of the platen to the line connecting the mid points of the longer sides of the coil 5 and the coil 6.The total torque acting on the platen with respect to the *z'*-axis is as following

$$T_z = T_{z1234} + T_{z56} = \frac{3L}{2}(i_3 b_{y3} + i_4 b_{y4} - i_1 b_{y1} - i_2 b_{y2}) - 2(i_5 b_{x5} + i_6 b_{x6}) c_{56} \,, \tag{3.2.16}$$

$$T_z = \frac{3L}{2}(-i_1 b_{y1} - i_2 b_{y2} + i_3 b_{y2} + i_4 b_{y1}) - 2(i_5 b_{x5} + i_6 b_{x6}) c_{56} \,. \tag{3.2.17}$$

3.2.4 Forces acting on the platen in the *z*-direction

In order to figure out the electromagnetic force acting on the coil 1 in the *z*-direction, the result of Subsection 2.6.3 is used.

$$\boldsymbol{F}_{z1} =$$

$$= i_1 \frac{L\lambda\beta p}{\pi\gamma_1} B_{Ay1}(z_1) \sin(\frac{\pi v}{L})(1-e^{-\gamma_1 d})\{\sin[\frac{2\pi}{L}(y_1 - \frac{v}{2})] - \sin[\frac{2\pi}{L}(y_1 + q + \frac{v}{2})]\}\boldsymbol{i}_z$$

$$= 2i_1 \frac{L\lambda\beta p}{\pi\gamma_1} B_{Ay1}(z_1) \sin(\frac{\pi v}{L})(1-e^{-\gamma_1 d}) \sin[\frac{2\pi}{L}(y_1 - \frac{v}{2})]\boldsymbol{i}_z$$

$$= 2i_1 b_{z1} \boldsymbol{i}_z , \tag{3.2.18}$$

where $b_{z1} = \frac{L\lambda\beta p}{\pi\gamma_1} B_{Ay1}(z_1) \sin(\frac{\pi v}{L})(1-e^{-\gamma_1 d}) \sin[\frac{2\pi}{L}(y_1 - \frac{v}{2})]$. (3.2.19)

For the z-direction force acting on the coil 2, referring to Figure 3-6, replacing y_1 in the case of coil 1 with ($y_1 - 3L/4$), we have

$$\boldsymbol{F}_{z2} =$$

$$= 2i_2 \frac{L\lambda\beta p}{\pi\gamma_1} B_{Ay1}(z_1) \sin(\frac{\pi v}{L})(1-e^{-\gamma_1 d}) \sin[\frac{2\pi}{L}(y_1 - \frac{3L}{4} - \frac{v}{2})]\boldsymbol{i}_z$$

$$= 2i_2 \frac{L\lambda\beta p}{\pi\gamma_1} B_{Ay1}(z_1) \sin(\frac{\pi v}{L})(1-e^{-\gamma_1 d}) \cos[\frac{2\pi}{L}(y_1 - \frac{v}{2})]\boldsymbol{i}_z$$

$$= 2i_2 b_{z2} \boldsymbol{i}_z , \tag{3.2.20}$$

where $b_{z2} = \frac{L\lambda\beta p}{\pi\gamma_1} B_{Ay1}(z_1) \sin(\frac{\pi v}{L})(1-e^{-\gamma_1 d}) \cos[\frac{2\pi}{L}(y_1 - \frac{v}{2})]$. (3.2.21)

For the coil 3, it is similar to the case of coil 2 because $y_3 = y_2$, as in Figure 3-7. We have

$$\boldsymbol{F}_{z3} = 2i_3 b_{z3} \boldsymbol{i}_z , \tag{3.2.22}$$

where $b_{z3} = b_{z2} = \frac{L\lambda\beta p}{\pi\gamma_1} B_{Ay1}(z_1) \sin(\frac{\pi v}{L})(1-e^{-\gamma_1 d}) \cos[\frac{2\pi}{L}(y_1 - \frac{v}{2})]$. (3.2.23)

For the coil 4, it is similar to the case of coil 1 because $y_4 = y_1$, as in Figure 3-7.

We have

$$\boldsymbol{F}_{z4} = 2i_4 b_{z4} \boldsymbol{i}_z , \tag{3.2.24}$$

where $b_{z4} = b_{z1} = \dfrac{L\lambda\beta p}{\pi\gamma_1} B_{Ay1}(z_1) \sin(\dfrac{\pi v}{L})(1-e^{-\gamma_1 d}) \sin[\dfrac{2\pi}{L}(y_1 - \dfrac{v}{2})]$. (3.2.25)

To calculate the electromagnetic force acting on the coil 6 in the z-direction, the result of Subsection 2.6.3 is used.

$$\boldsymbol{F}_{z6} =$$

$$= i_6 \frac{L\lambda\beta p}{\pi\gamma_1} B_{Bx1}(z_1) \sin(\frac{\pi v}{L})(1-e^{-\gamma_1 d})\{\sin[\frac{2\pi}{L}(-x_6 - \frac{v}{2})] - \sin[\frac{2\pi}{L}(-x_6 + q + \frac{v}{2})]\}\boldsymbol{i}_z$$

$$= -2i_6 \frac{L\lambda\beta p}{\pi\gamma_1} B_{Bx1}(z_1) \sin(\frac{\pi v}{L})(1-e^{-\gamma_1 d}) \sin[\frac{2\pi}{L}(x_6 + \frac{v}{2})]\boldsymbol{i}_z$$

$$= 2i_6 b_{z6} \boldsymbol{i}_z \tag{3.2.26}$$

$$b_{z6} = -\frac{L\lambda\beta p}{\pi\gamma_1} B_{Bx1}(z_1) \sin(\frac{\pi v}{L})(1-e^{-\gamma_1 d}) \sin[\frac{2\pi}{L}(x_6 + \frac{v}{2})] \tag{3.2.27}$$

For the coil 5, with reference to Figure 3-6, x_6 in the case of coil 6 is replaced by (x_6+5L/4), yielding

$$\boldsymbol{F}_{z5} = -2i_5 \frac{L\lambda\beta p}{\pi\gamma_1} B_{Bx1}(z_1) \sin(\frac{\pi v}{L})(1-e^{-\gamma_1 d}) \sin[\frac{2\pi}{L}(x_6 + \frac{5L}{4} + \frac{v}{2})]\boldsymbol{i}_z$$

$$= -2i_5 \frac{L\lambda\beta p}{\pi\gamma_1} B_{Bx1}(z_1) \sin(\frac{\pi v}{L})(1-e^{-\gamma_1 d}) \cos[\frac{2\pi}{L}(x_6 + \frac{v}{2})]\boldsymbol{i}_z$$

$$= 2i_5 b_{z5} \boldsymbol{i}_z , \tag{3.2.28}$$

$$b_{z5} = -\frac{L\lambda\beta p}{\pi\gamma_1} B_{Bx1}(z_1) \sin(\frac{\pi v}{L})(1-e^{-\gamma_1 d}) \cos[\frac{2\pi}{L}(x_6 + \frac{v}{2})] . \tag{3.2.29}$$

The total force acting on the platen in the z-direction is

$$\boldsymbol{F}_z = 2(i_1 b_{z1} + i_2 b_{z2} + i_3 b_{z3} + i_4 b_{z4} + i_5 b_{z5} + i_6 b_{z6}) . \tag{3.2.30}$$

3.2.5 The force-current relation for the 6-coil moving platen

Based on the derivations made from Subsections 3.2.1 to 3.2.3, we figure out the current-force relation for the 6-coil moving platen.

$$\boldsymbol{F} = [F_x \; F_y \; T_z]^{\mathrm{T}} \tag{3.2.31}$$

$$\boldsymbol{i} = [i_1 \; i_2 \; i_3 \; i_4 \; i_5 \; i_6]^{\mathrm{T}} \tag{3.2.32}$$

$$\boldsymbol{F} = \boldsymbol{A}\boldsymbol{i} \tag{3.2.33}$$

$$\boldsymbol{A} = \begin{bmatrix} 0 & 0 & 0 & 0 & 2b_{x5} & 2b_{x6} \\ 2b_{y1} & 2b_{y2} & 2b_{y2} & 2b_{y1} & 0 & 0 \\ -3b_{y1}L/2 & -3b_{y2}L/2 & 3b_{y2}L/2 & 3b_{y1}L/2 & -2b_{x5}c_{56} & -2b_{x6}c_{56} \end{bmatrix} \tag{3.2.34}$$

According to (3.2.2), (3.2.4), (3.2.7), (3.2.9), and (3.2.12), it is recalled that

$$b_{x5} = \frac{L\lambda\beta p}{\pi\gamma_1} B_{Bz1}(z_1) \sin(\frac{\pi v}{L})(1 - e^{-\gamma_1 d}) \sin[\frac{2\pi}{L}(x_6 + \frac{v}{2})], \tag{3.2.35}$$

$$b_{x6} = -\frac{L\lambda\beta p}{\pi\gamma_1} B_{Bz1}(z_1) \sin(\frac{\pi v}{L})(1 - e^{-\gamma_1 d}) \cos[\frac{2\pi}{L}(x_6 + \frac{v}{2})], \tag{3.2.36}$$

$$b_{y1} = b_{y4} = -\frac{L\lambda\beta p}{\pi\gamma_1} B_{Az1}(z_1) \sin(\frac{\pi v}{L})(1 - e^{-\gamma_1 d}) \cos[\frac{2\pi}{L}(y_1 - \frac{v}{2})], \tag{3.2.37}$$

$$b_{y2} = b_{y3} = \frac{L\lambda\beta p}{\pi\gamma_1} B_{Az1}(z_1) \sin(\frac{\pi v}{L})(1 - e^{-\gamma_1 d}) \sin[\frac{2\pi}{L}(y_1 - \frac{v}{2})] . \tag{3.2.38}$$

CHAPTER IV

MECHANICAL DESIGN AND ASSEMBLY

4.1 Mechanical design

Mechanical design of the moving platen is implemented for a light-mass, compact-size and single-part platen without relatively large extra parts for sensor mounts and air bearing supports. The total mass of the moving platen is expected to be below 0.8 kg. The mass of the six coils is 0.258 kg. Therefore, excluding the mass of the small sensor circuits and the electrical connectors, the mass of the frame of the platen should be less than 0.4 kg. Delrin was chosen as the material of the frame of the moving platen because of its three advantages. These are high tensile strength and high hardness, light mass density, and easy machinability. The following are properties of Delrin [14]:

- Mass density: 1.54 g/cm^3
- Tensile strength: 10000 psi
- Hardness: Rockwell R 120

Due to the electromagnetic design of the positioner and the arrangement of the coils on the moving platen discussed in Subsection 3.1, all the coils are placed so that their sides are parallel to the magnet matrix surface. The force-current relation is as simple as what was derived in Subsection 3.2 if the air gaps between the bottom surfaces of the coils and the top surface of the magnet matrix are the same. The electromagnetic forces generated by the coils are stronger if the air gap is smaller. For these reasons, the frame of the moving platen is designed as a plate having two parallel surfaces with the

coils attached in one side of the plate. The coils need to be clamped at their sides with the clamping forces being in the directions parallel to the base surface of the frame. When the moving platen are fully assembled and placed above the top surface of the magnet surface, it is required that there is no coil mounting part being placed underneath the bottom surfaces of the coils so that the coils can be as close to the magnet surface as possible. Six rectangular holes with curved corners are designed. They are formed by milling through the frame body. Each hole fits a coil, which has the coil size shown in Figure 3-3. The coils are clamped in the frame by screwing bolts from outside through the threaded holes in the frame body. SolidWorks[1] was used as the software tool to design the frame of the moving platen. Figure 4-1 shows an isometric view of a 3-D drawing of the frame without threaded holes to clamp the coils.

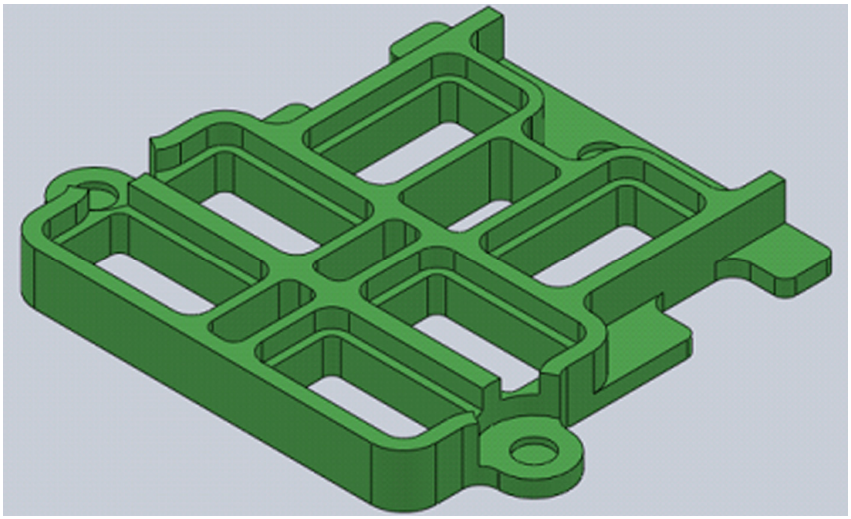

Figure 4-1: An isometric-view drawing of the frame of the single-part platen.

[1] SolidWorks Corporation, 300 Baker Avenue, Concord, MA 01742

In order to levitate the moving platen against gravity, three aerostatic bearings FP-C-010 manufactured by Nelson Air Corporation[2] are used. Figure 4-2 is a drawing including the top view, side view and dimensions of a FP-C-010 aerostatic bearing. The following are its specifications [15]:

- Load Capacity: 88 N
- Air pressure supply: 20 to 80 psi
- Stiffness: 17500 N/mm
- Air inlet size: M3 × 0.5 mm
- Material: Hardcoat Aluminum

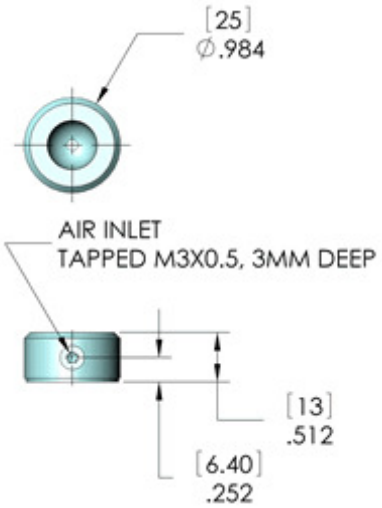

Figure 4-2: A drawing of the FP-C-010 aerostatic bearing,
the length unit is mm in the brackets and is inch outside the brackets [15].

[2] Nelson Air Corp., 559 Route 13 South, Milford, NH 03055

For the mechanical joints between the frame of the platen and the air bearings, three plastic balls made of Delrin with the diameter of 0.498 inch are used. In order to avoid using extra parts for air bearing mounts, the platen's frame is designed to have three blind holes with the depth of 0.9 inch and the plastic balls are rubbed to have the hemisphere shape. Figure 4-3 shows a drawing of a plastic ball after being rubbed for a flat surface. The hemisphere-shape plastic balls are fitted directly into the frame's blind holes so that the flat surface of a ball and the bottom surface of a blind hole are in contact. No screw or adjustment is required. Figure 4-4 illustrates the assembly of the platen's frame, a plastic ball, and an air bearing.

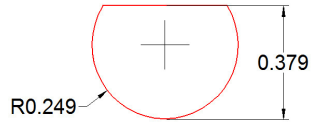

Figure 4-3: A drawing of a plastic ball with a flat surface after being rubbed. (unit: inch)

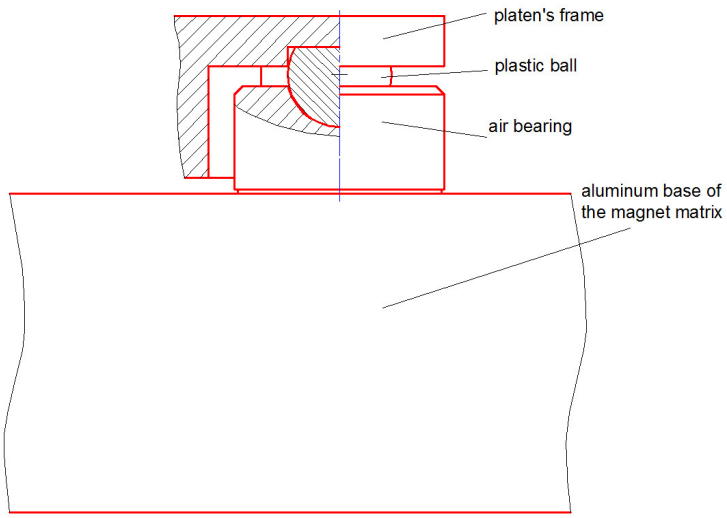

Figure 4-4: Assembly of the platen's frame, a plastic ball, and an air bearing.

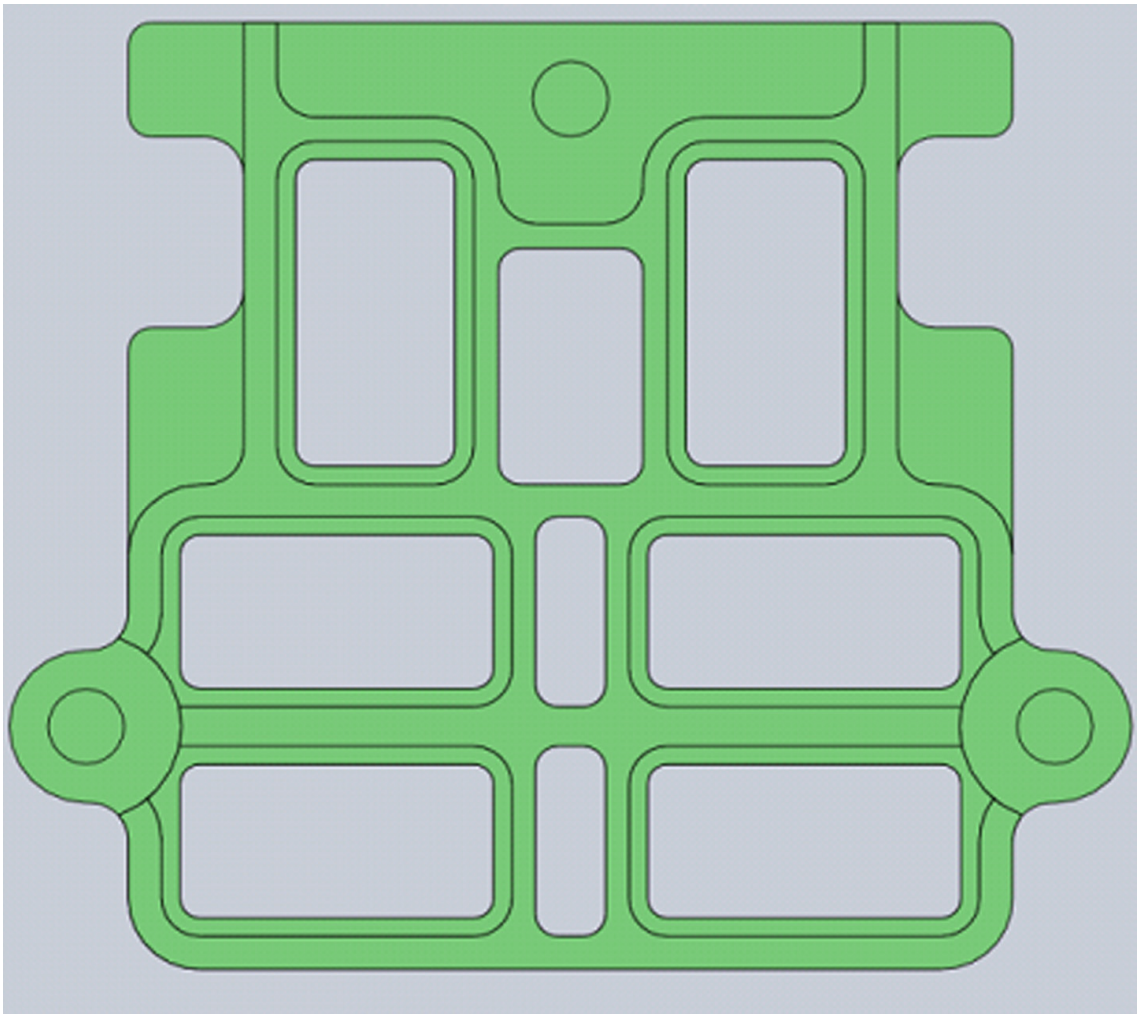

Figure 4-5: A bottom view of the 3-D drawing of the platen's frame.

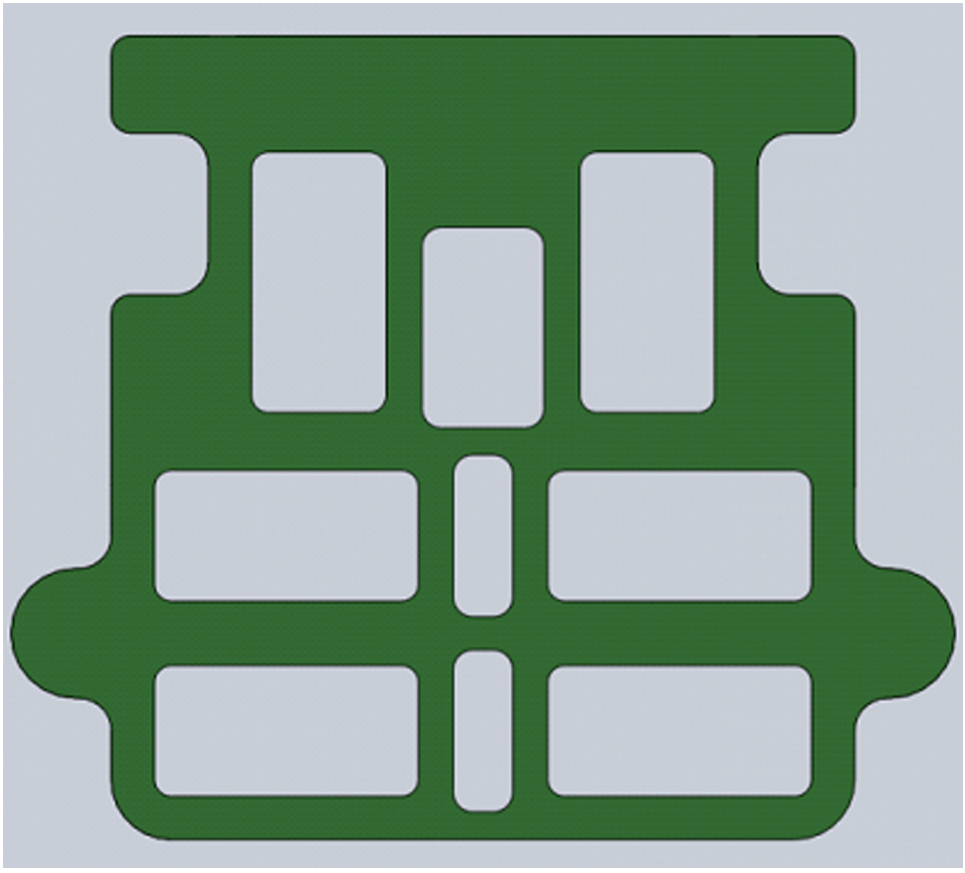

Figure 4-6: A top view of the 3-D drawing of the platen's frame.

Figures 4-5 and 4-6 show a bottom view and a top view of the platen's frame, respectively. The frame of the moving platen was designed so that it can be machined by a 2.5-axis CNC milling machine in a single-tool process with the tool diameter of 0.235 inch (5.97 mm). The top flat surface of the frame in Figure 4-2 is the reference surface for the machining process. All other surfaces of the frame are parallel or perpendicular to the reference surface. All the curve radii in the frame are greater than the radius of the milling tool to allow a single-tool cutting process. Figure 4-7 is a 2-D drawing of the frame with dimensions in detail.

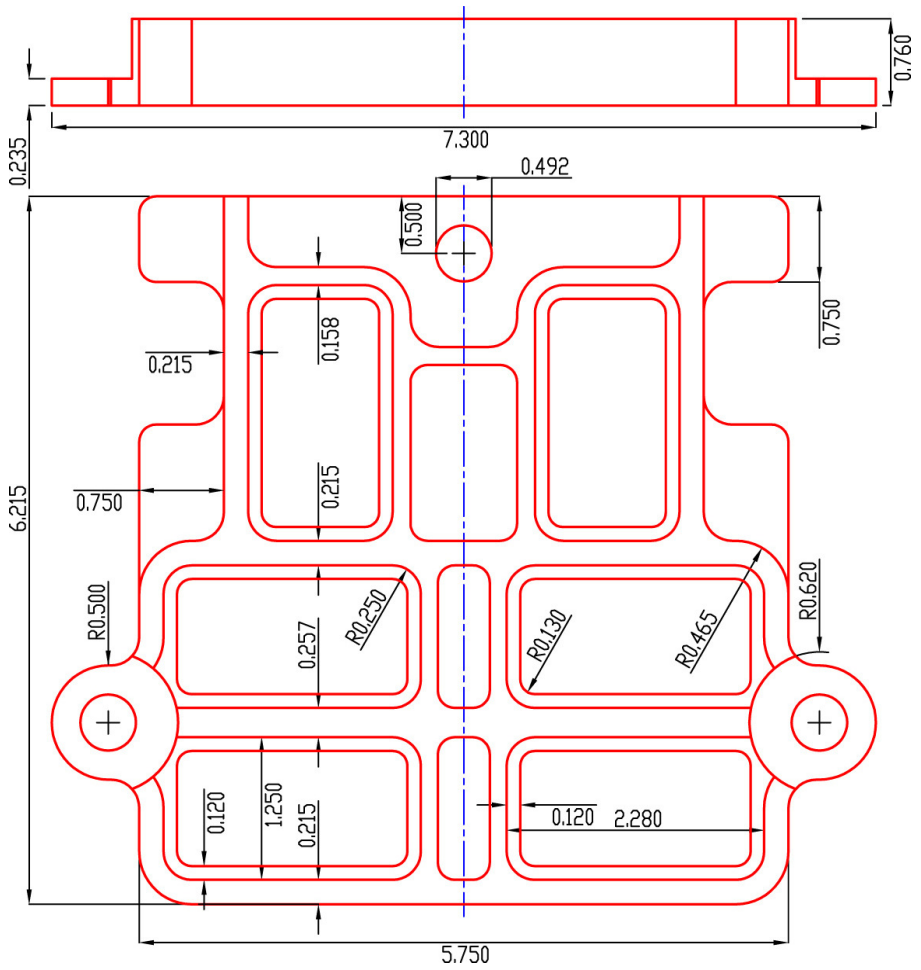

Figure 4-7: A 2-D drawing with the bottom view and side view of the frame. (unit: inch)

The SolidWorks drawing file as shown in Figures 4-1, 4-5, and 4-6 was imported into MasterCam[3] to generate a CNC cutting program. The frame of the moving platen was cut by a 3-axis CNC milling machine manufactured by Hass Automation[4] with positioning resolution of 1 μm.

---

[3] CNC Software Inc., 671 Old Post Road, Tolland, CT 06084

[4] Hass Automation Inc., 2800 Sturgis Rd., Oxnard, CA 93030

4.2 Assembly of the moving platen

After the cutting process to form the frame of the moving platen was completed, six threaded holes were created in the body of the frame in order to clamp the six coils in their spaces. The thread size is M3 × 0.5. Figure 4-8 shows an isometric-view 3-D drawing of the frame with the holes. Figure 4-9 shows the assembly drawing of the frame and six coils in place.

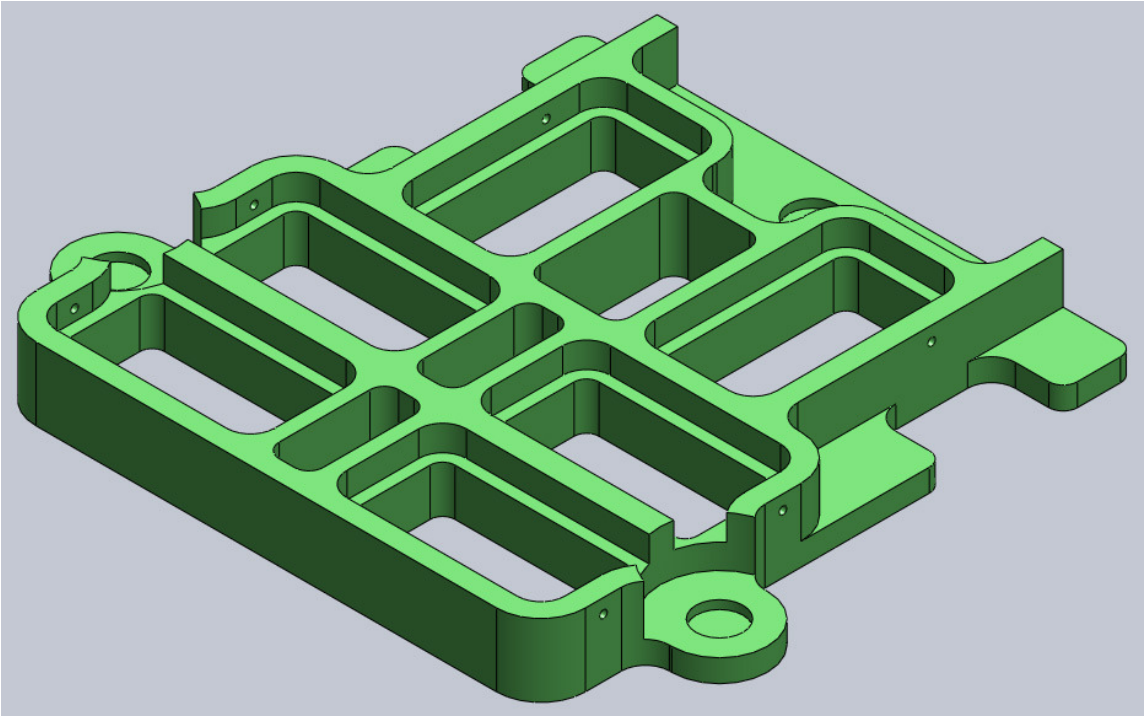

Figure 4-8: A 3-D drawing of the frame with the holes.

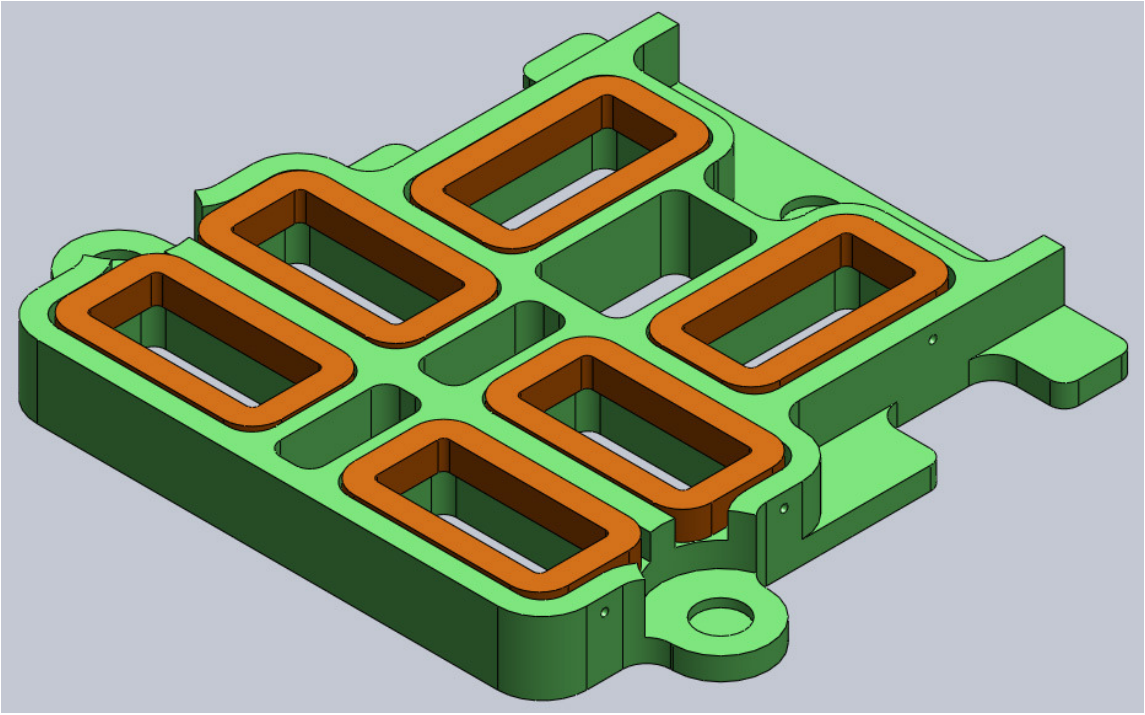

Figure 4-9: A 3-D assembly drawing of the platen's frame with six coils.

Figure 4-10 shows one of the three air bearings supporting the platen. The white plastic ball plays the role of the mechanical joint between the platen's frame and the air bearing. Figure 4-11 is a bottom-view picture of the platen with all the coils attached. An air gap of 1.5 mm is maintained between the bottom surfaces of the coils and the aluminum surface on top of the magnet matrix. The distance between the bottom surfaces of the coils and the surface of the magnet matrix is 3 mm. The z_1 in all the force calculation in Subsection 3.2 is 0.003 m.

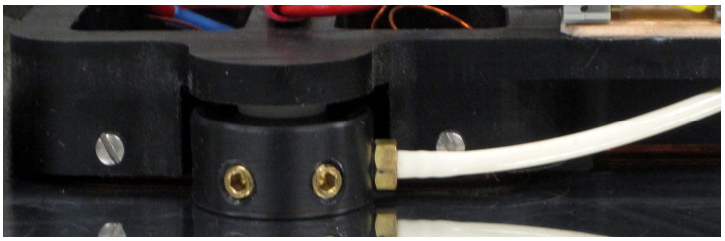

Figure 4-10: A picture of a corner of the moving platen with an air bearing.

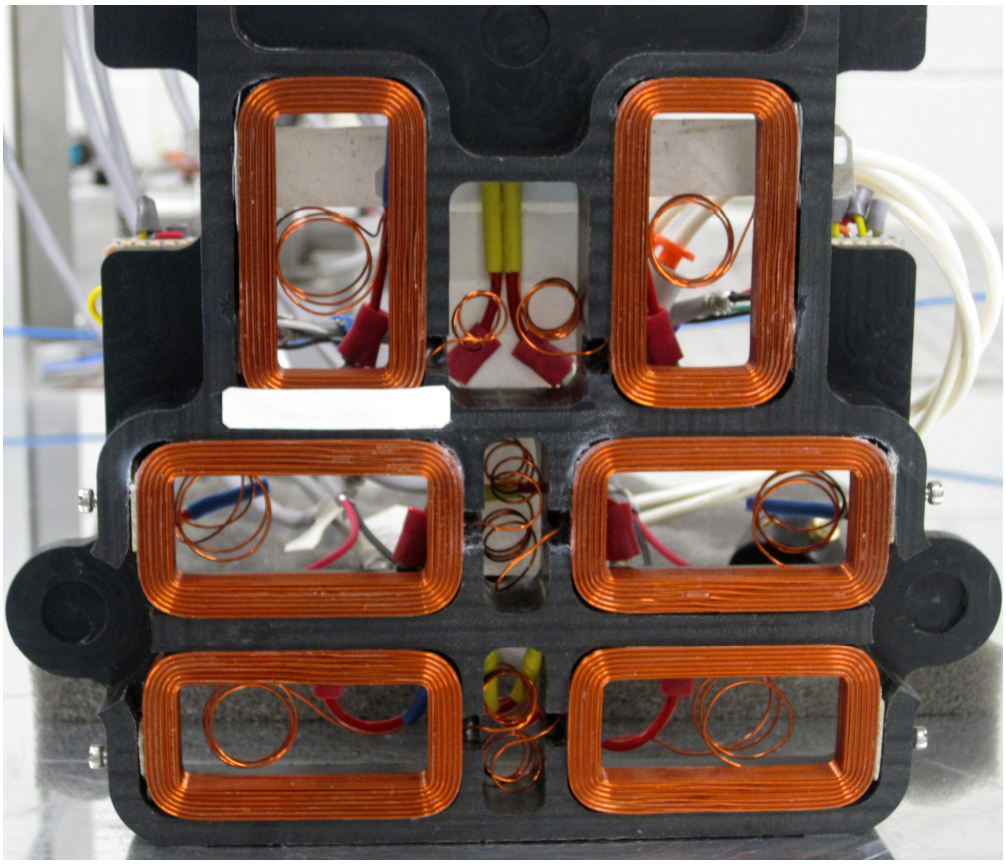

Figure 4-11: A bottom-view photo of the platen with 6 coils attached.

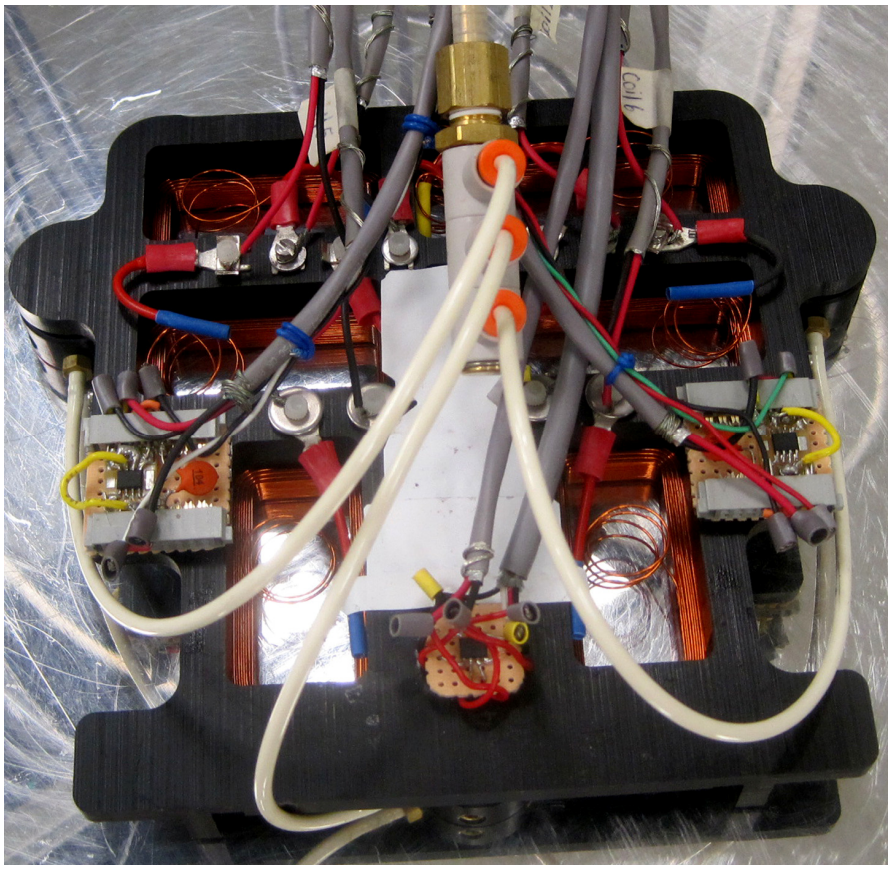

Figure 4-12: The platen with all components assembled.

Figure 4-12 is a photograph of the platen with all its components attached. As seen from this, three Hall-effect sensors are soldered in the three boards which are glued directly to the top surface of the platen's frame. The distance from the center points of the sensors to the aluminum surface on top of the magnet matrix is 27.7 mm. A diagram showing the exact locations of the sensors in the platen is given in Subsection 5.3.

The total mass of the moving platen, including the frame, the six coils, the three sensors and connectors is 0.64 kg. The moments of inertia taken at the center of mass with respect to principal axes are:

$I_{xx} = 0.0010$ $I_{xy} = 0.0000$ $I_{xz} = 0.0000$

$I_{yx} = 0.0000$ $I_{yy} = 0.0019$ $I_{yz} = 0.0000$

$I_{zx} = 0.0000$ $I_{zy} = 0.0000$ $I_{zz} = 0.0010$

Unit: kg m^2.

The advantages of the single-part platen designed in this thesis project are summarized as following:

- Light mass, 0.64 kg
- Low center of mass from the top surface of the magnet matrix, 0.4 inch
- Compact size, allowing large motion ranges along *x* and *y*.
- Being symmetric in the *y*-direction.

CHAPTER V

INSTRUMENTATION

5.1 Overall instrumentation diagram

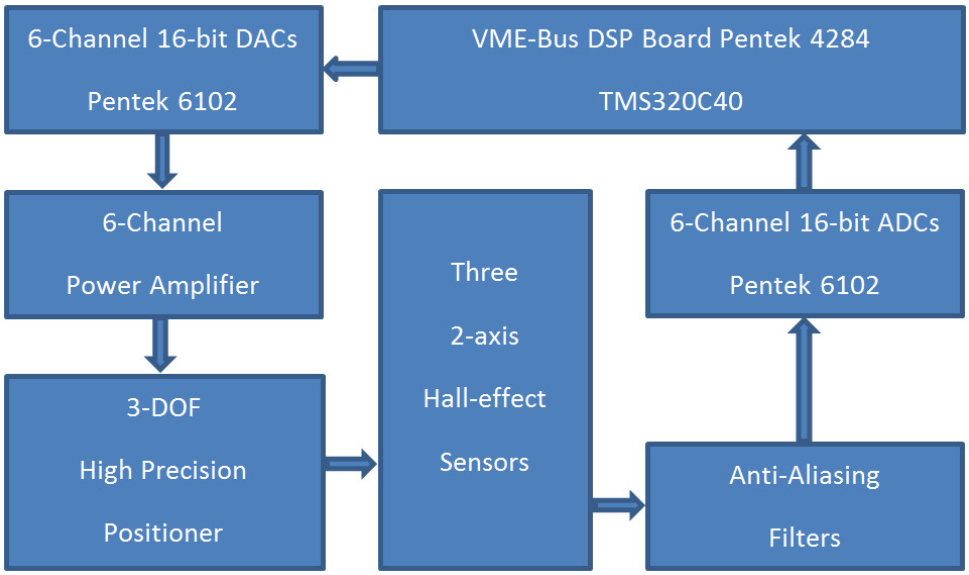

Figure 5-1: Overall instrumentation diagram.

Figure 5-1 is the overall instrumentation diagram of the 3-DOF high precision positioning system. It illustrates the signal flows between the hardware components of the system. The target DSP (digital-signal-processing) board is Pentek[5] 4284 with the central processing unit TMS320C40 from Texas Instruments[6]. Pentek 6102 with 8 ADC

---

[5] Pentek, Inc. One Park Way, Upper Saddle River, NJ 07458

[6] Texas Instruments Inc., 12500 TI Boulevard, Dallas, TX 75243

(analog-to-digital-conversion) channels and 8 DAC (digital-to-analog-conversion) channels is used as the data I/O board for the DSP board 4284. The output signals from the Hall-effect sensors attached to the moving platen are the inputs to the anti-aliasing filters. The outputs of the anti-aliasing filters are the inputs to the ADC channels. The central processing unit in the DSP board sends the control signals to the power amplifier through the DAC channels in Pentek 6102. The outputs of the power amplifier are the currents flowing in the six coils of the positioner.

5.2 DSP board Pentek 4284 and data acquisition board Pentek 6102

The DSP board Pentek 4284 has a 2-Megabyte dual-port shared RAM (random-access-memory) and 128-kB flash EPROM (erasable-programmable-read-only-memory). The peak processing power of Pentek 4284 is 50 million-floating-point operations per second [16]. It can work on a 32-bit-address VME-bus (VERSAmodule Eurocard) system as a master or a slave, allowing real-time data communication with a VME computer and with external sources via the data I/O board Pentek 6102.

The data I/O board, Pentek 6102 is used with the DSP board 4284 on the same VME-bus, allowing ADC and DAC. Figure 5-2 shows pictures of the DSP board, Pentek 4284 and the Data I/O board, Pentek 6102. The specifications of Pentek 6102 are listed below [16]:

- 8 A/D channels and 8 D/A channels, both with 16-bit resolution
- Differential inputs
- Maximum sampling rate: 250 kHz

- Input voltage range: −5 V to 5 V
- First-in-first-out buffering for each A/D and D/A channel.

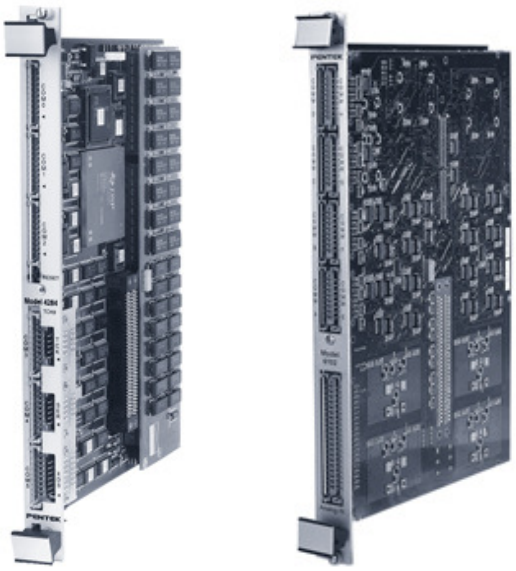

(a) (b)

Figure 5-2: A picture of (a) the DSP board Pentek 4284 and (b) the data I/O board Pentek 6102 [16].

A VME computer running on Windows 2000 with Texas Instrument Code Composer installed is used to write and compile programs in C code. After compiling, the executable file is loaded from the VME computer to the target DSP board 4284 and ready to run.

5.3 Hall-effect sensors

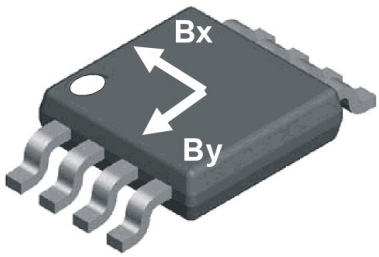

Figure 5-3: A drawing of 2SA-10 with its sensitive sensing directions [17].

Three 2-axis Hall-effect sensors 2SA-10 made by Sentron AG[7] are used to measure the magnetic flux density above the superimposed Halbach magnet matrix. Each Hall-effect sensor can measure two orthogonal magnetic flux density components at the center point of the sensor [17]. Figure 5-3 is a drawing of the Hall-effect sensor 2SA-10 and its two sensitive sensing directions. Following are the specifications of the sensor [17]:

- Sensing range: –40 mT to 40 mT
- Magnetic sensitivity: 50 V/T (supply voltage 5.00 V)
- Bandwidth: DC to 18 kHz
- Magnetic input conditions: > 1000 mT, devices saturates, but not damaged.

Figure 5-4 is the diagram of connections for reliable operation of 2SA-10. Figure 5-5 shows the positions of the sensors in the moving platen. The position of the moving

[7] Sentron AG, Baarerstrasse 73 CH-6300 Zug, Switzerland

platen in the base coordinate system fixed to the magnet matrix is determined by the field solution of the magnet matrix and the magnetic flux densities sensed by the Hall-effect sensors. Beyond the sensitive intervals as noted in Figure 5-6, the sensing noise is relatively large and the magnetic flux density may exceed the sensing range of the sensors. A collaboration working approach was used in [10] to take advantages of linearity and low sensing noise in the sensitive intervals.

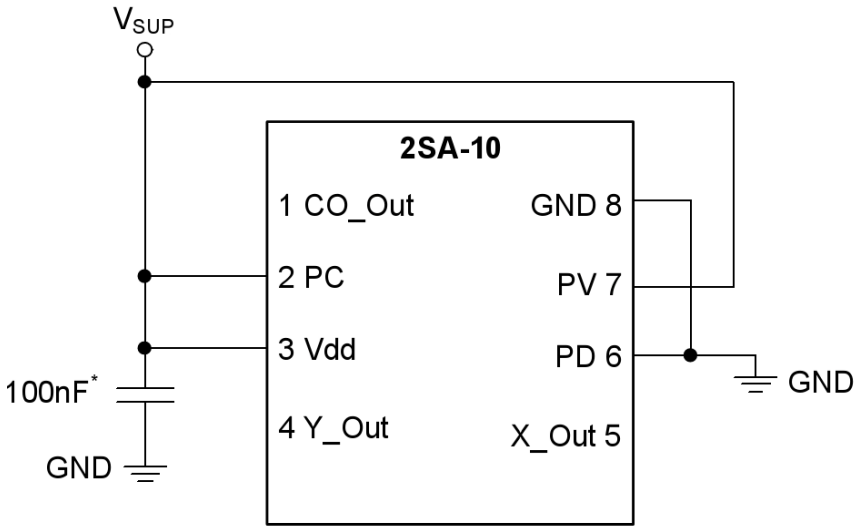

Figure 5-4: Connections diagram for the Hall-effect sensor 2SA-10 [17].

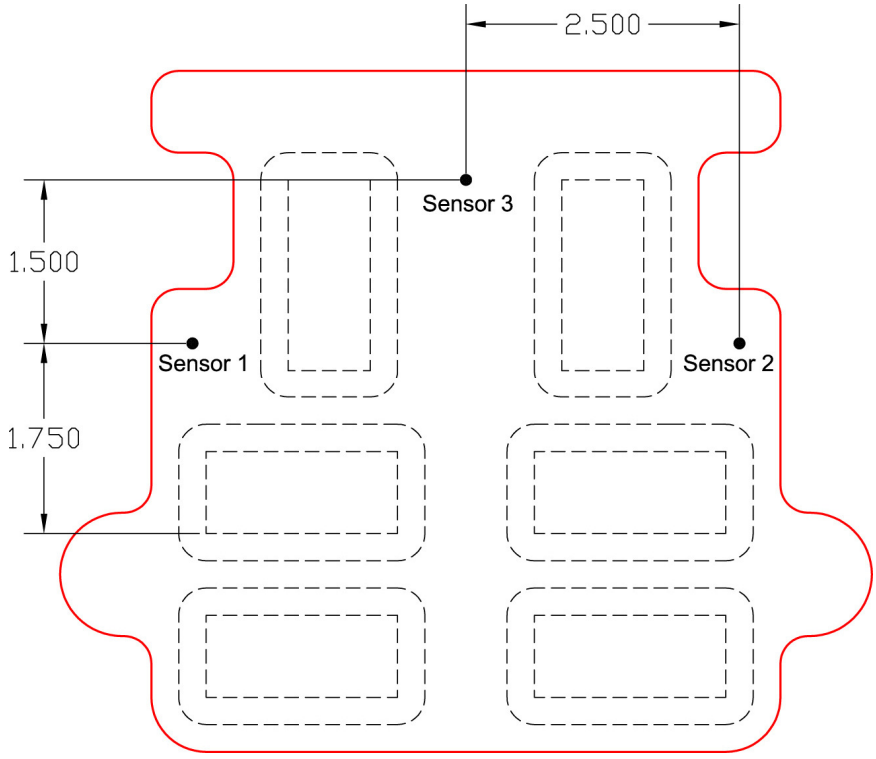

Figure 5-5: Positions of the sensors in the moving platen, unit: inch.

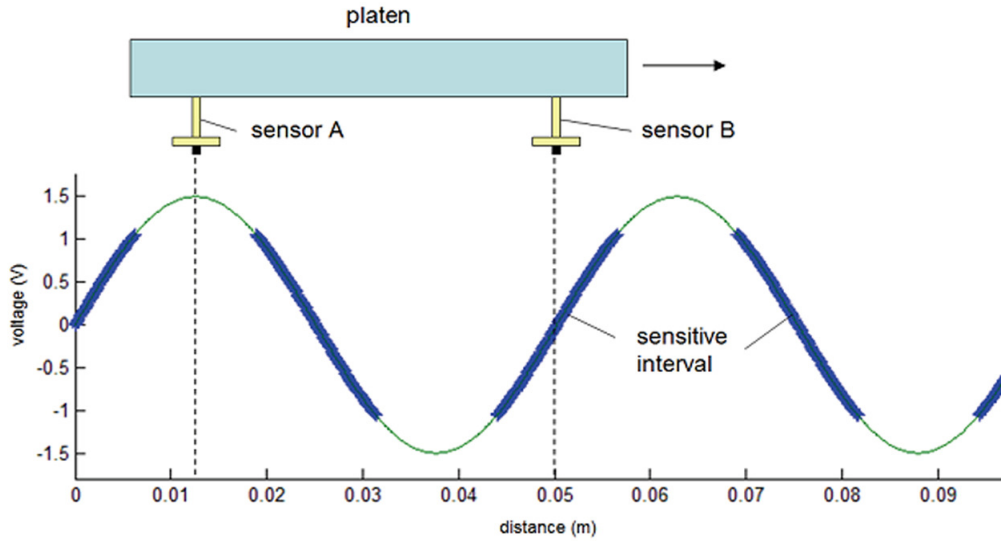

Figure 5-6: Collaboration of two sensors [10].

5.4 Power amplifier circuits

Figure 5-7 shows the diagram of a power amplifier circuit [1] used in this thesis project. Six power amplifier units are used for six coils in the moving platen. The input voltage of a power amplifier circuit is commanded from the DSP board 4284 via a D/A channel of the data acquisition board 6102. The output is the current flowing in the coil, which has the resistance R_a and the inductance L_a. Following are values of the electronic components in a power amplifier circuit:

- $R_1 = R_2 = R_4 = R_5 = R_8 = R_9 = 10$ kΩ
- $C_1 = C_2 = C_3 = 10$ nF
- $R_a = 1.98$ Ω
- $L_a = 1.28$ mH
- $R_6 = 27.4$ kΩ, $R_7 = 5$ kΩ

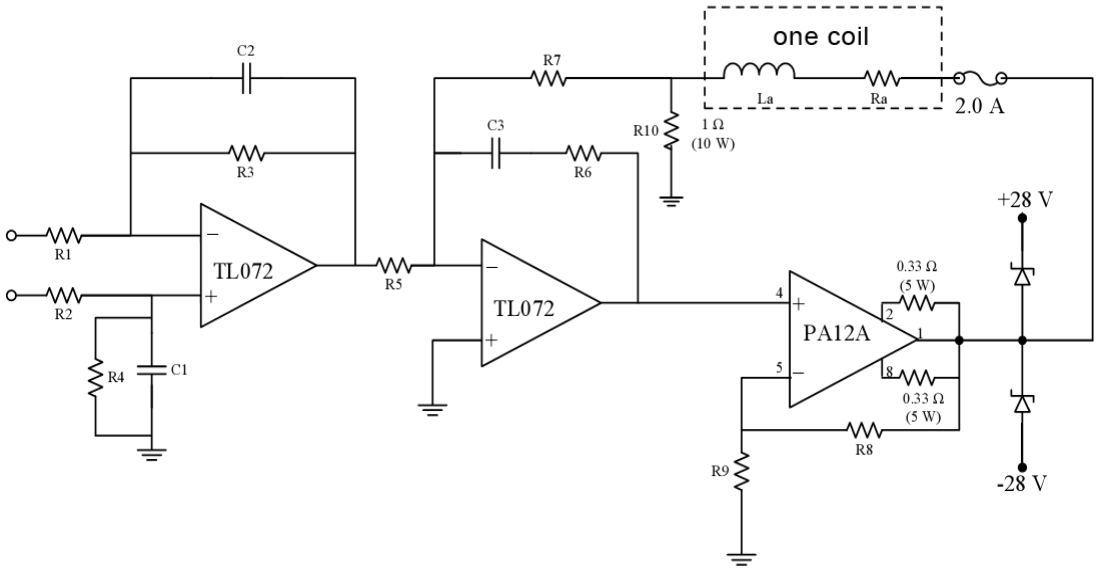

Figure 5-7: Circuit diagram of a power amplifier unit [1].

The power OP Amps PA12A manufactured APEX[8] meet the requirements of excellent linearity, high output current, and high slew rate [17]. They were used for the power amplifier circuits in the previous works [1], [6] and [10]. Some of PA12A's specifications [18] are listed below and the external connections are given in Figure 5-8:

- Supply range: ±10 V to ±50 V.
- Output current: Up to ±15 A peak.
- Settling time to 0.1% in a 2V step at 25°C: 2 µs.
- Slew rate at 25°C: 4 V / µs.
- Maximum power dissipation: 125 W.

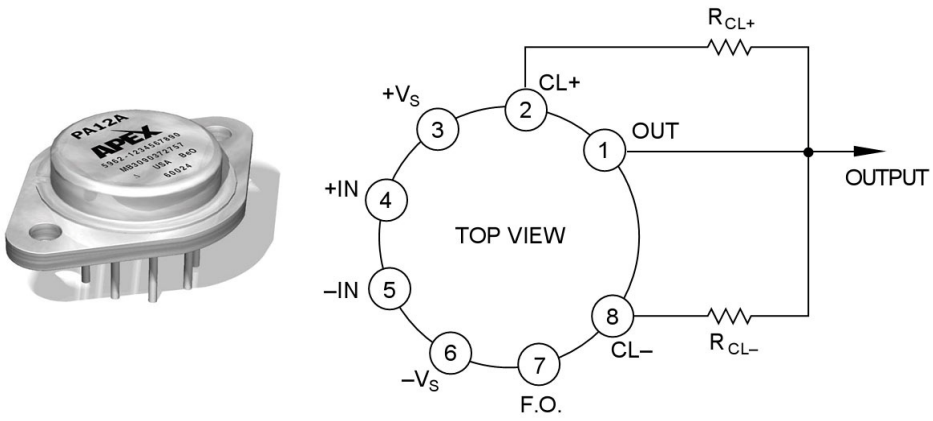

Figure 5-8: An Apex PA12A and the external connections required [18].

[8] Apex Microtechnology Corp., 5980 N. Shannon Road, Tuscon, Arizona 85741

The transfer function for a power amplifier unit is derived and obtained as following:

$$H(s)=\frac{I_{coil}(s)}{V_{in}(s)}=$$

$$=\frac{R_3R_7(R_8+R_9)(R_6C_3s+1)}{R_1R_5(R_3C_2s+1)[R_{10}(R_8+R_9)(R_6C_3s+1)\ +\ R_7R_9C_3s(R_{10}+R_a+L_as)]}$$

Figure 5-9 is the Bode plot of the frequency response of a power amplifier circuit. The power amplifier bandwidth is 6.893 kHz; the power amplifier gain is 0.506. Within the control bandwidth of 100 Hz, the phase lag that the power amplifier circuit adds into the system is less than 1°. The dynamics of the power amplifier can be ignored.

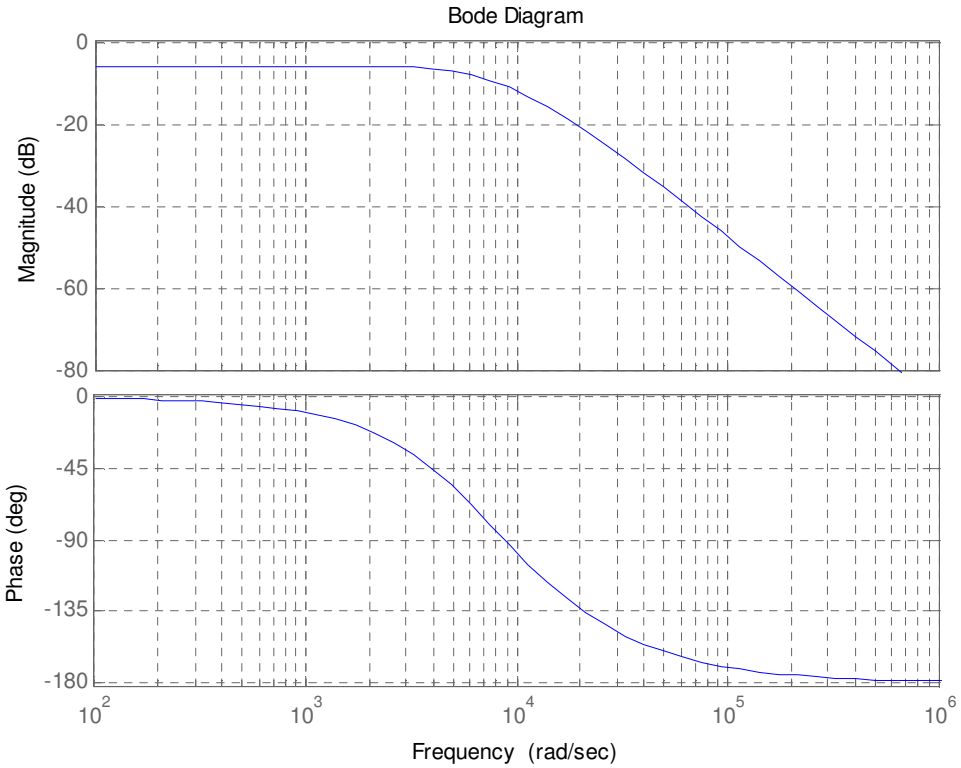

Figure 5-9: Frequency response of the power amplifier.

5.5 Anti-aliasing filter

The anti-aliasing filter used in this project is a first-order low-pass filter as shown in Figure 5-10. Based on the system's sampling frequency of 1 kHz and the fast Fourier transform analysis of the signal sensed from the Hall-effect sensors without an anti-aliasing filter, a cut-off frequency in the range of 200 Hz to 250 Hz is desirable. Therefore, the resistance and capacitance of the filter circuit were chosen as R = 7.326 kΩ and C = 0.1 μF, yielding a cut-off frequency of 217 Hz.

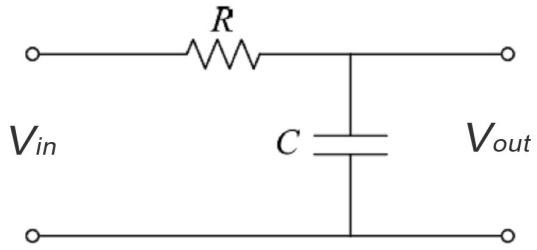

Figure 5-10: Anti-aliasing filter.

CHAPTER VI

DYNAMICS ANALYSIS AND CONTROL OF THE POSITIONER

6.1 Dynamics analysis of the moving platen

This section describes the dynamics analysis of the moving platen, using the Newtonian approach and the force-current relation derived in Subsection 3.2. Following are the definitions and physical quantities used in this subsection:

- *xyz* is an inertia Cartesian coordinate system fixed to the superimposed Halbach magnet matrix. Where *xy* is the plane contains the strong-side surface of the magnet matrix.
- *x'y'z'* is a Cartesian coordinate system with the origin at the platen's center of mass, *x'*, *y'*, and *z'* are parallel to *x*, *y*, and *z*, respectively.
- m is the mass of the platen, $m = 0.64$ kg.
- I_z is the moment of inertia of the platen about the *z'*-axis, $I_z = 0.001$ kg m^2.
- F_x and F_y are the resultant electromagnetic forces acting on the platen in the *x*-direction, and the *y*-direction, respectively.
- T_z is the torque acting on the moving platen about the *z'*-axis due to the electromagnetic forces acting on the coils.
- φ is the rotation angle of the platen about the *z'*-axis.

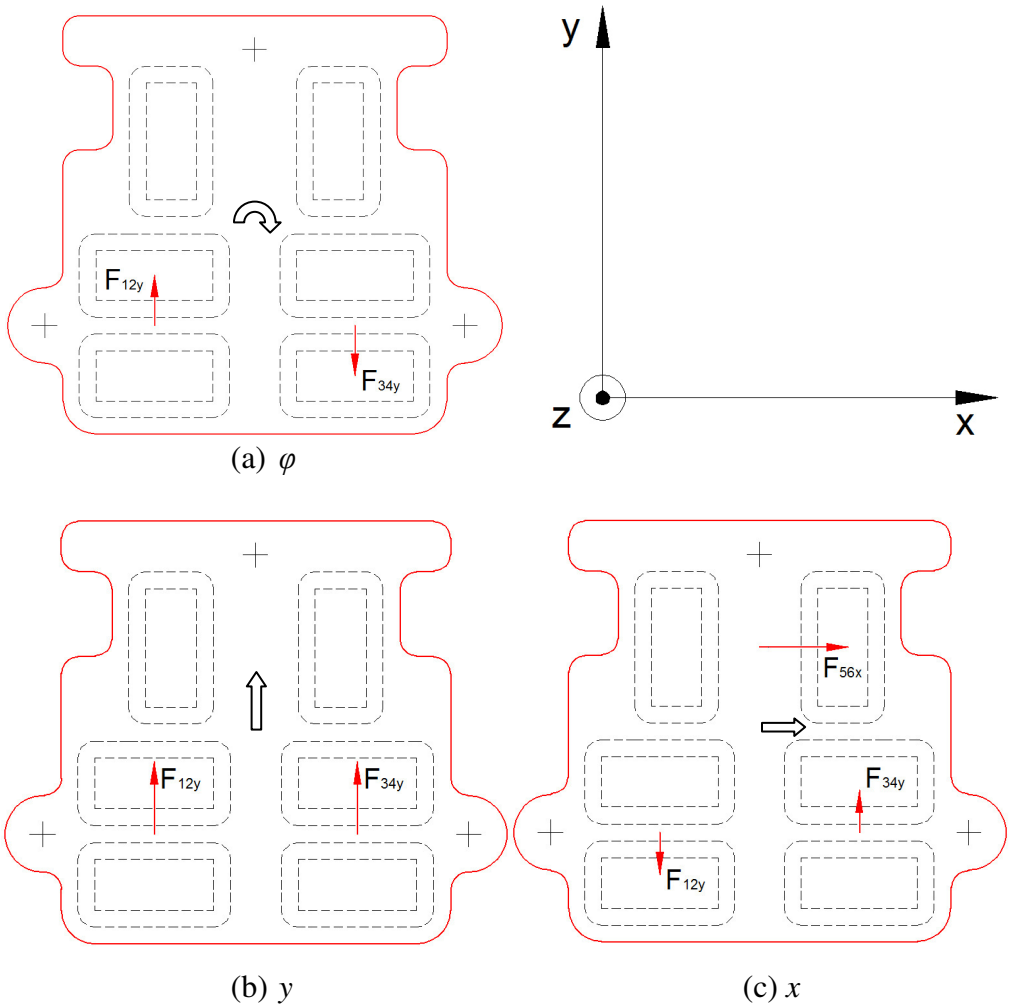

(a) φ (b) y (c) x

Figure 6-1: Illustration of 3-DOF motion generation.

In considering force allocation for mechanical dynamics of the moving platen, the six coils in the moving platen can be divided into three sets of coils with two coils per set. Each of the two set of coils 1 and 2 and the set of coils 3 and 4 can only generate two independent force components in the y-direction and in the z-direction. Coils 5 and 6 can only generate two independent force components in the x-direction and in the z-direction. Figure 6-1 shows the diagrams of the force allocation to generate all 3-DOF

motions in the *xy* plane.

According to the outcome of Subsection 3.2.4, the resultant force acting on the two coils 1 and 2 in the *z*-direction is

$$\boldsymbol{F}_{z1} + \boldsymbol{F}_{z2} =$$

$$= 2i_1 \frac{L\lambda\beta p}{\pi\gamma_1} B_{Ay1}(z_1)\sin(\frac{\pi v}{L})(1-e^{-\gamma_1 d})\{\sin[\frac{2\pi}{L}(y_1-\frac{v}{2})]+\cos[\frac{2\pi}{L}(y_1-\frac{v}{2})]\}\boldsymbol{i}_z$$

$$= 2\sqrt{2}i_1 \frac{L\lambda\beta p}{\pi\gamma_1} B_{Ay1}(z_1)\sin(\frac{\pi v}{L})(1-e^{-\gamma_1 d})\sin[\frac{2\pi}{L}(y_1-\frac{v}{2})+\frac{\pi}{4}]\boldsymbol{i}_z . \quad (6.1.1)$$

With the maximum electric currents of 1 A, the maximum force acting on the platen in the *z*-direction generated by coils 1 and 2 is

$$F_{z12\_max} = \left| 2\sqrt{2}i_1 \frac{L\lambda\beta p}{\pi\gamma_1} B_{Ay1}(z_1)\sin(\frac{\pi v}{L})(1-e^{-\gamma_1 d}) \right| = 4.4 \text{ N}. \quad (6.1.2)$$

Similarly, we have the maximum forces acting on the platen in the *z*-direction generated by the set of coils 3 and 4, and the set of coils 5 and 6 are

$$F_{z34\_max} = 4.4 \text{ N}, \quad (6.1.3)$$

$$F_{z56\_max} = 4.4 \text{ N}. \quad (6.1.4)$$

The stiffness of an air bearing is 17000 N/mm [13]. Three air bearing supporting the moving platen have a resultant stiffness of 51000 N/mm. The maximum displacement of the moving platen in the vertical direction is

$$4.4 \times 3 / (51 \times 10^6) = 0.26 \text{ μm}.$$

The maximum rotation angles about the *y*' and *x*' axes are estimated to be, respectively,

$$\theta_{max} = 6.82 \times 10^{-6} \text{ rad},$$

$$\psi_{max} = 7.44 \times 10^{-6} \text{ rad}.$$

Thus, because of the high stiffness of the air bearings and the limited electric currents that can be flowed into the coils, the error vertical displacement and the rotation angles about the horizontal axes of the moving platen can be ignored.

In order to move the platen in the *y*-direction, the set of coils 1 and 2 and the set of coils 3 and 4 generate two resultant forces in the same direction. In order to move the platen in the *x*-direction, coil 5 and coil 6 are energized to yield a resultant force in the *x*-direction, concurrently generating a torque about the *z'*-axis. This torque must be cancelled by two forces with the same magnitude but opposite directions generated by the set of coils 1 and 2 and the set of coils 3 and 4. For the rotation about the *z'*-axis, the resultant force in the horizontal plane generated by the set of coils 5 and 6 must be zero. The set of coils 1 and 2 and the set of coils 3 and 4 generate two resultant forces with the same magnitude but opposite directions.

The detailed derivation of the equations representing the dynamics of the moving platen is given below. From the result of the Subsection 3.2, the current-force relation for planar motions in the *xy* plane of the moving platen is:

$$\boldsymbol{f} = \boldsymbol{A}\boldsymbol{i}$$

$\boldsymbol{f} = [F_x \; F_y \; T_z]^{\mathrm{T}}$ is the column vector of the forces acting on the moving platen.

$\boldsymbol{i} = [i_1 \; i_2 \; i_3 \; i_4 \; i_5 \; i_6]^{\mathrm{T}}$ is the column vector of the currents flowing in the coils.

$$\boldsymbol{A} = \begin{bmatrix} 0 & 0 & 0 & 0 & 2b_{x5} & 2b_{x6} \\ 2b_{y1} & 2b_{y2} & 2b_{y2} & 2b_{y1} & 0 & 0 \\ -3b_{y1}L/2 & -3b_{y2}L/2 & 3b_{y2}L/2 & 3b_{y1}L/2 & -2b_{x5}c_{56} & -2b_{x6}c_{56} \end{bmatrix}$$

According to Newtonian dynamics, the equations of motion of the moving platen in the horizontal directions with negligible friction are

$$\begin{cases} m\ddot{x} = F_x \\ m\ddot{y} = F_y \\ m\ddot{\varphi} = T_z \end{cases} \tag{6.1.5}$$

The dynamics of the moving platen can be described as following:

$$m\ddot{x} = 2b_{x5}i_5 + 2b_{x6}i_6\,, \tag{6.1.6}$$

$$m\ddot{y} = 2b_{y1}(i_1 + i_4) + 2b_{y2}(i_2 + i_3)\,, \tag{6.1.7}$$

$$I_z\ddot{\varphi} = -3b_{y1}(i_1 - i_4)L/2 - 3b_{y2}(i_2 - i_3)L/2 - 2c_{56}(b_{x5}i_5 + b_{x6}i_6)\,, \tag{6.1.8}$$

where, according to (3.2.35), (3.2.36), (3.2.37), and (3.2.38),

$$b_{x5} = \frac{L\lambda\beta p}{\pi\gamma_1} B_{Bz1}(z_1)\sin(\frac{\pi v}{L})(1-e^{-\gamma_1 d})\sin[\frac{2\pi}{L}(x_6 + \frac{v}{2})],$$

$$b_{x6} = -\frac{L\lambda\beta p}{\pi\gamma_1} B_{Bz1}(z_1)\sin(\frac{\pi v}{L})(1-e^{-\gamma_1 d})\cos[\frac{2\pi}{L}(x_6 + \frac{v}{2})],$$

$$b_{y1} = b_{y4} = -\frac{L\lambda\beta p}{\pi\gamma_1} B_{Az1}(z_1)\sin(\frac{\pi v}{L})(1-e^{-\gamma_1 d})\cos[\frac{2\pi}{L}(y_1 - \frac{v}{2})],$$

$$b_{y2} = b_{y3} = \frac{L\lambda\beta p}{\pi\gamma_1} B_{Az1}(z_1)\sin(\frac{\pi v}{L})(1-e^{-\gamma_1 d})\sin[\frac{2\pi}{L}(y_1 - \frac{v}{2})].$$

6.2 Control of the positioner

The nonlinearity of the system is due to the trigonometric terms in the force-current relations derived in Subsection 3.2. The force vector is related to the current vector by a matrix ***A*** which has all non-zero elements depending on *x* or *y* sinusoidally. This relation is position-dependent. For path-following motions or step motions with large step sizes, the approach of linearization of the system about a number of operating

points cannot work. The position-dependent trigonometric terms cannot be linearized at every point in a continuous path in the working space. In this subsection, a discrete PID-like controller is proposed to close the control loop for the moving platen to stabilize its position and to perform motions over the superimposed Halbach magnet matrix. The focuses are step responses in translational motions in x and y, and step responses in rotational motions about the z-axis.

First, we consider the simplest case by the assumption that there is no external force acting on the platen on the horizontal plane. Let $i_1 = i_4$, $i_2 = i_3$ and $i_5 = i_6 = 0$, the electromagnetic forces F_x, F_y, and T_z acting on the platen are reduced to

$$F_x = 0,$$

$$F_y = 4(b_{y1} i_1 + b_{y2} i_2),$$

$$T_z = 0,$$

where $b_{y1} = -\frac{L\lambda\beta p}{\pi\gamma_1} B_{Az1}(z_1) \sin(\frac{\pi v}{L})(1-e^{-\gamma_1 d}) \cos[\frac{2\pi}{L}(y_1 - \frac{v}{2})]$,

$$b_{y2} = \frac{L\lambda\beta p}{\pi\gamma_1} B_{Az1}(z_1) \sin(\frac{\pi v}{L})(1-e^{-\gamma_1 d}) \sin[\frac{2\pi}{L}(y_1 - \frac{v}{2})].$$

For conciseness, we denote

$$b_0 = \frac{L\lambda\beta p}{\pi\gamma_1} B_{Az1}(z_1) \sin(\frac{\pi v}{L})(1-e^{-\gamma_1 d}). \tag{6.2.1}$$

It is reminded that

$$\gamma_1 = 2\pi / L. \tag{6.2.2}$$

As a consequence, we have

$$F_y = -4b_0 \cos[\gamma_1(y_1 - \frac{v}{2})]i_1 + 4b_0 \sin[\gamma_1(y_1 - \frac{v}{2})]i_2 . \quad (6.2.3)$$

The nature of the system is that the force F_y drives the moving platen to find an unique equilibrium position in one pitch of the magnet array at which F_y is minimized. When the currents i_1 and i_2 flowing in the coils 1 and 2 are constant, the relation between the currents i_1, and i_2 and the equilibrium position y_1 is expressed as

$$-\cos[\gamma_1(y_1 - \frac{v}{2})]i_1 + \sin[\gamma_1(y_1 - \frac{v}{2})]i_2 = 0 . \quad (6.2.4)$$

Solving this relation in real-time with inverse trigonometric functions and caution of singularity should be avoided. A controller u, which has the effect on the dynamics of the system given by the following equations, is proposed.

$$\begin{cases} i_1 = I_{12} \sin(\gamma_1 u) \\ i_2 = I_{12} \cos(\gamma_1 u) \end{cases} \quad (6.2.5)$$

I_{12} is a constant current figured out by the force required to drive the moving platen. Apart from avoiding solving (6.2.4) with inverse trigonometric functions, this form of control effort being related to electric currents has two advantages. Firstly, it limits the electric currents flowing in the coils by I_{12}, avoiding overheating the coils and damage to the power amplifier units. Secondly, it creates a linear relation between the control effort u and the position y_1 in steady state as given by (6.2.8).

$$-\cos[\gamma_1(y_1 - \frac{v}{2})]\sin(\gamma_1 u) + \sin[\gamma_1(y_1 - \frac{v}{2})]\cos(\gamma_1 u) = 0 \quad (6.2.6)$$

$$\sin[\gamma_1(y_1 - \frac{v}{2} - u)] = 0 \quad (6.2.7)$$

$$\gamma_1(y_1 - \frac{v}{2} - u) = r\pi \text{ , } r \text{ is an integer} \tag{6.2.8}$$

In this system, instead of using the platen's position for feedback, the magnetic flux densities sensed from the Hall-effect sensors are used. The primary reason is the field solution given by (2.3.30),

$$B_y(x, y, z) = \sum_{k=0}^{+\infty} (-1)^{k+1} 2\mu_0 \frac{\sqrt{2}M_0}{\pi n}(1 - e^{-\gamma_n \Delta}) e^{-\gamma_n z} \sin(\frac{2\pi n}{L} y) \text{ ,}$$

$n = 4k + 1$, k is a non-negative integer.

It is seen that once the magnetic flux density $B_y(x, y, z)$ is known, the position y cannot be figured out precisely by simply taking the inverse of a trigonometric function corresponding to the highest harmonic $n = 1$. Solving the relation for the position y with two harmonics of $n = 1$ and $n = 5$ is not allowed in real-time. In which the entire control routine is expected to be executed in less than 1000 μs. Therefore, in y, the magnetic flux density B_y is chosen as the output representing the position of the moving platen.

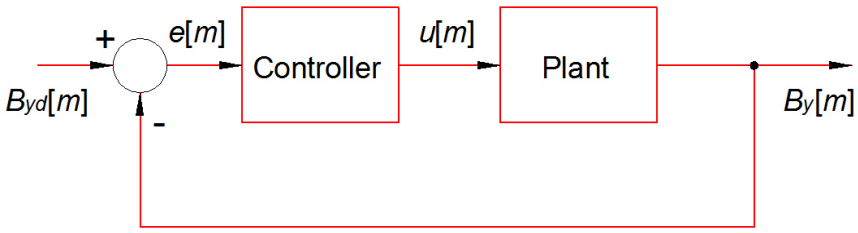

Figure 6-2: The discrete control diagram with B_y being the output.

Figure 6-2 shows a control diagram in which B_y is the output, B_{yd} is the reference. With negligible friction, the plant can be considered a pure mass system. A discrete PID

controller $u[m]$ has the form of

$$u[m] = u_1[m] + u_2[m] + u_3[m], \tag{6.2.9}$$

where

m is the iteration index in the discrete control process,

$$u_1[m] = k_p\, e[m], \tag{6.2.10}$$

$u_1[m]$ is the proportional part in the discrete PID controller,

$$u_2[m] = u_2[m-1] + k_I\, e[m]\, T, \tag{6.2.11}$$

$u_2[m]$ is the integral part in the discrete PID controller, following backward rectangular transform,

T is a sampling period, T = 0.001 s.

$$u_3[m] = k_d\, (e[m] - e[m-1]) / T, \tag{6.2.12}$$

$u_3[m]$ is the derivative part in the discrete PID controller,

$$e[m] = B_{yd}[m] - B_y[m] \tag{6.2.13}$$

$e[m]$ is the error signal at the mth sampling period.

We substitute (6.2.10), (6.2.11), and (6.2.12) into (6.2.9), obtaining

$$u[m] = k_p\, e[m] + u_2[m-1] + k_I\, e[m]\, T + k_d\, (e[m] - e[m-1]) / T, \tag{6.2.14}$$

$$u[m] = u_2[m-1] + (k_p + k_I\, T)\, e[m] + k_d\, (e[m] - e[m-1]) / T. \tag{6.2.15}$$

Denoting $k_1 = k_p + k_I\, T$, we have

$$u[m] = u_2[m-1] + k_1 e[m] + k_d\, (e[m] - e[m-1]) / T \tag{6.2.16}$$

As discussed in this section, the nature of the system with the controller u in (6.2.5) is that in steady state, the control effort u is not zero. It has a linear relation with the position y_1, as in (6.2.8). Therefore, (6.2.16) is modified in order to be utilized in this

case. A discrete PID-like controller is proposed as

$$u[m] = u[m-1] + k_1 e[m] + k_d\,(e[m] - e[m-1])\,/\,T \tag{6.2.17}$$

The equation (6.2.17) is equivalent to

$$u[m] = u[m-1] + k_1(B_{yd}[m] - B_y[m]) +$$

$$k_d\left(\frac{B_{yd}[m] - B_{yd}[m-1])}{T} - \frac{B_y[m] - B_y[m-1])}{T}\right) \tag{6.2.18}$$

Referring to (6.2.4), (6.2.5), and (6.2.7), in case we have a value u_0 to put in (6.2.4), (6.2.5), the force F_y drives the moving platen to find an equilibrium point corresponding to (6.2.8). If a discrete PID-like control process described by (6.2.18) is started at this position, then we have the control u in the first sampling period u(0) = u_0. Theoretically, a certain value of u_0 is not required for the controller to stabilize the moving platen at the desired position of B_{yd}. However, practically, in this case, in steady state, the control u is not zero and the position of the moving platen depends on u. Therefore, if we want to implement consecutive step responses to drive the platen to follow a continuous path, the control u corresponding to the steady state of the previous step response must be used as the initial control effort of the current step response being performed. When initial control efforts are not specified properly in that way, the platen may suddenly jump to find the equilibrium position to minimize the electromagnetic force due to the initial control effort first, and then settles down to the desired position later.

In the digital control approach described by (6.2.17), for a step response, the number of iterations depends on k_1, k_d and other two factors. The first one is the step

size, or how far it is from the initial position to the desired position of the platen. The second one is the amplitude I_{12} of the current i_1 and i_2, which results in the magnitude of the force F_y as seen in (6.2.3).

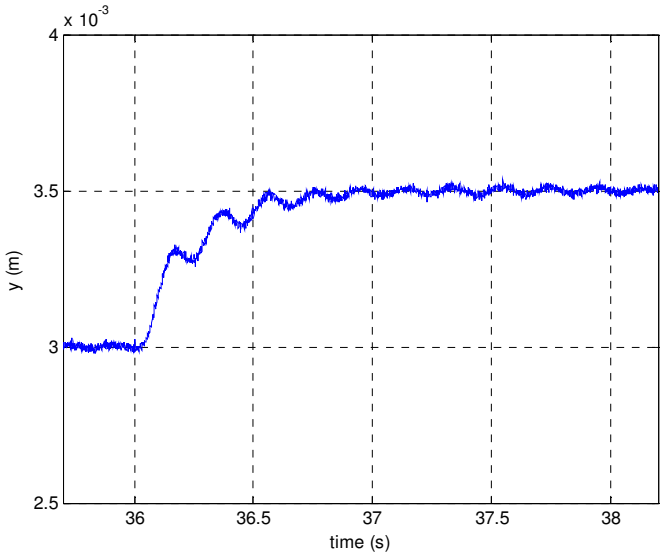

Figure 6-3: A step response of 500 μm in y, $k_1 = 0.9$, $k_d = 30$.

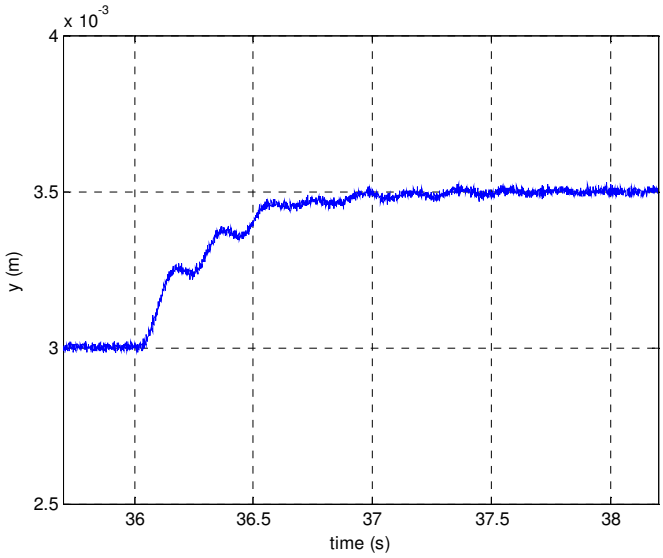

Figure 6-4: A step response of 500 μm in y, $k_1 = 0.7$, $k_d = 30$.

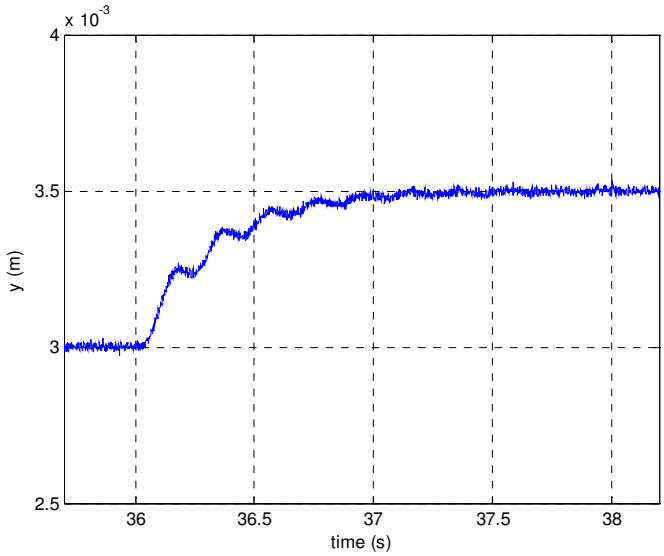

Figure 6-5: A step response of 500 μm in y, $k_1 = 0.7$, $k_d = 35$.

Figures 6-3, 6-4, and 6-5 are given to illustrate the effect of k_1 and k_p on the step responses performed with the control approach described by (2.6.17). Comparing the two step responses in Figures 6-3 and 6-4, which have the same k_d, it is seen that the response with $k_1 = 0.9$ has smaller rise time than that of the step response with $k_1 = 0.7$. However, the amplitude of fluctuation about the desired position in the first response is larger than that of the second response. The fluctuation in the second response can be even reduced by applying a smaller k_1 than 0.7. However, this will slow down the system's response. The comparison between the two responses in Figures 6-4 and 6-5, which have the same k_1, shows that k_d has the effect of reducing the fluctuation amplitude without slowing down the response.

Based on the discussion given, for the moving platen with six coils, we consider the six coils as three sets with two coils per set sharing a common controller. Totally

there are three control efforts u_{12}, u_{34}, and u_{56}.

$$i_1 = I_{12}\sin(\gamma_1 u_{12}) \tag{6.2.19}$$

$$i_2 = I_{12}\cos(\gamma_1 u_{12}) \tag{6.2.20}$$

$$i_3 = I_{34}\sin(\gamma_1 u_{34}) \tag{6.2.21}$$

$$i_4 = I_{34}\cos(\gamma_1 u_{34}) \tag{6.2.22}$$

$$i_5 = I_{56}\sin(\gamma_1 u_{56}) \tag{6.2.23}$$

$$i_6 = I_{56}\cos(\gamma_1 u_{56}) \tag{6.2.24}$$

The equations describing the controller of the system are:

$$u_{12}[m] = u_{12}[m-1] + k_{1y}(B_{y1d}[m] - B_{y1}[m]) +$$

$$k_{dy}\left(\frac{B_{y1d}[m] - B_{y1d}[m-1])}{T} - \frac{B_{y1}[m] - B_{y1}[m-1])}{T}\right) \tag{6.2.25}$$

$$u_{34}[m] = u_{34}[m-1] + k_{1y}(B_{y2d}[m] - B_{y2}[m]) +$$

$$k_{dy}\left(\frac{B_{y2d}[m] - B_{y2d}[m-1])}{T} - \frac{B_{y2}[m] - B_{y2}[m-1])}{T}\right) \tag{6.2.26}$$

$$u_{56}[m] = u_{56}[m-1] + k_{1x}(B_{xd}[m] - B_{x}[m]) +$$

$$k_{dx}\left(\frac{B_{xd}[m] - B_{xd}[m-1])}{T} - \frac{B_{x}[m] - B_{x}[m-1])}{T}\right) \tag{6.2.27}$$

B_{y1} and B_{y2} are the y-component magnetic flux densities sensed by sensor 1 and sensor 2, respectively. The sensor numbers and positions are given in Figure 5-5. B_{y1d} and B_{y2d} are the corresponding magnetic flux densities at the desired position of the moving platen along the y-axis. B_x is the x-component magnetic flux density sensed by the sensor 1 or the sensor 2. B_{xd} is the corresponding magnetic flux density at the desired position of the

moving platen along the x-axis. There is only one pair of parameters k_{1y} and k_{dy} for the set of coils 1 and 2 and the set of coils 3 and 4.

From the results of Subsection 3.2.5, (6.2.1) and (6.2.2), the electromagnetic force F_x acting on the platen due to the currents i_5 and i_6 is:

$$F_x = 2b_{x5}i_5 + 2b_{x6}i_6$$

$$F_x = 2b_0 \sin[\gamma_1(x_6 + \frac{v}{2})]i_5 - 2b_0 \cos[\gamma_1(x_6 + \frac{v}{2})]i_6 \tag{6.2.28}$$

Equations (6.2.23) and (6.2.24) are substituted into (6.2.28), yielding

$$F_x = 2b_0 I_{56}\{\sin[\gamma_1(x_6 + \frac{v}{2})]\sin(\gamma_1 u_{56}) - \cos[\gamma_1(x_6 + \frac{v}{2})]\cos(\gamma_1 u_{56})\} \tag{6.2.29}$$

$$= -2b_0 I_{56} \cos[\gamma_1(x_6 + \frac{v}{2} + u_{56})]$$

The force F_x generate a torque about the z'-axis. In order to balance this torque, two forces with equal magnitudes and opposite directions are generated by the set of coils 1 and 2 and the set of coils 3 and 4. We denote the amount of forces changed in the set of coil 1 and 2 and the set of coils 3 and 4 as F_b.

$$F_b\ (3L/2) - F_x c_{56} = 0 \tag{6.2.30}$$

$$F_b = 2F_x c_{56} / (3L) \tag{6.2.31}$$

The force acting on the platen in y due to the set of i_1 and i_2 is:

$$F_{12y} = 2(b_{y1}i_1 + b_{y2}i_2)$$

$$F_{12y} = -2b_0 \cos[\gamma_1(y_1 - \frac{v}{2})]I_{12} \sin(\gamma_1 u_{12}) + 2b_0 \sin[\gamma_1(y_1 - \frac{v}{2})]I_{12} \cos(\gamma_1 u_{12})$$

$$F_{12y} = 2b_0 I_{12} \sin[\gamma_1(y_1 - \frac{v}{2} - u_{12})] \tag{6.2.32}$$

The force acting on the platen along y due to the set of i_3 and i_4 is:

$$F_{34y} = 2(b_{y3} i_3 + b_{y4} i_4)$$

$$F_{34y} = 2b_0 \sin[\gamma_1(y_1 - \frac{v}{2})] I_{34} \sin(\gamma_1 u_{34}) - 2b_0 \cos[\gamma_1(y_1 - \frac{v}{2})] I_{34} \cos(\gamma_1 u_{34})$$

$$F_{34y} = -2b_0 I_{34} \cos[\gamma_1(y_1 - \frac{v}{2} + u_{34})] \tag{6.2.33}$$

We assume that Δu_{12} and Δu_{34} are the amount of control effort changed to balance the torque generate by the force F_x about the z'-axis. From (6.2.32), the new force after being compensated by Δu_{12} is

$$F_{12y\_new} = 2b_0 I_{12} \sin[\gamma_1(y_1 - \frac{v}{2} - u_{12} - \Delta u_{12})], \tag{6.2.34}$$

$$F_{12y\_new} = F_{12y} \cos(\gamma_1 \Delta u_{12}) - 2b_0 I_{12} \cos[\gamma_1(y_1 - \frac{v}{2} - u_{12})] \sin(\gamma_1 \Delta u_{12}). \tag{6.2.35}$$

In the motions along y with the y-direction forces to actuate the platen generated by the coils 1, 2, 3 and 4, the coils 5 and 6 are only energized to remove small disturbances in x. With this reason, Δu_{12} can be considered sufficiently small so that $\cos(\gamma_1 \Delta u_{12}) = 1$ and $\sin(\gamma_1 \Delta u_{12}) = \gamma_1 \Delta u_{12}$. Equation (6.2.35) becomes the following

$$F_{12y\_new} = F_{12y} - 2b_0 I_{12} \cos[\gamma_1(y_1 - \frac{v}{2} - u_{12})] \gamma_1 \Delta u_{12} \tag{6.2.36}$$

By comparing (6.2.31) and (6.2.36), we have:

$$F_b = 2F_x c_{56} / (3L) = -2b_0 I_{12} \cos[\gamma_1(y_1 - \frac{v}{2} - u_{12})] \gamma_1 \Delta u_{12} \tag{6.2.37}$$

$$\Delta u_{12} = \frac{-F_x c_{56}}{3Lb_0 I_{12}\gamma_1 \cos[\gamma_1(y_1 - \frac{v}{2} - u_{12})]} \tag{6.2.38}$$

Fortunately, the y-direction forces have a tendency to drive the platen to find an equilibrium position. This position is corresponding to (6.2.7),

$$\sin[\gamma_1(y_1 - \frac{v}{2} - u_{12})] = 0 .$$

Therefore, the singularity in (6.2.38) due to

$$\cos[\gamma_1(y_1 - \frac{v}{2} - u_{12})] = 0$$

does not happen.

The Δu_{34} is derived in a similar way. However, because of the symmetry of the platen, which gives $y_1 = y_4$ and the two forces added to balance the platen should have equal magnitudes and opposite directions, one can specify directly $\Delta u_{34} = -\Delta u_{12}$.

CHAPTER VII

EXPERIMENTAL RESULTS

This chapter presents the experimental results from running the multi-axis positioner with the discrete PID-like control approach discussed above in Subsection 6.2. Micro-scale step responses in translational motions in the *x*-axis and the *y*-axis and rotational motion about the *z*-axis were performed. Along with this are long-range motions in the *x*-axis and the *y*-axis and the position profile in speed-varying motion in *x* and *y*. Figures 7-1 and 7-2 respectively shows responses of consecutive steps along *x* with the step sizes of 8 μm and 10 μm. This is to determine the positioning resolution in *x*. As seen from Figure 7-1, the positioner demonstrates a positioning resolution better than 8 μm in *x*. Figures 7-3, 7-4, and 7-5 shows the step responses of 20 μm, 50μm, and 100 μm, respectively, and the corresponding perturbations in *y* and φ. In Figures 7-6 and 7-7, there are staircase responses in *x* with the step sizes of 500 μm and 1000 μm, respectively. Figure 7-8 (a) and (b) shows consecutive steps along *y* with the step sizes of 8 μm and 10 μm, respectively. Being similar to the case of *x*, the positioning resolution achieved in *y* is 8 μm. Figures 7-9, 7-10, and 7-11 shows the step responses of 20 μm, 50 μm and 100 μm and along *y* and the corresponding perturbations in *x* and φ. Two staircase responses of 500 μm and 1000 μm in *y* are given in Figure 7-12 (a) and (b), respectively.

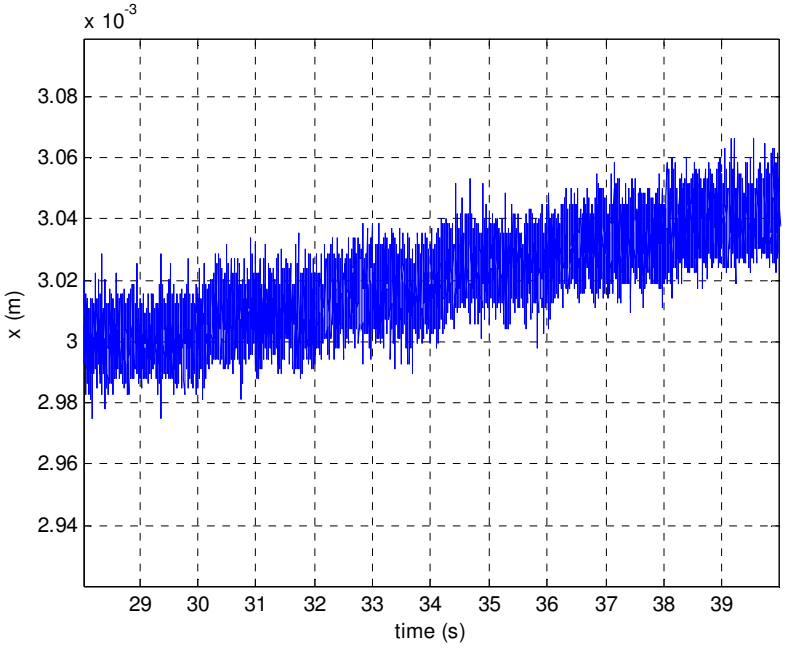

Figure 7-1: Five consecutive steps of 8 µm in *x*.

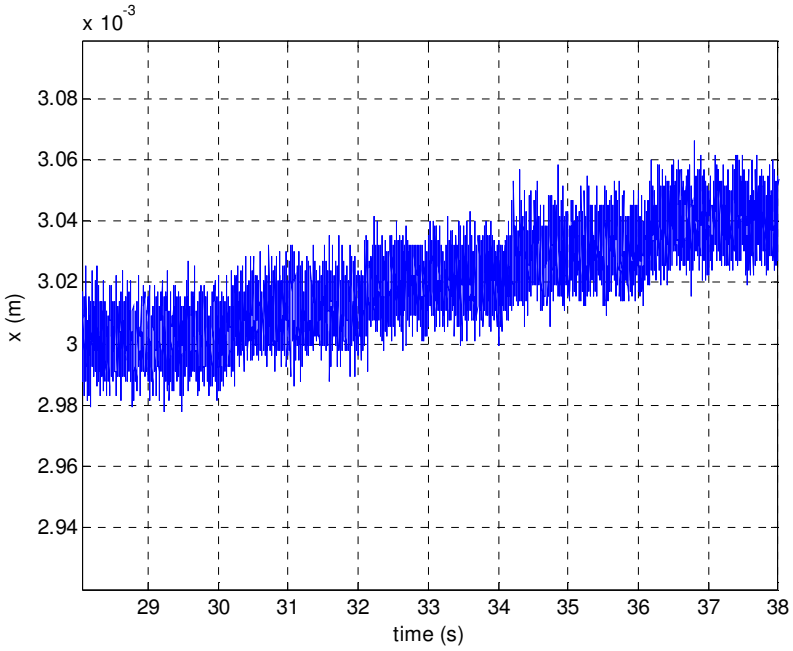

Figure 7-2: Four consecutive steps of 10 µm in *x*.

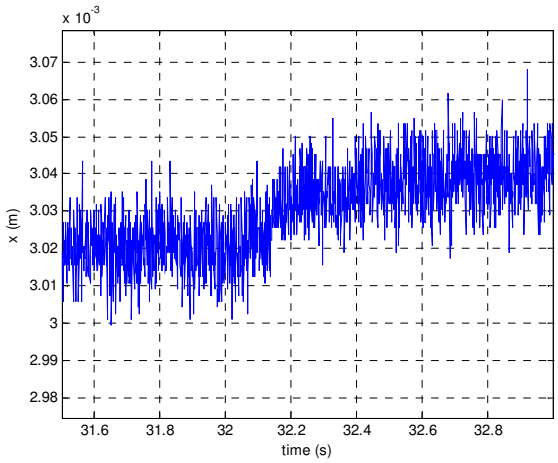

(a)

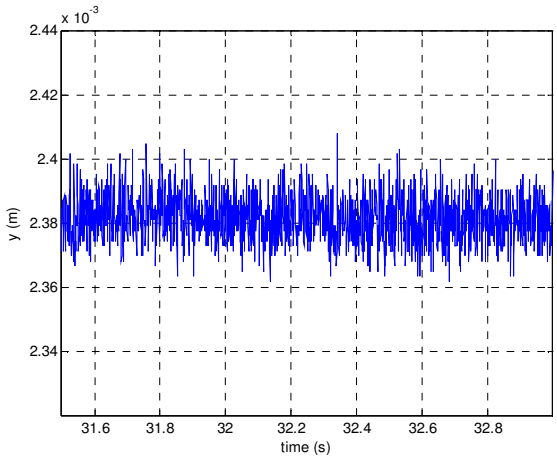

(b)

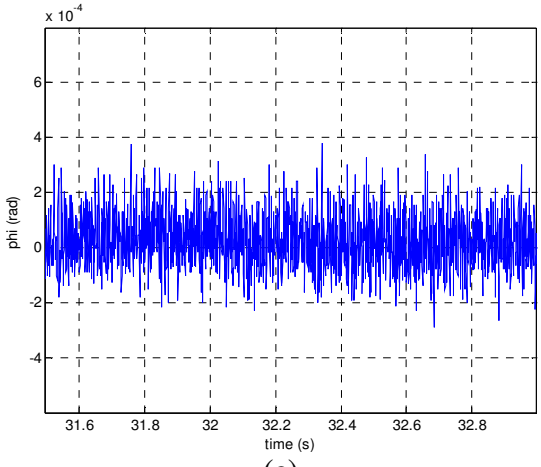

(c)

Figure 7-3: (a) 20 µm step in x and perturbations (b) in y and (c) in φ.

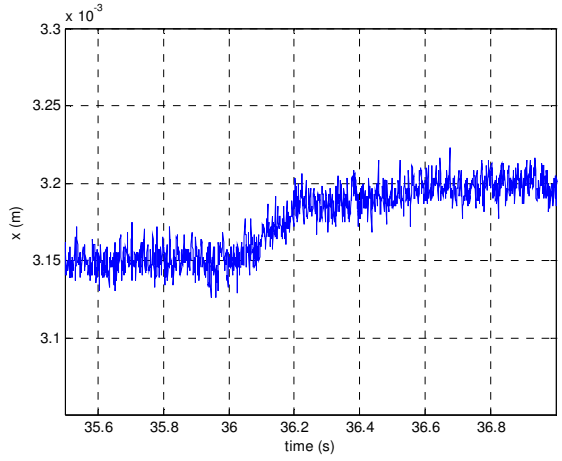

(a)

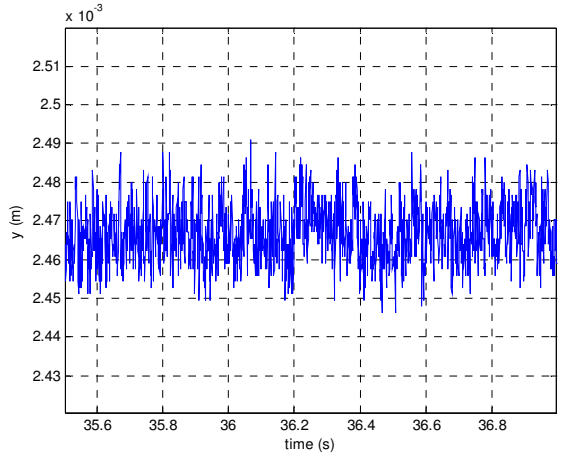

(b)

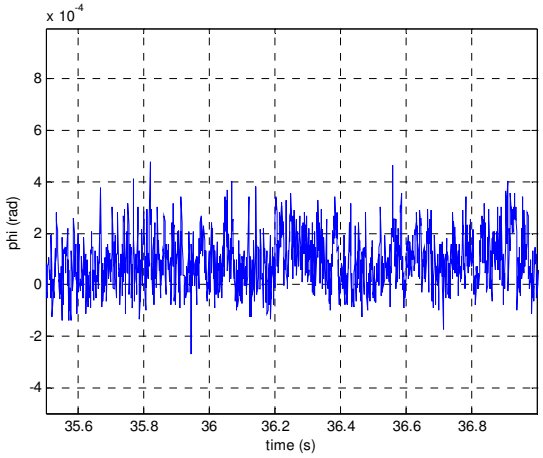

(c)

Figure 7-4: (a) 50 µm step in *x* and perturbations (b) in *y* and (c) in φ.

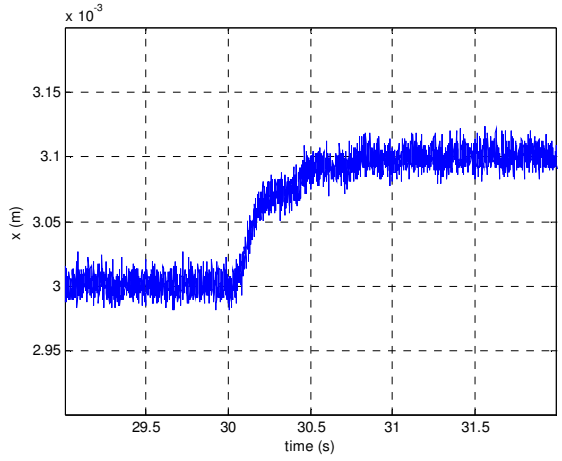

(a)

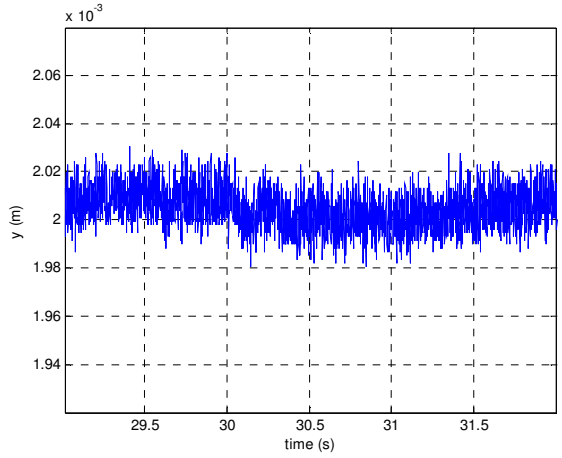

(b)

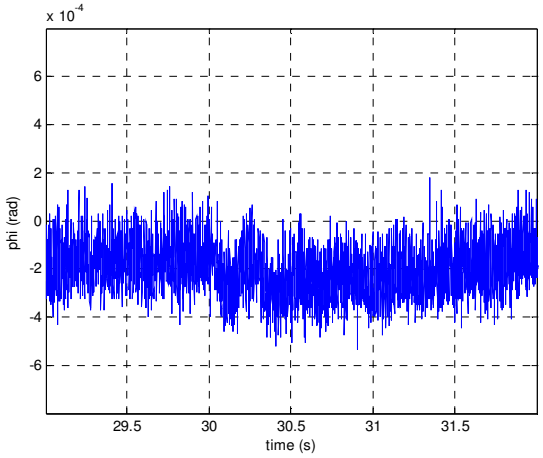

(c)

Figure 7-5: (a) 100 µm step in *x* and perturbations (b) in *y* and (c) in φ.

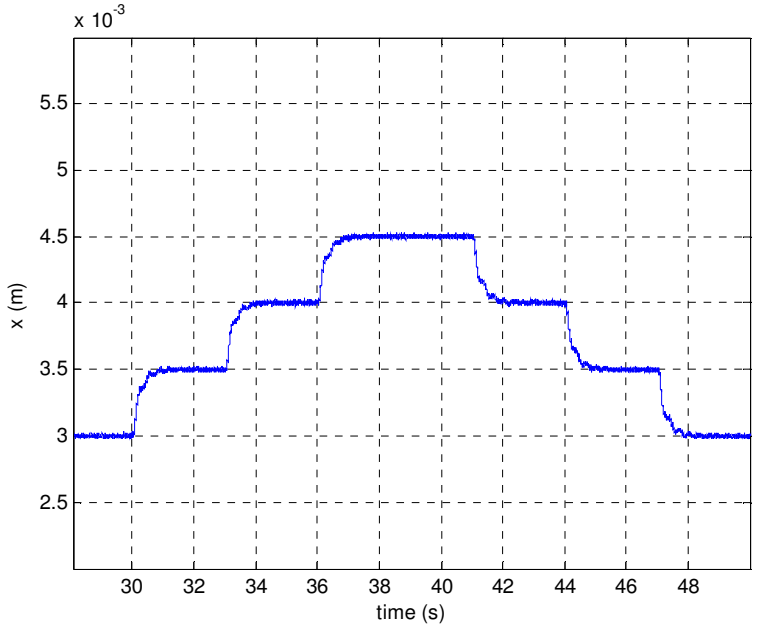

Figure 7-6: A stair-case response with step size of 500 µm in *x*.

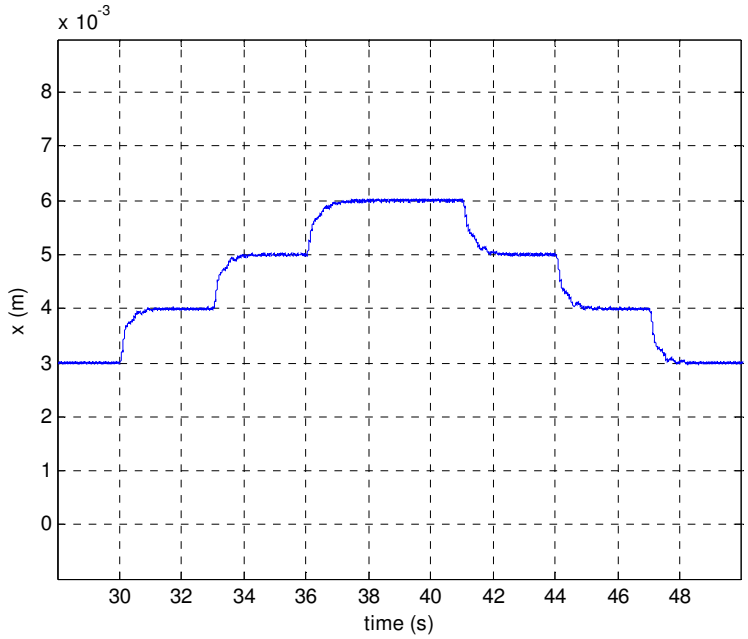

Figure 7-7: A stair-case response with step size of 1000 µm in *x*.

As can be seen from Figures 7-3, 7-4 and 7-5, in the step responses in x with k_1 = 0.9 and k_p = 30, with the step sizes of 20 µm, 50 µm, and 100 µm, the rise times are 0.25 s, 0.4 s, 0.5 s and the settling times are 0.4 s, 0.5 s, and 0.8 s, respectively. There are three points that make this system different from a linear time invariant system following a classical PID control approach. Firstly, the force-current relation, which has the form of $\boldsymbol{F} = \boldsymbol{A}\,\boldsymbol{i}$, is position dependent. For a step size of 20 µm or shorter, the matrix $\boldsymbol{A}$ during the response can be considered non-varying. However, with a step size of 50 µm or longer, the $\boldsymbol{A}$ matrix varies. Secondly, putting the control input in the form of (6.2.5), the system dynamics is no longer in the form of $m\ddot{x} = bu$ but $m\ddot{x} = b\sin(\gamma u)$ with b and γ being some constants. Thirdly, what proposed and tested in this case is not actually a discrete-PID control approach but a modified-discrete-PID control approach as discussed in Subsection 6.2.

In Figure 7-6 and 7-7, the consecutive step responses are consistent with settling time of 0.9 s in 500 µm step size and 1 s in 1000 µm step size. The rise time is 0.6 s in both two cases. In Figure 7-9, 7-10 and 7-11, step responses of 20 µm, 50 µm and 100 µm along the y-axis have the settling time of 0.5 s, 0.5 s, and 0.9 s, and the rise time of 0.25 s, 0.4 s, and 0.5 s, respectively. The staircase responses with step sizes of 500 µm and 1000 µm in y given in Figure 7-12 (a) and (b) have the settling time of 1.1 s and 1.2 s, respectively and the rise time of 0.6 s in both cases. Comparing the step responses with step sizes of 50 µm and 100 µm, the rise times are 0.4 s and 0.5 s, and the settling times are 0.5 s and 0.8 s, respectively. In the step motions described above, when the step size is larger, or the initial position is farther from the desired position, the initial

speed of motion is higher. This is the effect of the proportional gain in the PID-like controller to reduce the rise time. If the moving platen's velocity is high, especially when it approaches or passes through the desired position, the derivative part in the PID-like controller has the effect on decreasing the platen's velocity, and therefore, reducing the overshoot and settling time of the system's response.

In different cases above, it is noticeable that the step responses with the same step sizes in *x* and *y* have the same rise time; however, the settling times in the response along *x* is smaller than that in the response along *y*. The force disturbance due to the stiffness of the wires, which are connected to the coils to power them, acts on the moving platen directly in the *y* direction. Therefore, it takes more time for the controller to stabilize the platen's position along the *y*-direction.

Comparing the perturbations in the step responses of 50 µm and 100 µm in *x* and in *y*, in the responses along *x*, the perturbations in *y* are larger than the perturbations in *x* of the responses in *y*. This is because the asymmetric structure of the platen in *x*. When the platen moves in *x*, only the set of coils 5 and 6 generate the force in the *x*-direction. The two other sets of coils are to generate two forces in *y* with the same magnitude and opposite directions to balance the torque acting on the platen about the *z'*-axis due to the force in *x*. This is different from the case of motions along *y*. In which both the set of coils 1 and 2 and the set of coils 3 and 4 arranged in a symmetric structure generate the forces in *y*.

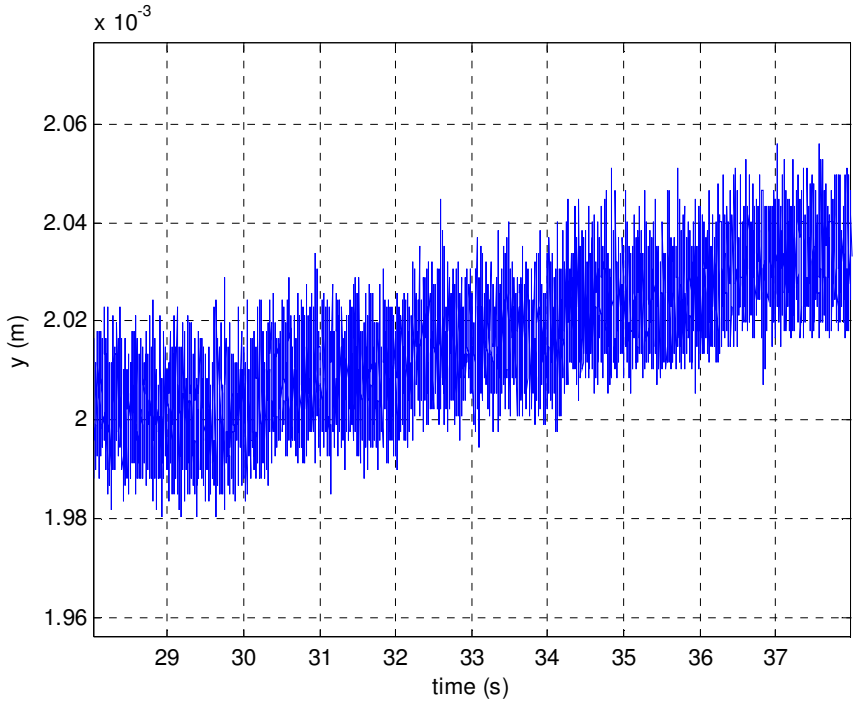

(a)

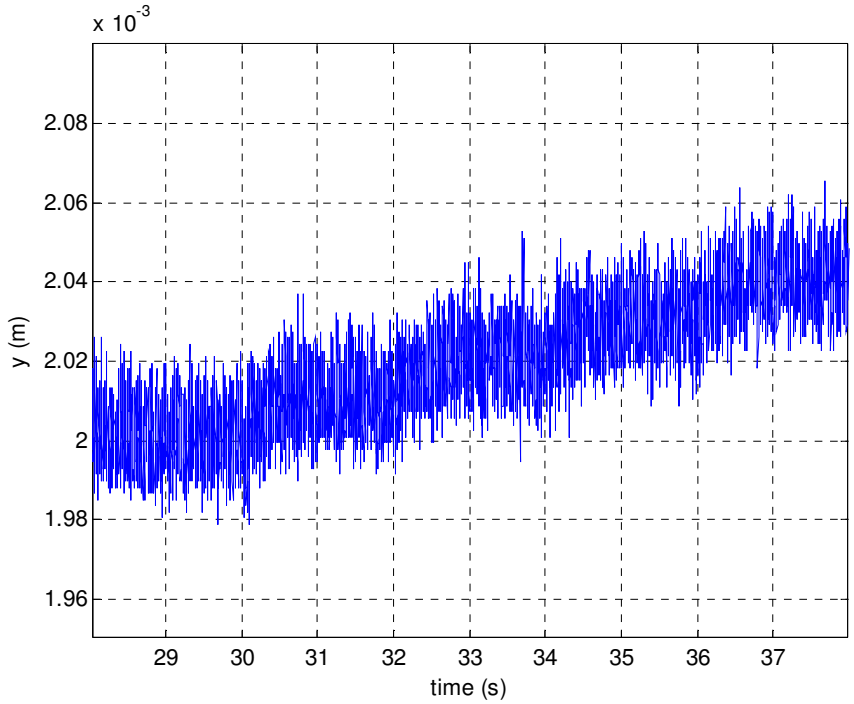

(b)

Figure 7-8: Four consecutive steps of (a) 8 µm in *y* and (b) 10 µm in *y*.

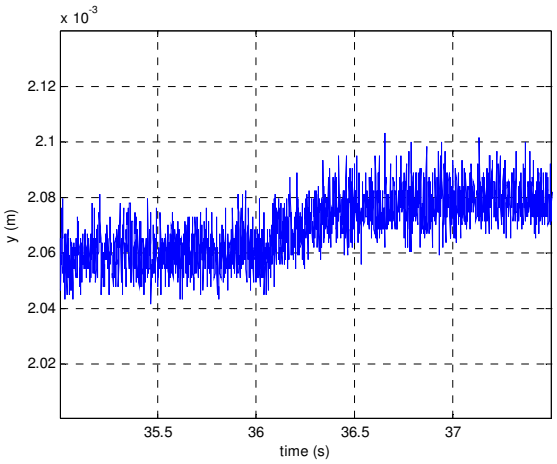

(a)

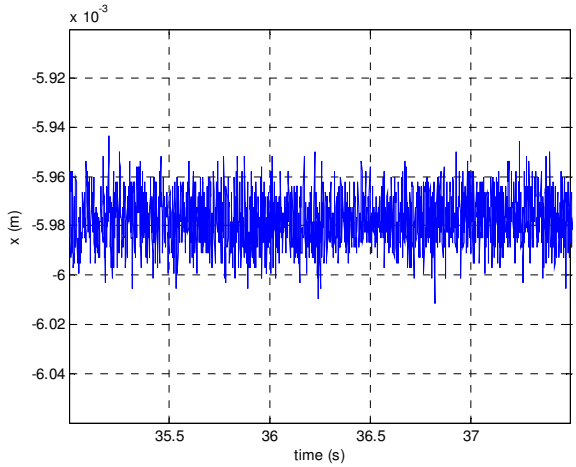

(b)

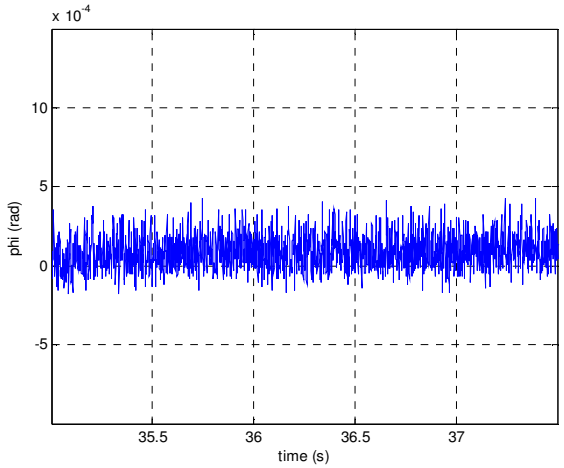

(c)

Figure 7-9: (a) A step response of 20 µm in y and perturbations (b) in x and (c) in φ.

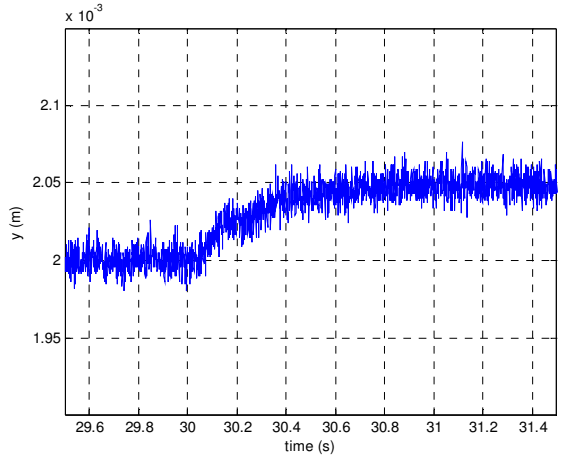

(a)

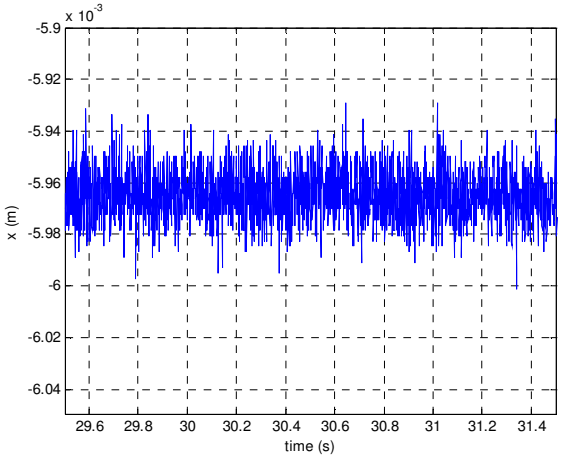

(b)

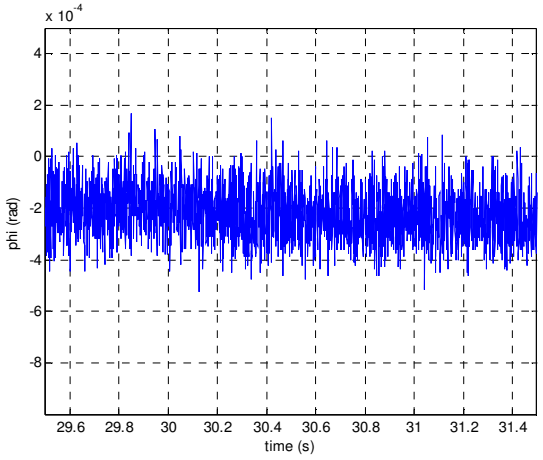

(c)

Figure 7-10: (a) A step response of 50 µm in *y* and perturbations (b) in *x* and (c) in φ.

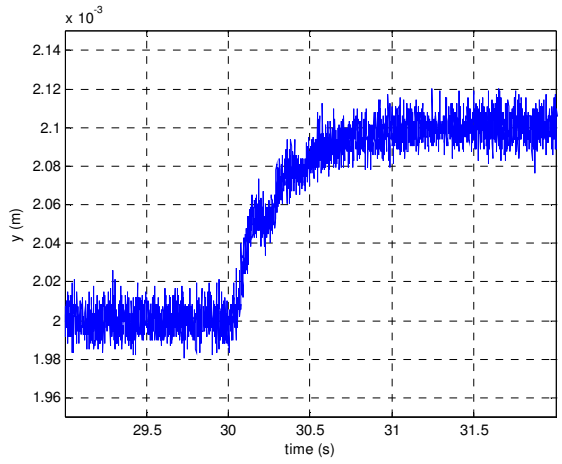

(a)

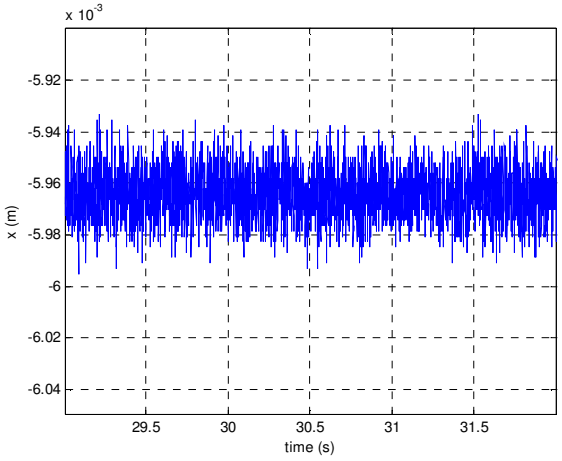

(b)

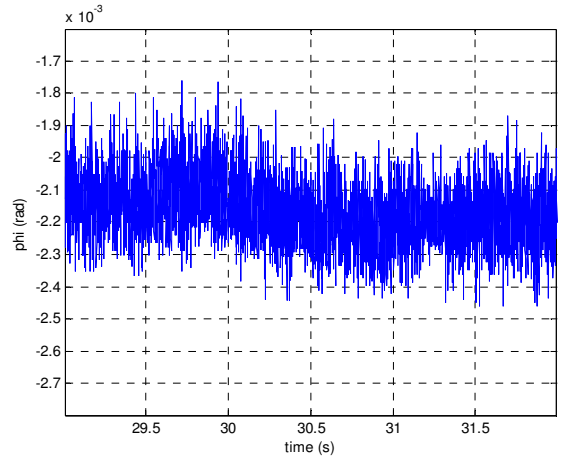

(c)

Figure 7-11: (a) A step response of 100 µm in y and perturbations (b) in x and (c) in φ.

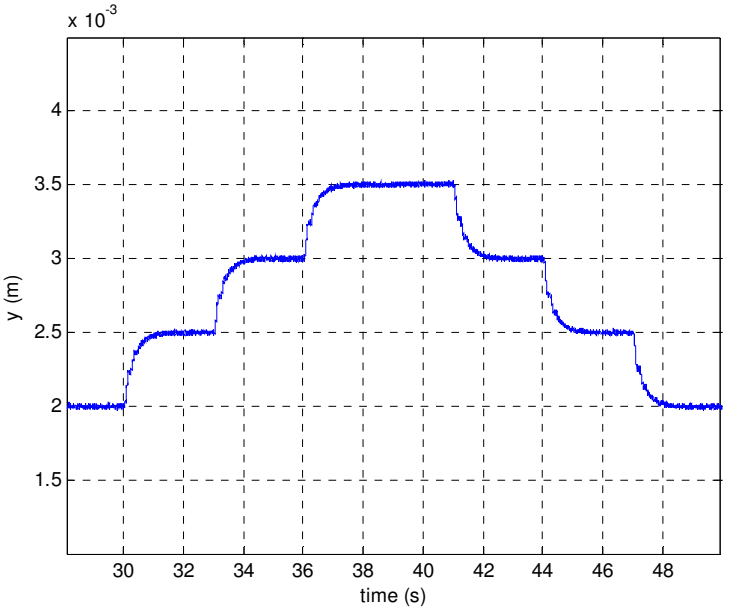

(a)

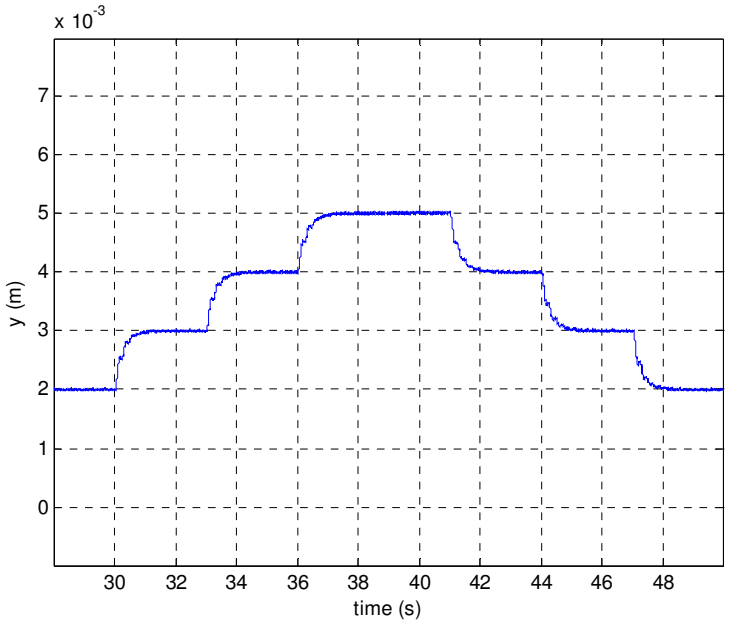

(b)

Figure 7-12: A stair-case response with step size of (a) 500 µm in *y* and (b) 1000 µm in *y*.

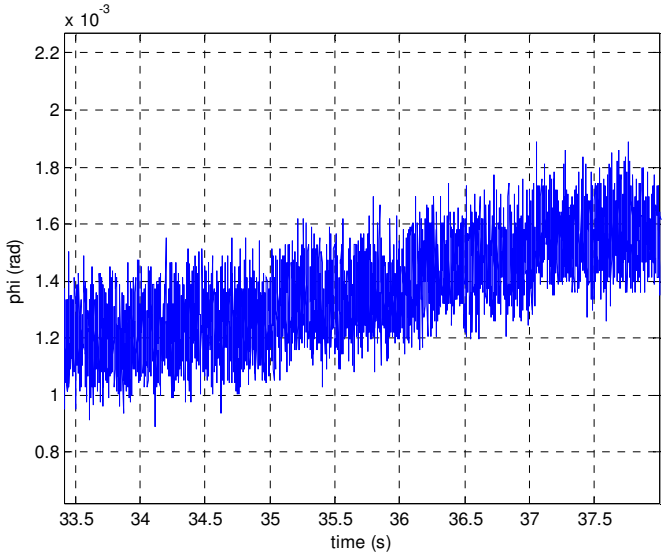

Figure 7-13: Three consecutive step responses of 1.3×10^{-4} rad.

Figure 7-13 shows the positioning resolution of 1.3×10^{-4} rad in the rotational motions about the *z'*-axis. Figures 7-13 and 7-14 gives the step responses in rotations about the *z'*-axis with perturbations in *x* and *y*; the step sizes are 2×10^{-4} rad and 0.001 rad, respectively. The step response of 0.001 rad is the only one that has a considerable overshoot of about 33 % in this series of experimental results. When a rotational motion about *z'* is performed, the set of coils 1 and 2 and the set of coils 3 and 4 are energized to generate two forces with the same magnitude and opposite directions while the set of coils 5 and 6 generate only a zero resultant force. For a small angle of rotation, the forces generated by the coils 1, 2, 3, and 4 are almost distributed in the *y*-direction. This is why in the step responses shown in Figures 7-14 and 7-15, the perturbations in *y* are larger than the perturbations in *x*.

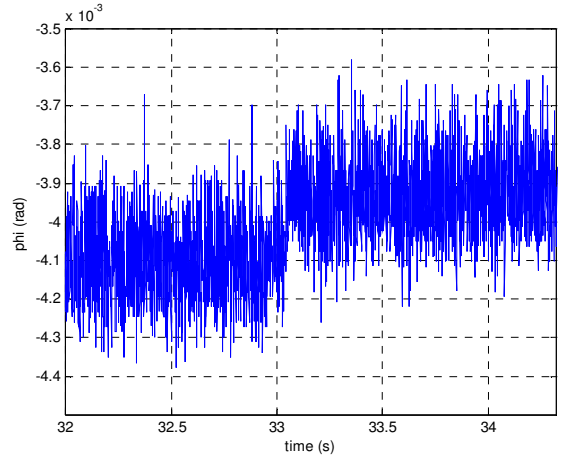

(a)

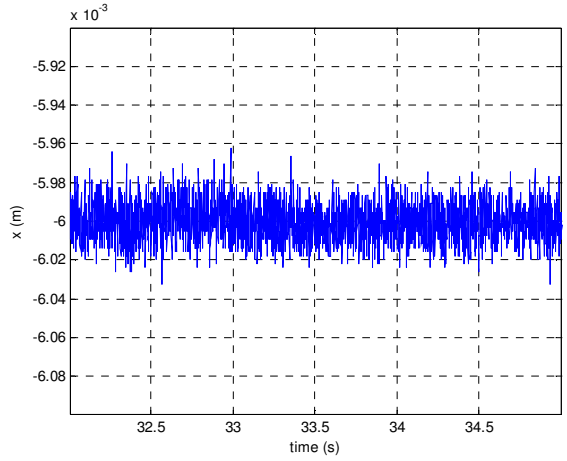

(b)

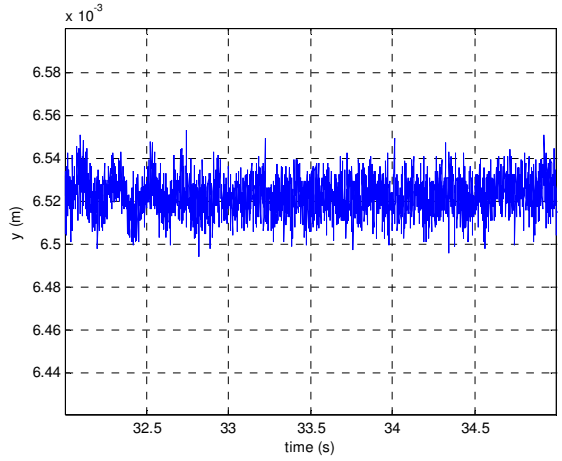

(c)

Figure 7-14: (a) A step response of 2×10^{-4} rad in φ and perturbations (b) in x and (c) in y.

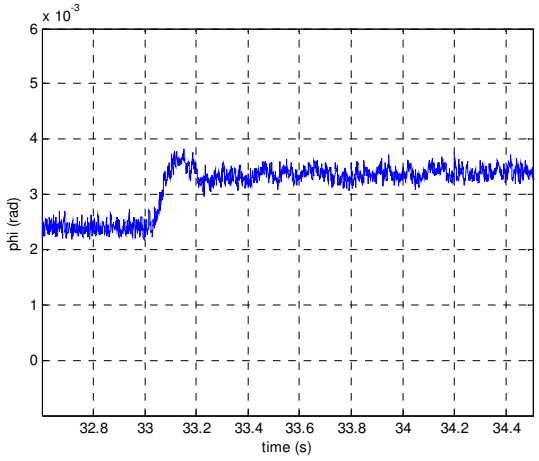

(a)

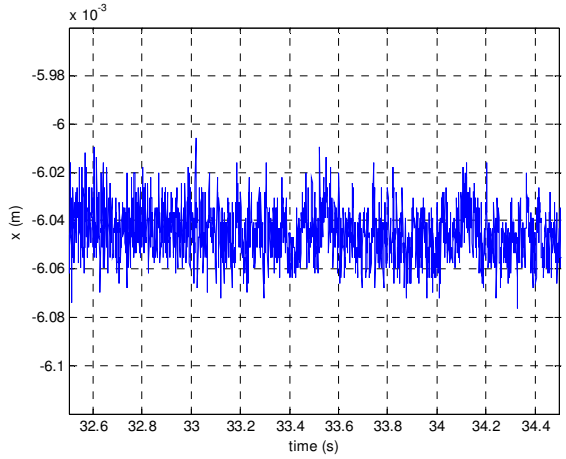

(b)

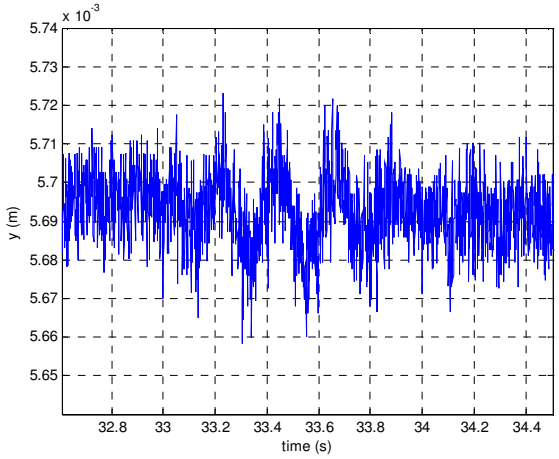

(c)

Figure 7-15: (a) A step response of 0.001 rad in φ and perturbations (b) in x and (c) in y.

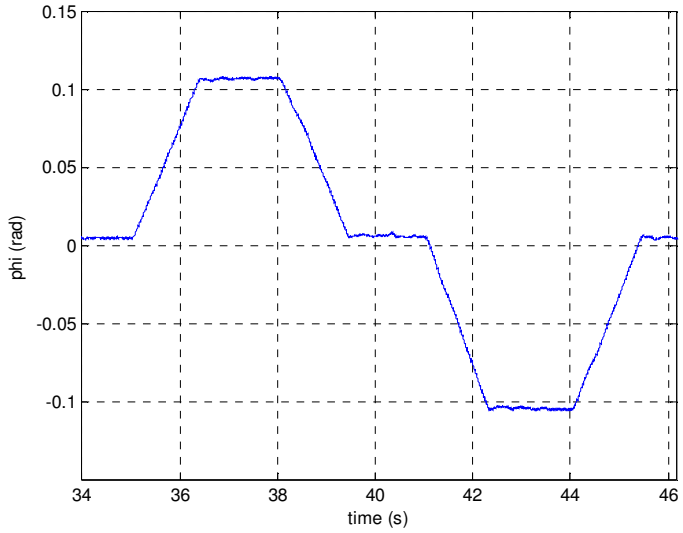

Figure 7-16: The trapezoidal angle profile of the rotations about *z'*.

Figure 7-16 shows four consecutive rotations about *z'* to form a trapezoidal angle profile. The constant angular velocity is 0.073 rad/s. The achieved travel range in the rotational motion about *z'* is 0.21 rad or 12.03°. When the angle between the axes of a Hall-effect sensors and the axes *x* and *y* gets lager, or the Hall-effect sensor rotates a larger angle from the position it aligns with the sides of the magnet matrix, the sensing noise from the Hall-effect sensor is larger. The rotational motions of the moving platen about the *z'*-axis is not limited by the capability of the actuator, or the force allocation, but by the sensing capability.

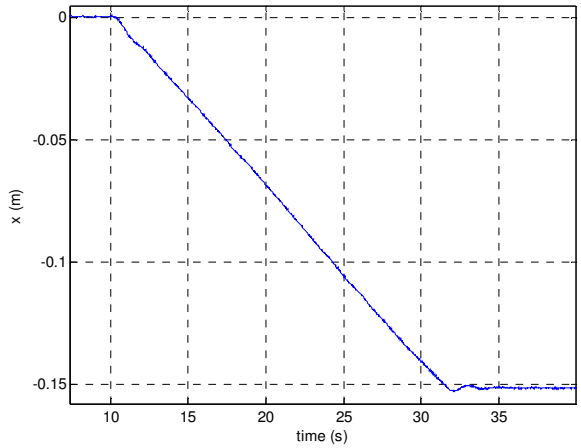

(a)

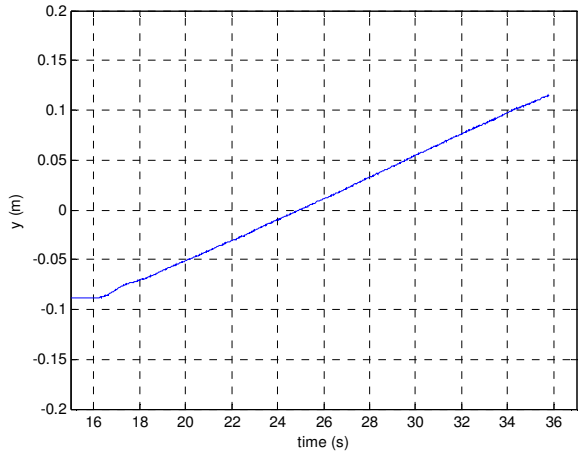

(b)

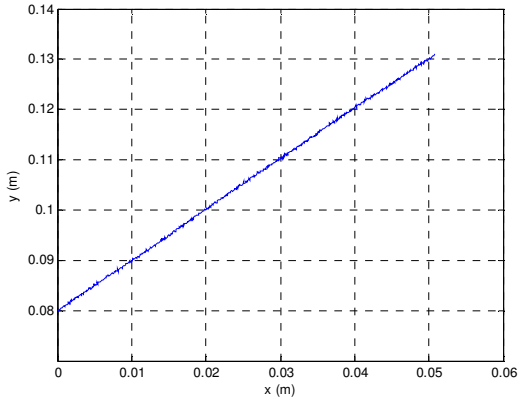

(c)

Figure 7-17: Long-range motions, (a) $3L$ = 15.24 cm in x and (b) $4L$ = 20.32 cm in y, (c) combined x-and-y translational motion of L in each direction.

A long range translational motion of $3L$ = 15.24 cm in x is shown in Figure 7-17 (a) with the constant velocity of 0.70 cm/s. A translational motion of $4L$ = 20.32 cm in y is shown in Figure 7-17 (b) with the constant velocity of 1.02 cm/s. Figure 7-15 (c) gives a x-and-y combined translational motion of L in each direction with the constant velocity of 0.25 cm/s in both x and y. Compared with the combined motion in Figure 7-15 (c) with considerably lower constant velocity and varying-speed motions in Figures 7-18 and 7-19 with velocity rising from zero, the position profiles in Figures 7-17 (a) and (b) have small fluctuations at the beginning of the profiles due to velocities jumping from zero.

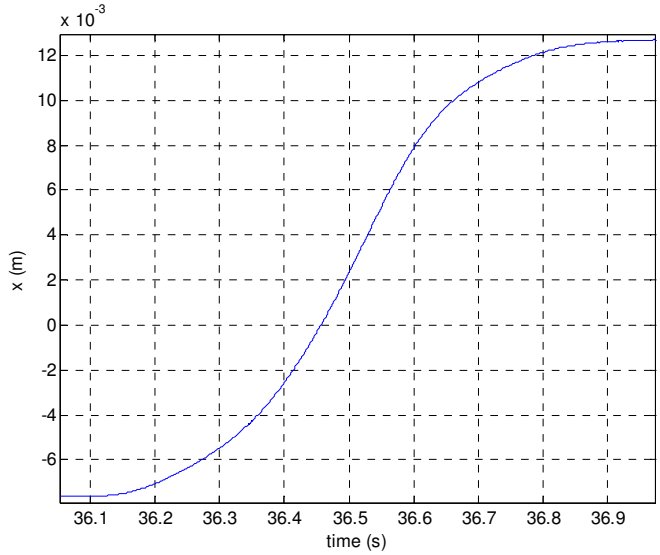

Figure 7-18: The x-profile of a motion in x with the maximum velocity of 5.25 cm/s.

Figure 7-18 is the position profile of a speed-varying motion in x with the maximum velocity of 5.25 cm/s; the constant acceleration is 10.50 cm/s^2. Figure 7-19 shows a position profile of a speed-varying motion in y. In which, the maximum velocity

is 10.5 cm/s and the constant acceleration is 42 cm/s^2.

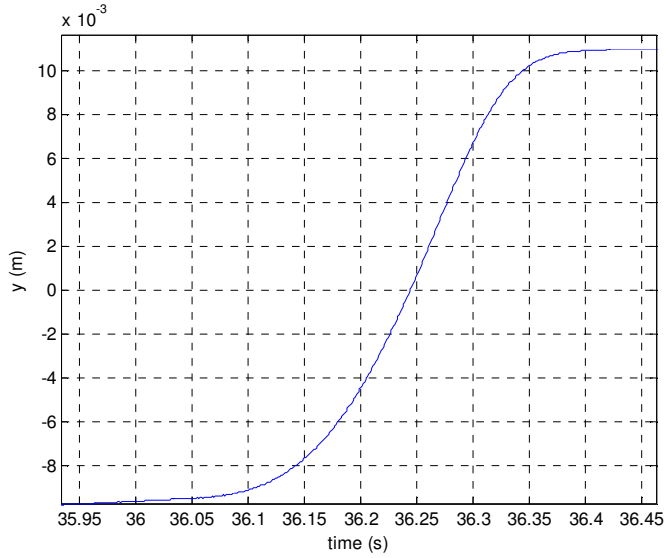

Figure 7-19: The *y*-profile of a motion in *y* with the maximum velocity of 10.5 cm/s.

In Figure 7-20, the position profile of a speed-varying motion in *x* is given. The platen's velocity in *x* rises from zero to 10.50 cm/s in 0.24 s with a constant acceleration of 43.75 cm/s^2. Figure 7-21 shows a position profile of a speed-varying motion in *y*. In which, the platen's velocity increases from zero to 16.25 cm/s in 0.17 s. The constant acceleration in this case is 95.59 cm/s^2. The achieved velocity and acceleration in *y* are higher than those in *x*. This is because the symmetric structure of the platen in *y*. When a motion in *x* is performed, the coils 5 and 6 generate a force in *x*. As discussed before, this force concurrently generates a torque acting on the platen about *z'*. This torque must be balanced by energizing the coils 1, 2, 3, and 4 to generate two forces with equal magnitudes in the positive-*y* and negative-*y* directions. Therefore, for the two translational motions along *x* and along *y* with the same velocity and acceleration, the

perturbations of y and φ in the motion along x are larger than the corresponding perturbations of x and φ in the motion along y. This is why the achieved velocity and acceleration in x are lower than those in y.

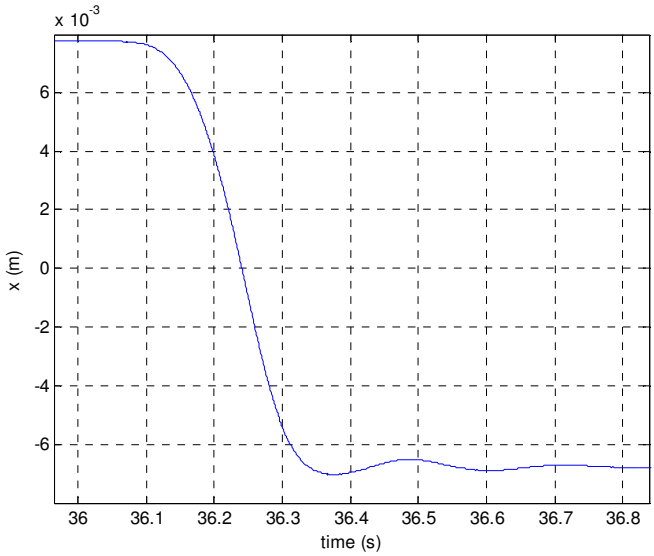

Figure 7-20: The x-profile of a motion in x for the achieved velocity and acceleration.

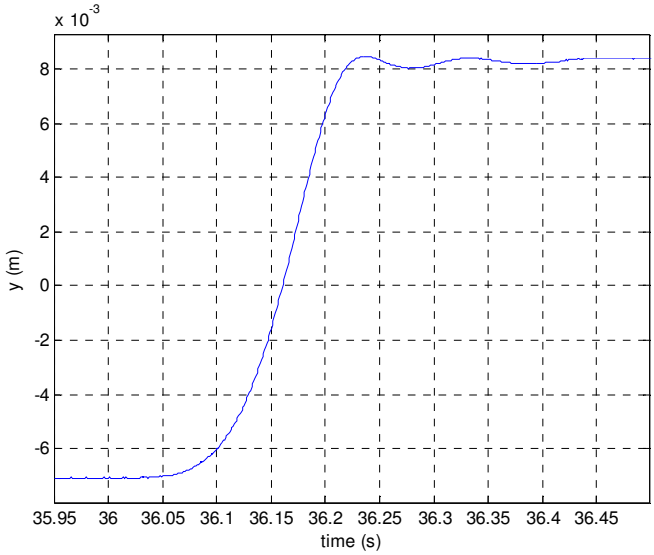

Figure 7-21: The y-profile of a motion in y for the achieved velocity and acceleration.

The root-means-square (rms) position error in x and y is 8 μm in the worst case when a Hall-effect sensor is outside the sensitive intervals as in Figure 5-4. However with two sensors to guarantee that there is always one in a sensitive interval, a 6-μm rms error in positioning along x and y is obtained.

With the electric currents given by the equations from (6.2.19) to (6.2.24), once the current amplitudes I_{12}, I_{34}, I_{56} are specified and the effect of the small coil inductances on the power consumption can be ignored, the calculation of the power consumption of the positioner is straightforward. With the maximum currents of 1 A, or $I_{12} = I_{34} = I_{56} = 1$ A, the power consumed by the positioner is

$$P = (i_1^2 + i_2^2 + i_3^2 + i_4^2 + i_5^2 + i_6^2)R\,,$$

where $R = 1.98\ \Omega$ is the resistance of a coil.

$$P = I_{12}^2[\sin^2(\gamma_1 u_{12}) + \cos^2(\gamma_1 u_{12})]R + I_{34}^2[\sin^2(\gamma_1 u_{34}) + \cos^2(\gamma_1 u_{34})]R$$

$$+ I_{56}^2[\sin^2(\gamma_1 u_{56}) + \cos^2(\gamma_1 u_{56})]R$$

$$P = (I_{12}^2 + I_{34}^2 + I_{56}^2)R = 3 \times 1.98 = 5.94 \text{ W.}$$

With the current amplitudes $I_{12} = I_{34} = I_{56} = 0.5$ A, the power consumption of the positioner is

$$P = (I_{12}^2 + I_{34}^2 + I_{56}^2)R = (3/4) \times 1.98 = 1.485 \text{ W.}$$

CHAPTER VIII

CONCLUSIONS AND FUTURE WORKS

In this thesis project, a multi-axis positioner with a 6-coil single-part platen was designed and constructed to move over a superimposed Halbach magnet matrix. A new electromagnetic design with 6 coils was proposed and tested. The newly designed moving platen has a compact size; the maximum dimensions in x and in y are 185.4 mm and 157.9 mm, respectively. The total mass of the platen is 0.64 kg. The distance from the platen's center of mass to the aluminum surface on top of the magnet matrix is 10.2 mm. Based on the Lorentz force law, the electromagnetic design of six coils arranged in the platen, the volume integration for force calculation, and the electric-current relation for the six-coil platen were developed. In order to deal with the nonlinearity due to trigonometric terms in the force-current relation, a discrete PD-like control approach was proposed to close the control loop. The six coils are divided into three sets with two coils per set sharing a common control effort. The experimental results verified the commutation law designed in this project and the discrete PID-like control approach.

For step responses not greater than 1000 μm along the x-direction or the y-direction, the steady-state errors and overshoots are sufficiently small to be negligible. The maximum travel range in the x-direction is $3L$ or 15.24 cm; the maximum travel range in the y-direction is $4L$, or 20.32 cm. The maximum travel range in rotational motion about the vertical axis is 0.21 rad. The positioner demonstrates a positioning resolution of 8 μm in x and y and 130 μrad in rotation about the vertical axis. The rms

positioning error obtained is 6 μm in *x* and *y*. The velocity and acceleration achieved in *x* are 10.50 cm/s and 43.75 cm/s^2, respectively. The velocity and acceleration achieved in *y* are 16.25 cm/s and 95.59 cm/s^2, respectively. The positioner is highly applicable in stepping and scanning applications with large travel ranges in two orthogonal directions.

With the ADC sampling rate of 1 kHz, the corner frequency of 217 Hz to filter the signals sensed from the Hall-effect sensors, the sensing noise still presents. For the applications that require higher positioning precision, this positioner with Hall-effect sensors and the rms positioning error of 6 μm is insufficient. However, the electromagnetic commutation, the working principle of the moving platen, and the control approach have been verified.

A future work can combine Hall-effect sensors with Laser Interferometers to create a map between the data sensed from two types of sensors and to complement each other. This definitely increases the positioning resolution while the positioner maintains large motion ranges by the Hall-effect sensors.

REFERENCES

[1] W.-J. Kim, “High-precision planar magnetic levitation,” Ph.D. dissertation, Massachusetts Institute of Technology, Cambridge, MA, June 1997.

[2] Trumper, D. L., Kim, W.-J., and Williams, M. E., “Magnetic array,” US PTO Patent No. 5,631,618, May 20, 1997.

[3] M. Quirk and J. Serda, *Semiconductor Manufacturing Technology.* Upper Saddle River, NJ: Prentice-Hall, 2001.

[4] C. Mack, *Fundamental Principles of Optical Lithography: The Science of Microfabrication.* Chichester, West Sussex, UK: John Wiley & Sons Ltd, 2007.

[5] R. Doering and Y. Nishi, *Handbook of Semiconductor Manufacturing Technology.* Boca Raton, FL: Taylor & Francis Group. 2008.

[6] T. -J. Hu, “Design and control of a 6-degree-of-freedom levitated positioner with high precision,” Ph.D. dissertation, Texas A&M University, College Station, TX, May 2005.

[7] Ir. J. C. Compter, “Electro-dynamic planar motor”, *Precision Engineering*, vol. 28, pp. 171−180, 2004.

[8] C. M. M. Van Lierop, J. W. Jansen, A. A. H. Damen, E. A. Lomonova, P. P. J. van den Bosch, and A. J. A. Vandenput, “Model-based commutation of a long-stroke magnetically levitated linear actuator,” *IEEE Trans. Ind. Appl.,* vol. 45, no. 6, pp. 1982−1990, 2009.

[9] C. M. M. van Lierop, J. W. Jansen, A. A. H. Damen, and P. P. J. Van den Bosch, “Control of multi-degree-of-freedom planar actuators,” in *Proc. IEEE Int. CCA,* Munich, Germany, Oct. 2006, pp. 2516−2521.

[10] H. Yu, “Design and control of a compact 6-Degree-of-Freedom precision positioner with linux-based real-time control,” Ph.D. dissertation, Texas A&M University, College Station, TX, Aug. 2009.

[11] Y. Ueda and H. Ohsaki, “A planar actuator with a small mover travelling over large yaw and translational displacements,” *IEEE Trans. Magn.*, vol. 44, no. 5, pp. 609-616, 2008.

[12] K. Halbach, "Design of permanent multipole magnets with oriented rare earth cobalt material," *Nuclear Instruments and Methods,* vol. 169, no. 1, pp. 1-10,

1980.

[13] Kim, W.-J., Bhat, N. D., and Hu, T., "Integrated multidimensional positioner for precision manufacturing," *Journal of Engineering Manufacture*, vol. 218, no. 4, pp. 431–442, 2004.

[14] McMaster Carr website. [Online]. Available: http://www.mcmaster.com, 2010.

[15] Nelson Air Corp. website. [Online]. Available: http://www.nelsonair.com, 2010.

[16] Pentek Inc. website. [Online]. Available: http://www.pentek.com, 2010.

[17] Sentron AG website. [Online]. Available: http://www.sentron.ch, 2010.

[18] PA12A/APEX datasheet. [Online]. Available: http://www.datasheetcatalog.com/datasheets_pdf/P/A/1/2/PA12A.shtml, 2010.

APPENDIX

Matlab code

```
%%The Field Solution


clear,clc;

mui = 4 * pi * 10^(-7);
muiMo   = 0.71;
muiMoZ  = muiMo * (2^(0.5)) / pi;

L = 0.0508;
alpha = 2*pi/L;
delta = L/4;            % 0.0127, size of a cubic magnet, unit: m
z0 = 3*0.001;           % the air gap = 1.5 mm, thickness of the alum sheet +
                        % epoxy is 1.5 mm
z1 = z0;
n = 25;                 % number n in the Fourier expansion
RE = 200;               % Number of samples in each pitch of the magnet
nu = 6*RE + 1;          % Number of samples in the whole 6-pitch magnet array
y = 1:1:nu;
x = 1:1:nu;

Baz1 = 1:1:nu;
Baz5 = 1:1:nu;
Bay1 = 1:1:nu;
Bay5 = 1:1:nu;
Baz = 1:1:nu;
```

```
Bay = 1:1:nu;
Bbz1 = 1:1:nu;
Bbz5 = 1:1:nu;
Bbx1 = 1:1:nu;
Bbx5 = 1:1:nu;

Bbz = 1:1:nu;
Bbx = 1:1:nu;

for dem=1:nu
    y(dem) = -3*L + (dem-1)*L/RE;
    x(dem) = -3*L + (dem-1)*L/RE;

    Baz1(dem) = 0;
    Baz5(dem) = 0;
    Bay1(dem) = 0;
    Bay5(dem) = 0;

    Baz(dem) = 0;
    Bay(dem) = 0;


    Bbz1(dem) = 0;
    Bbz5(dem) = 0;
    Bbx1(dem) = 0;
    Bbx5(dem) = 0;

    Bbz(dem) = 0;
    Bbx(dem) = 0;
```

```
end
for m = 0:floor((n-1)/8)
    Baz1 = Baz1 + muiMoZ * (1 /(8*m + 1)) * (1-exp(-alpha*delta*(8*m+1))) * exp(-
    alpha * z0 * (8*m+1))* 2 * cos(alpha*(8*m+1).*y);
    Bbz1 = Bbz1 + muiMoZ * (1 /(8*m + 1)) * (1-exp(-alpha*delta*(8*m+1))) * exp(-
    alpha * z1 * (8*m+1))* 2 * cos(alpha*(8*m+1).*x);

    Bay1 = Bay1 + muiMoZ * (1 /(8*m + 1)) * (1-exp(-alpha*delta*(8*m+1))) * exp(-
    alpha * z0 * (8*m+1))* (-2) * sin(alpha*(8*m+1).*y);
    Bbx1 = Bbx1 + muiMoZ * (1 /(8*m + 1)) * (1-exp(-alpha*delta*(8*m+1))) * exp(-
    alpha * z1 * (8*m+1))* (-2) * sin(alpha*(8*m+1).*x);
end

for m = 0:floor((n-5)/8)
    Baz5 = Baz5 - muiMoZ * (1 /(8*m + 5)) * (1-exp(-alpha*delta*(8*m+5))) * exp(-
    alpha * z0 * (8*m+5))* 2 * cos(alpha*(8*m+5).*y);
    Bbz5 = Bbz5 - muiMoZ * (1 /(8*m + 5)) * (1-exp(-alpha*delta*(8*m+5))) * exp(-
    alpha * z1 * (8*m+5))* 2 * cos(alpha*(8*m+5).*x);

    Bay5 = Bay5 - muiMoZ * (1 /(8*m + 5)) * (1-exp(-alpha*delta*(8*m+5))) * exp(-
    alpha * z0 * (8*m+5))* (-2) * sin(alpha*(8*m+5).*y);
    Bbx5 = Bbx5 - muiMoZ * (1 /(8*m + 5)) * (1-exp(-alpha*delta*(8*m+5))) * exp(-
    alpha * z1 * (8*m+5))* (-2) * sin(alpha*(8*m+5).*x);
end

Baz = Baz1 + Baz5;
Bbz = Bbz1 + Bbz5;

Bay = Bay1 + Bay5;
```

```
Bbx = Bbx1 + Bbx5;
[X, Y] = meshgrid(x,y);
BaZ1 = 0.* X + 0.*Y;
BaZ5 = 0.* X + 0.*Y;
BbZ1 = 0.* X + 0.*Y;
BbZ5 = 0.* X + 0.*Y;
BZ = 0.* X + 0.*Y;

BaY1 = 0.* X + 0.*Y;
BbX1 = 0.* X + 0.*Y;
BaY5 = 0.* X + 0.*Y;
BbX5 = 0.* X + 0.*Y;
BaY = 0.* X + 0.*Y;
BbX = 0.* X + 0.*Y;

for m = 0:floor((n-1)/8)
    BaZ1 = BaZ1 + muiMoZ * (1 /(8*m + 1)) * (1-exp(-alpha*delta*(8*m+1))) * exp(-
    alpha * z0 * (8*m+1))* 2 .* cos(alpha*(8*m+1).*Y);
    BbZ1 = BbZ1 + muiMoZ * (1 /(8*m + 1)) * (1-exp(-alpha*delta*(8*m+1))) * exp(-
    alpha * z1 * (8*m+1))* 2 .* cos(alpha*(8*m+1).*X);

    BaY1 = BaY1 + muiMoZ * (1 /(8*m + 1)) * (1-exp(-alpha*delta*(8*m+1))) *
    exp(-alpha * z0 * (8*m+1))* (-2) * sin(alpha*(8*m+1).*Y);
    BbX1 = BbX1 + muiMoZ * (1 /(8*m + 1)) * (1-exp(-alpha*delta*(8*m+1))) *
    exp(-alpha * z1 * (8*m+1))* (-2) * sin(alpha*(8*m+1).*X);
end

for m = 0:floor((n-5)/8)
```

```
        BaZ5 = BaZ5 - muiMoZ * (1 /(8*m + 5)) * (1-exp(-alpha*delta*(8*m+5))) * exp(-
        alpha * z0 * (8*m+5))* 2 .* cos(alpha*(8*m+5).*Y);
        BbZ5 = BbZ5 - muiMoZ * (1 /(8*m + 5)) * (1-exp(-alpha*delta*(8*m+5))) * exp(-
        alpha * z1 * (8*m+5))* 2 .* cos(alpha*(8*m+5).*X);

        BaY5 = BaY5 - muiMoZ * (1 /(8*m + 5)) * (1-exp(-alpha*delta*(8*m+5))) * exp(-
        alpha * z0 * (8*m+5))* (-2) * sin(alpha*(8*m+5).*Y);
        BbX5 = BbX5 - muiMoZ * (1 /(8*m + 5)) * (1-exp(-alpha*delta*(8*m+5))) * exp(-
        alpha * z1 * (8*m+5))* (-2) * sin(alpha*(8*m+5).*X);
end

BaZ = BaZ1 + BaZ5;
BbZ = BbZ1 + BbZ5;
BZ  = BaZ + BbZ;

BaY = BaY1 + BaY5;
BbX = BbX1 + BbX5;

figure
colormap(HSV);
mesh(X,Y,BZ), axis([-3*L 3*L -3*L 3*L -1 1]), xlabel('X (m)'), ylabel('Y (m)'),
zlabel('B (T)')

figure
mesh(X,Y,BaY), axis([-3*L 3*L -3*L 3*L -0.5 0.5]), xlabel('X (m)'), ylabel('Y (m)'),
zlabel('B (T)');

figure
```

```
mesh(X,Y,BbX), axis([-3*L 3*L -3*L 3*L -0.5 0.5]), xlabel('X (m)'), ylabel('Y (m)'),
zlabel('B (T)');
```

C code

```
/*file name: main.h*/

/*** This is the file to define the global variables for DSP files ***/
/*** Dual port memory address ***/

unsigned long int POS1;
unsigned long int POS2;
unsigned long int POS3;

unsigned long int POSS1;
unsigned long int POSS2;
unsigned long int POSS3;

unsigned long int index;
unsigned long int index2;

float sensor_a2;
float sensor_a2b1;
float sensor_a2b2;
float sensor_a2b3;
float sensor_a2b4;
float sensor_b2;
float sensor_b2b1;
float sensor_b2b2;
```

```
float sensor_b2b3;
float sensor_b2b4;

float sensor_c1;
float sensor_c1b1;
float sensor_c1b2;
float sensor_c1b3;
float sensor_c1b4;
float i1,i2,i3,i4,i5,i6;
float a2_temp;
float a2_tempb;
float c1_temp;
float c1_tempb;
unsigned long int ss;
float Bs_siny_ratio;

/*** Register Address ***/

unsigned long int       MX_Int_Clr;
unsigned long int       MX_Ctrl;
unsigned long int       Clk1_Div;
unsigned long int       Clk4_Div;
unsigned long int       AD_FIFO_Rst;
unsigned long int       AD_Data_Fmt;
unsigned long int       AD_CkSl_Sct;
unsigned long int       AD_Trig_Ctrl;
unsigned long int       AD_Mask_CD;
unsigned long int       DA_FIFO_Rst;
unsigned long int       DA_Data_Fmt;
```

```
unsigned long int       DA_CkSl_Sct;
unsigned long int       DA_Trig_Ctrl;
unsigned long int       AD_FIFO_A1;
unsigned long int       AD_FIFO_A2;
unsigned long int       AD_FIFO_B1;
unsigned long int       AD_FIFO_B2;
unsigned long int       AD_FIFO_C1;
unsigned long int       AD_FIFO_C2;
unsigned long int       AD_FIFO_D1;
unsigned long int       AD_FIFO_D2;
unsigned long int       DA_FIFO_A1;
unsigned long int       DA_FIFO_A2;
unsigned long int       DA_FIFO_B1;
unsigned long int       DA_FIFO_B2;
unsigned long int       DA_FIFO_C1;
unsigned long int       DA_FIFO_C2;
unsigned long int       DA_FIFO_D1;
unsigned long int       DA_FIFO_D2;

float   pi;
float   L;
float   p;
float   q;
float   d;
float   th;
float   c56;
float   BAz1;
float   BBz1;
float   lamda;
```

```
float    beta;
float    m;
float    inertia_z;
float    gama;
float    z1;
float    zs;
float    muiM0;
float    delta;
float    D;
float    de12;
float    de34;
float sin12temp;
float cos12temp;
float sin34temp;
float cos34temp;

/*** function ***/
void tr_low(void);
void tr_high(void);
void int_enable(void);
void int_disable(void);
void c_int01();
void adda_setup(void);

void d2a_enable(void);
void d2a_disable(void);


/*file name: dsp.h*/
/***  This is the file to define the globle varables for DSP files ***/
```

```
extern unsigned long int POS1;
extern unsigned long int POS2;
extern unsigned long int POS3;

extern unsigned long int POSS1;
extern unsigned long int POSS2;
extern unsigned long int POSS3;

extern unsigned long int index;
extern unsigned long int index2;

extern float sensor_a2;
extern float sensor_a2b1;
extern float sensor_a2b2;
extern float sensor_a2b3;
extern float sensor_a2b4;

extern float sensor_b2;
extern float sensor_b2b1;
extern float sensor_b2b2;
extern float sensor_b2b3;
extern float sensor_b2b4;

extern float sensor_c1;
extern float sensor_c1b1;
extern float sensor_c1b2;
extern float sensor_c1b3;
extern float sensor_c1b4;
```

```
extern float i1,i2,i3,i4,i5,i6;

extern float a2_temp;
extern float a2_tempb;
extern float c1_temp;
extern float c1_tempb;

extern unsigned long int ss;    /*temporarily storing the sensor data*/
extern float Bs_siny_ratio;

extern  float    pi;
extern  float    L;
extern  float    p;
extern  float    q;
extern  float    d;
extern  float    th;
extern  float    c56;
extern  float    BAz1;
extern  float    BBz1;
extern  float    lamda;
extern  float    beta;
extern  float    m;
extern  float    inertia_z;
extern  float    gama;
extern  float    z1;
extern  float    zs;
extern  float    muiM0;
extern  float    delta;
extern  float    D;
```

```
extern float de12;
extern float de34;
extern  float sin12temp;
extern  float cos12temp;
extern  float sin34temp;
extern  float cos34temp;

/*** Register Address ***/

extern unsigned long int        MX_Int_Clr;
extern unsigned long int        MX_Ctrl;
extern unsigned long int        Clk1_Div;
extern unsigned long int        Clk4_Div;
extern unsigned long int        AD_FIFO_Rst;
extern unsigned long int        AD_Data_Fmt;
extern unsigned long int        AD_CkSl_Sct;
extern unsigned long int        AD_Trig_Ctrl;
extern unsigned long int        AD_Mask_CD;
extern unsigned long int        DA_FIFO_Rst;
extern unsigned long int        DA_Data_Fmt;
extern unsigned long int        DA_CkSl_Sct;
extern unsigned long int        DA_Trig_Ctrl;
extern unsigned long int        AD_FIFO_A1;
extern unsigned long int        AD_FIFO_A2;
extern unsigned long int        AD_FIFO_B1;
extern unsigned long int        AD_FIFO_B2;
extern unsigned long int        AD_FIFO_C1;
extern unsigned long int        AD_FIFO_C2;
extern unsigned long int        AD_FIFO_D1;
```

```
extern unsigned long int        AD_FIFO_D2;
extern unsigned long int        DA_FIFO_A1;
extern unsigned long int        DA_FIFO_A2;
extern unsigned long int        DA_FIFO_B1;
extern unsigned long int        DA_FIFO_B2;
extern unsigned long int        DA_FIFO_C1;
extern unsigned long int        DA_FIFO_C2;
extern unsigned long int        DA_FIFO_D1;
extern unsigned long int        DA_FIFO_D2;
/*** function ***/

void tr_low(void);
void tr_high(void);
void int_enable(void);
void int_disable(void);
void adda_setup(void);
void d2a_enable(void);
void d2a_disable(void);


/*file name: 6102setup.c*/

#include "dsp.h"

void adda_setup()
{
        *(unsigned long *)0x100020=0;       /* Mix Bus Control Register */

        *(unsigned long *)MX_Ctrl=0x4;      /* Reset MIX board */
        *(unsigned long *)MX_Ctrl=0x0;
```

```
        *(unsigned long *)AD_FIFO_Rst=0x0;      /* Reset AD FIFO */
        *(unsigned long *)AD_Data_Fmt=0x1;      /* Set AD Data format */
        *(unsigned long *)AD_Data_Fmt=0x0;

        *(unsigned long *)MX_Int_Clr=0x0;       /*  Clear any pending MIX
                                                interrupts */
        *(unsigned long *)AD_CkSl_Sct=0x0f00;   /* AD Channel A,B,C,D
                                                from Clock1  */
        *(unsigned long *)Clk1_Div=19999;       /* Sampling frequency
                                                20Mhz/20000= 1KHz */
        *(unsigned long *)Clk4_Div=79;
        *(unsigned long *)AD_Mask_CD=0x0200;

        *(unsigned long *)MX_Ctrl=0x1;          /* Enable MIX interrupt */

        *(unsigned long *)DA_FIFO_Rst=0x0;      /* Reset DA FIFO */
        *(unsigned long *)DA_Data_Fmt=0x1;      /* Set DA Data format */
        *(unsigned long *)DA_Data_Fmt=0x1111;

        *(unsigned long *)DA_CkSl_Sct=0x8000;
}

void d2a_enable()
{
        *(unsigned long *)DA_FIFO_Rst=0x0;          /* Reset DA FIFO */
        *(unsigned int *)DA_FIFO_A1=0;
        *(unsigned int *)DA_FIFO_A2=0;
        *(unsigned int *)DA_FIFO_B1=0;
        *(unsigned int *)DA_FIFO_B2=0;
```

```
        *(unsigned int *)DA_FIFO_C1=0;
        *(unsigned int *)DA_FIFO_C2=0;
        *(unsigned long *)DA_FIFO_Rst=0xFF;
}
void d2a_disable()
{
        *(unsigned int *)DA_FIFO_A1=0;
        *(unsigned int *)DA_FIFO_A2=0;
        *(unsigned int *)DA_FIFO_B1=0;
        *(unsigned int *)DA_FIFO_B2=0;
        *(unsigned int *)DA_FIFO_C1=0;
        *(unsigned int *)DA_FIFO_C2=0;
        *(unsigned int *)DA_FIFO_D1=0;
        *(unsigned int *)DA_FIFO_D2=0;
        *(unsigned long *)DA_FIFO_Rst=0x0;      /* Reset DA FIFO */
        *(unsigned long *)DA_Trig_Ctrl=0x07;    /* Stop D/A Channel
                                                   A,B,C Trigger */
        *(unsigned long *)DA_Trig_Ctrl=0x0f;    /* Stop D/A Channel
                                                   A,B,C,D Trigger */
}

 /* file name: interrupt.c */

#include "dsp.h"
unsigned int *int01_vector;
void c_int01();

void disable_int(void)
{
```

```
        *(unsigned long *)0x80000080=0;
        *(unsigned int *)AD_Trig_Ctrl=0x0F;      /* Stop A,B,C,D Channel
                                                    Trigger */
        *(unsigned int *)AD_FIFO_Rst=0x0;        /* Reset AD FIFO */
        asm("   iack @0");                       /* Clear Any Pending
                                                    Interrupts */
}

void enable_int(void)
{
*(unsigned int *)0x10000003 = *(unsigned int *)0x10000003 | 0x00000008;

        int01_vector = (unsigned int *) c_int01;
        asm("   LDEP IVTP,AR0");
        asm("   LDI @_int01_vector,R0");
        asm("   STI R0,*+AR0(3)");
        asm("   IACK @0");
        asm("   LDI IIF,R0");
        asm("   ANDN 000fH,R0");
        asm("   OR 0009H,R0");
        asm("   LDI R0,IIF");
        asm("   OR 2000H,ST");

        /* enable A/D channel */

        *(unsigned int *)AD_FIFO_Rst=0x0;            /* Reset AD FIFO */
        *(unsigned int *)AD_FIFO_Rst=0x7F;           /* AD A1,A2,B1,B2,C1,C2
                                                        FIFO Release and Enable data collection */
```

```
        *(unsigned int *)AD_Trig_Ctrl=0xF0;                /* Trigger Channel
                                                           A,B,C,D */
}

/* file name: int_01.c */

#include "dsp.h"
#include "C:\tic3x4x\c3x4x\cgtools\include\math.h"

void c_int01()
{
        unsigned long D1reading;
        long ADreading;
        tr_low();
        D1reading=*(unsigned long *)AD_FIFO_D1;

        if (index2 < 50000){
                ADreading=*(unsigned long int *)AD_FIFO_A1;
                *(unsigned int *)(POS1+index2) = ADreading;

                ss = *(unsigned int *)(POS1+index2);
                sensor_a2 = (ss & 0xffff0000) >> 16;
                if (sensor_a2 > 32768){
                        sensor_a2 = sensor_a2 - 65536;
                }
                *(unsigned int *)(POSS1+index2) = sensor_a2;
                sensor_a2b1 = *(unsigned int *)(POSS1+index2-1);
                sensor_a2b2 = *(unsigned int *)(POSS1+index2-2);
                sensor_a2b3 = *(unsigned int *)(POSS1+index2-3);
```

```
                sensor_a2b4 = *(unsigned int *)(POSS1+index2-4);

                ADreading=*(unsigned long int *)AD_FIFO_B1;
                *(unsigned int *)(POS2+index2) = ADreading;

                ADreading=*(unsigned long int *)AD_FIFO_C1;
                *(unsigned int *)(POS3+index2) = ADreading;

                ss = *(unsigned int *)(POS3+index2);
                sensor_c1 = (ss & 0x0000ffff);
                if (sensor_c1 > 32768){
                        sensor_c1 = sensor_c1 - 65536;
                }
                *(unsigned int *)(POSS3+index2) = sensor_c1;
                sensor_c1b1 = *(unsigned int *)(POSS3+index2-1);
                sensor_c1b2 = *(unsigned int *)(POSS3+index2-2);
                sensor_c1b3 = *(unsigned int *)(POSS3+index2-3);
                sensor_c1b4 = *(unsigned int *)(POSS3+index2-4);
}

a2_temp = (sensor_a2+sensor_a2b1+sensor_a2b2+sensor_a2b3+sensor_a2b4)/1638.4;
c1_temp = (sensor_c1+sensor_c1b1+sensor_c1b2+sensor_c1b3+sensor_c1b4)/1638.4;

if (index2<12000){
        *(unsigned int *)DA_FIFO_A1=( (unsigned int)(0) << 16 ) & 0xffff0000 ;
        *(unsigned int *)DA_FIFO_A2=( (unsigned int)(0) << 16 ) & 0xffff0000 ;
        *(unsigned int *)DA_FIFO_B1=( (unsigned int)(0) << 16 ) & 0xffff0000 ;
        *(unsigned int *)DA_FIFO_B2=( (unsigned int)(0) << 16 ) & 0xffff0000 ;
        *(unsigned int *)DA_FIFO_C1=( (unsigned int)(0) << 16 ) & 0xffff0000 ;
```

```
        *(unsigned int *)DA_FIFO_C2=( (unsigned int)(0) << 16 ) & 0xffff0000 ;
}

if ((index2 >= 12000) & (index2 < 20000)){
        *(unsigned int *)DA_FIFO_A1=( (unsigned int)(0) << 16 ) & 0xffff0000 ;
        *(unsigned int *)DA_FIFO_A2=( (unsigned int)(index2-12000) << 16 ) &
0xffff0000 ;
        *(unsigned int *)DA_FIFO_B1=( (unsigned int)(index2-12000) << 16 ) &
0xffff0000 ;
        *(unsigned int *)DA_FIFO_B2=( (unsigned int)(0) << 16 ) & 0xffff0000 ;
        *(unsigned int *)DA_FIFO_C1=( (unsigned int)((index2-12000)/2) << 16 ) &
0xffff0000 ;
        *(unsigned int *)DA_FIFO_C2=( (unsigned int)((index2-12000)/2) << 16 ) &
0xffff0000 ;
}

if ((index2 >= 20000) & (index2 < 23000)){
        *(unsigned int *)DA_FIFO_A1=( (unsigned int)(0) << 16 ) & 0xffff0000 ;
        *(unsigned int *)DA_FIFO_A2=( (unsigned int)(8000) << 16 ) & 0xffff0000 ;
        *(unsigned int *)DA_FIFO_B1=( (unsigned int)(8000) << 16 ) & 0xffff0000 ;
        *(unsigned int *)DA_FIFO_B2=( (unsigned int)(0) << 16 ) & 0xffff0000 ;
        *(unsigned int *)DA_FIFO_C1=( (unsigned int)(4000) << 16 ) & 0xffff0000 ;
        *(unsigned int *)DA_FIFO_C2=( (unsigned int)(4000) << 16 ) & 0xffff0000 ;
}

if ((index2 >= 23000)&(index2 < 24500)){
        sin12temp = sin(pi*de12/D);
        cos12temp = cos(pi*de12/D);
        sin34temp = sin(pi*de34/D);
```

```
        cos34temp = cos(pi*de34/D);

        *(unsigned int *)DA_FIFO_A1=( (unsigned int)(-8000* sin12temp) << 16 ) &
0xffff0000 ;
        *(unsigned int *)DA_FIFO_A2=( (unsigned int)(8000* cos12temp) << 16 ) &
0xffff0000 ;
        *(unsigned int *)DA_FIFO_B1=( (unsigned int)(8000* cos34temp) << 16 ) &
0xffff0000 ;
        *(unsigned int *)DA_FIFO_B2=( (unsigned int)(8000* sin34temp) << 16 ) &
0xffff0000 ;
        *(unsigned int *)DA_FIFO_C1=( (unsigned int)(4000) << 16 ) & 0xffff0000
        *(unsigned int *)DA_FIFO_C2=( (unsigned int)(4000) << 16 ) & 0xffff0000
        de12 = de12 + 1;
        de34 = de12;
}

if ((index2 >= 24500)&(index2 < 25500)){
        if (a2_temp<3.9){
                de12 = de12 + 1;
                de34 = de12;
        }
        sin12temp = sin(pi*de12/D);
        cos12temp = cos(pi*de12/D);
        sin34temp = sin(pi*de34/D);
        cos34temp = cos(pi*de34/D);

        *(unsigned int *)DA_FIFO_A1=( (unsigned int)(-8000* sin12temp) << 16 ) &
0xffff0000 ;
```

```
        *(unsigned int *)DA_FIFO_A2=( (unsigned int)(8000* cos12temp) << 16 ) &
0xffff0000 ;
        *(unsigned int *)DA_FIFO_B1=( (unsigned int)(8000* cos34temp) << 16 ) &
0xffff0000 ;
        *(unsigned int *)DA_FIFO_B2=( (unsigned int)(8000* sin34temp) << 16 ) &
0xffff0000 ;
        *(unsigned int *)DA_FIFO_C1=( (unsigned int)(4000) << 16 ) & 0xffff0000
        *(unsigned int *)DA_FIFO_C2=( (unsigned int)(4000) << 16 ) & 0xffff0000 ;
}

if ((index2 >= 27000)&(index2 < 30000)){
        de12 = de12 + 0.8*(3.9597 - a2_temp)-30*(a2_temp-a2_tempb);
        de34 = de12;
        sin12temp = sin(pi*de12/D);
        cos12temp = cos(pi*de12/D);
        sin34temp = sin(pi*de34/D);
        cos34temp = cos(pi*de34/D);
        *(unsigned int *)DA_FIFO_A1=( (unsigned int)(-8000* sin12temp) << 16 ) &
0xffff0000 ;
        *(unsigned int *)DA_FIFO_A2=( (unsigned int)(8000* cos12temp) << 16 ) &
0xffff0000 ;
        *(unsigned int *)DA_FIFO_B1=( (unsigned int)(8000* cos34temp) << 16 ) &
0xffff0000 ;
        *(unsigned int *)DA_FIFO_B2=( (unsigned int)(8000* sin34temp) << 16 ) &
0xffff0000 ;
        *(unsigned int *)DA_FIFO_C1=( (unsigned int)(4000) << 16 ) & 0xffff0000 ;

        *(unsigned int *)DA_FIFO_C2=( (unsigned int)(4000) << 16 ) & 0xffff0000 ;
}
```

```
if ((index2 >= 30000)&(index2 < 33000)){
        de12 = de12 + 0.8*(5.8638 - a2_temp)-30*(a2_temp-a2_tempb);
        de34 = de12;
        sin12temp = sin(pi*de12/D);
        cos12temp = cos(pi*de12/D);
        sin34temp = sin(pi*de34/D);
        cos34temp = cos(pi*de34/D);

        *(unsigned int *)DA_FIFO_A1=( (unsigned int)(-8000* sin12temp) << 16 ) &
0xffff0000 ;
        *(unsigned int *)DA_FIFO_A2=( (unsigned int)(8000* cos12temp) << 16 ) &
0xffff0000 ;
        *(unsigned int *)DA_FIFO_B1=( (unsigned int)(8000* cos34temp) << 16 ) &
0xffff0000 ;
        *(unsigned int *)DA_FIFO_B2=( (unsigned int)(8000* sin34temp) << 16 ) &
0xffff0000 ;
        *(unsigned int *)DA_FIFO_C1=( (unsigned int)(4000) << 16 ) & 0xffff0000 ;
        *(unsigned int *)DA_FIFO_C2=( (unsigned int)(4000) << 16 ) & 0xffff0000;
}

if ((index2 >= 33000)&(index2 < 36000)){
        de12 = de12 + 0.8*(7.6783 - a2_temp)-30*(a2_temp-a2_tempb);
        de34 = de34 + 0.8*(-5.0715 - c1_temp)-30*(c1_temp-c1_tempb);
        sin12temp = sin(pi*de12/D);
        cos12temp = cos(pi*de12/D);
        sin34temp = sin(pi*de34/D);
        cos34temp = cos(pi*de34/D);
```

```
        *(unsigned int *)DA_FIFO_A1=( (unsigned int)(-8000* sin12temp) << 16 ) &
0xffff0000 ;
        *(unsigned int *)DA_FIFO_A2=( (unsigned int)(8000* cos12temp) << 16 ) &
0xffff0000 ;
        *(unsigned int *)DA_FIFO_B1=( (unsigned int)(8000* cos34temp) << 16 ) &
0xffff0000 ;
        *(unsigned int *)DA_FIFO_B2=( (unsigned int)(8000* sin34temp) << 16 ) &
0xffff0000 ;
        *(unsigned int *)DA_FIFO_C1=( (unsigned int)(4000) << 16 ) & 0xffff0000 ;
        *(unsigned int *)DA_FIFO_C2=( (unsigned int)(4000) << 16 ) & 0xffff0000 ;
}
a2_tempb = a2_temp;
c1_tempb = c1_temp;

if (index2 < 51000){
        index2 = index2 + 1;
}
MX_Int_Clr= 0x20000029;
*(unsigned int *)MX_Int_Clr=0x0;
}


/*File name: main.c*/

#include "main.h"

main()
{
        POS1 = 0x800d0000;
        POS2 = 0x800e0000;
```

```
POS3 = 0x800f0000;

POSS1 = 0x800a0000;
POSS2 = 0x800b0000;
POSS3 = 0x800c0000;

index2 = 0;
de12 = 0;
de34 = 0;

pi      =       3.1415962;
L       =       0.0508;
p       =       44.64 * 0.001;          /*1.7573 inch*/
q       =       19.24 * 0.001;          /*0.7573 inch*/
d       =       7.62 * 0.001;           /*0.3 inch*/
th      =       6.12 * 0.001;           /*0.241 inch*/

BAz1    =       0.3445;         /* base on z = 0.003 m*/
BBz1    =       0.3445;

lamda   =       1968.50;        /*turn density along the width*/
beta    =       1711.74;        /*turn density along the height*/

m       =       0.64;           /* kg, total mass of the moving platen*/
inertia_z       =       0.001;  /* kg*m2 */
gama    =       2 * 3.1415962 / 0.0508;
z1 = 0.003;
zs = 27.73 * 0.001;
muiM0 = 0.71;
```

```
delta = 0.0127;
D = 8000;
/*** Register Address ***/
MX_Int_Clr=         0x20000029;
MX_Ctrl=            0x20000028;
Clk1_Div=           0x20000010;
AD_FIFO_Rst=        0x2000001B;
AD_Data_Fmt=        0x20000019;
AD_CkSl_Sct=        0x2000001C;
AD_Trig_Ctrl=       0x20000014;
AD_Mask_CD=         0x20000018;
DA_FIFO_Rst=        0x2000003B;
DA_Data_Fmt=        0x20000039;
DA_CkSl_Sct=        0x2000003C;
DA_Trig_Ctrl=       0x20000034;
AD_FIFO_A1=         0x20000000;
AD_FIFO_A2=         0x20000001;
AD_FIFO_B1=         0x20000002;
AD_FIFO_B2=         0x20000003;
AD_FIFO_C1=         0x20000004;
AD_FIFO_C2=         0x20000005;
AD_FIFO_D1=         0x20000006;
AD_FIFO_D2=         0x20000007;
DA_FIFO_A1=         0x20000020;
DA_FIFO_A2=         0x20000021;
DA_FIFO_B1=         0x20000022;
DA_FIFO_B2=         0x20000023;
DA_FIFO_C1=         0x20000024;
DA_FIFO_C2=         0x20000025;
```

```
	adda_setup();

	*(unsigned int *)DA_FIFO_A1=( (unsigned int)(0) << 16 ) & 0xffff0000 ;
	*(unsigned int *)DA_FIFO_A2=( (unsigned int)(0) << 16 ) & 0xffff0000 ;

	*(unsigned int *)DA_FIFO_B1=( (unsigned int)(0) << 16 ) & 0xffff0000 ;
	*(unsigned int *)DA_FIFO_B2=( (unsigned int)(0) << 16 ) & 0xffff0000 ;

	*(unsigned int *)DA_FIFO_C1=( (unsigned int)(0) << 16 ) & 0xffff0000 ;
	*(unsigned int *)DA_FIFO_C2=( (unsigned int)(0) << 16 ) & 0xffff0000 ;

	sensor_a2 = 0;
	sensor_a2b1 = 0;
	sensor_a2b2 = 0;
	sensor_a2b3 = 0;
	sensor_a2b4 = 0;
	sensor_c1 = 0;
	sensor_c1b1 = 0;
	sensor_c1b2 = 0;
	sensor_c1b3 = 0;
	sensor_c1b4 = 0;

	enable_int();
	d2a_enable();

	processing :
		index = 1;
	goto processing;
}
```

VITA

Name: Vu Huy Nguyen

Address: 107 H, Institute of Energy
Ton That Tung ST, Dong Da
Hanoi, Vietnam

Email Address: vhn1182@gmail.com

Education: B.S., Mechanical Engineering, Hanoi University of Science and Technology, 2005
M.S., Mechanical Engineering, Texas A&M University, 2011